2018-08-01

Permeability Characterization and Fluorescent Void Flow Monitoring for Processing Simulation

John Caleb Lystrup

Permeability Characterization and Fluorescent Void Flow Monitoring for Processing Simulation

John Caleb Lystrup

A dissertation submitted to the faculty of
Brigham Young University
in partial fulfillment of the requirements for the degree of

Doctor of Philosophy

Andrew Robert George, Chair
David T. Fullwood
Julie Crockett
Eric R. Homer
David W. Jensen

Department of Mechanical Engineering

Brigham Young University

ABSTRACT

Permeability Characterization and Fluorescent Void Flow Monitoring for Processing Simulation

John Caleb Lystrup
Department of Mechanical Engineering, BYU
Doctor of Philosophy

Liquid composite molding (LCM) is growing in importance alternative to traditional prepreg-autoclave methods for manufacture aerospace composites. The most significant roadblock to industry's implementation of LCM is the optimization of resin flow to ensure high quality parts. This study developed process optimization tools to foster the adaptation of LCM. The following dissertation characterized the permeability of reinforcement fabrics under various processing conditions, and investigated in-situ bubble flow with carbon fiber. The purpose of this research is to extend the understanding of LCM and push forward the state of the art via sub-studies captured in five chapters, or manuscripts. Research from these manuscripts is as follows.

Chapter 3 sets the groundwork for LCM optimization by extending the current theory for assessing 3D permeability of reinforcement fabrics using an ellipsoidal point infusion experiment. The aim was to improve 3D permeability measurement accuracy for LCM processing models. This work is the first to compare solutions in the context of 75 experiments.

Chapters 4 and 5 extend permeability analysis to curved and sheared geometries, typical to real-world aerostructures. Chapter 4 demonstrates a method for measurement of curvature effects on permeability with vacuum infusion. A correlation was shown between curvature (as evaluated over four radii) and effective permeability. Chapter 5 researches the shearing of reinforcement fabric (e.g. when reinforcements are draped over double curvature). The study shows that permeability actually increases for mid-range shear angles beyond the shear-locking angle, and develops a technique for obtaining the 3D permeability of sheared fabric.

Chapter 6 investigates carbon fiber voids *in situ.* LCM optimization requires improved void monitoring for carbon fiber. It is challenging to monitor void flow *in situ* with carbon fiber reinforcements because of fiber opacity. The research builds upon a new automated fluorescent imaging method to monitor void flow in-situ. Results include high-resolution and high-contrast images and 230 data points for infusion velocity vs. void content data.

Chapter 7 contributes to the growing interest in LCM processes for aerospace applications by providing a short cost summary of typical processes for manufacturing aerospace composite parts. Data shows that LCM is a financially wise alternative to automated fiber placement (prepreg-autoclave) manufacturing when a void content of 2-2.5% is acceptable. Work on LCM processes optimization indicates that these percentages will reduce in coming years.

Keywords: permeability, liquid composite molding, void mobility, void content, carbon fiber

ACKNOWLEDGEMENTS

I cannot express enough gratitude to Zodiac Aerospace for funding and motivating this research, as well as providing valuable feedback related to pressing issues in the aerospace composites industry. I would like to thank Dr. Razmik Boodaghians for his persistent and professional feedback.

Dr. Andy George deserves the highest gratitude of all for being patient, insightful, and instilling trust and confidence. He is both an outstanding example and mentor. His leadership is evident through a personal commitment to excellence, his example of lifelong holistic learning, and his service to family and friends. Anyone who has participated in his lectures knows that Andy is full of energy for life and knowledge. Truly our research meetings have been paramount learning experiences for me.

Special thanks belongs to Dr. David Fullwood for introducing me to composite materials, and for always encouraging me to reach higher personal standards. Special thanks to Dr. David Jensen for his courses, as well as making time to answer academic, life, and professional questions. Special thanks as well to Dr. Julie Crockett and Dr. Eric Homer for their technical guidance. Special thanks to Cole Childs, Jordan Ahlstrom, Suyash Ghirnikar, Perry Burton, Mike Laird, and Kevin Cole for their laboratory assistance and friendship.

Special thanks belongs to Brock Zobell for his graduate work in spearheading the fluorescent image analysis method. Special thanks to Kim Stevens for writing the original code to analyze void content from thousands of carbon fiber void images. Brock's and Kim's work on image analysis was critical to this research.

Finally, thanks to my family and friends for their unceasing support and encouragement.

TABLE OF CONTENTS

LIST OF TABLES

LIST OF FIGURES

1 INTRODUCTION

The carbon fiber industry continues to grow at a rate of 9-11% annually; and continued growth relies heavily on improved processing [1]. The application of prepreg and autoclave cure the traditional standard to the aerospace industry. A widely considered alternative in aerospace composites manufacturing to prepreg use is liquid composite molding (LCM), which encompasses several process variants all involving pushing or pulling the resin matrix through the reinforcement before cure. The advantages of LCM over prepreg include lower material costs, less material scrap, less freezer storage requirements (saving energy costs), and greater flexibility in complex geometries and preforming (minimization of post-processing). LCM is seen as a promising alternative to prepreg-autoclave because it is capable of keeping up with growing demand. The general disadvantages of LCM compared to prepreg are associated with the added field of process engineering involving liquid flow, and the higher void content due to mechanical entrapment of voids during infusion. When molding under a vacuum bag (typical for large parts), a thickness gradient is caused by the pressure gradient from the resin inlet to the vent. In order to capitalize on the benefits of LCM, the weaknesses must be mitigated.

The effects of all of these weaknesses can be minimized with an optimized LCM process. Such optimization requires an understanding of the underlying mechanics of such a process, from experimentation on the effects of variation in manufacturing parameters. Prototype manufacturing serves this purpose, but at a great cost in time and money. The development of an

optimized LCM process can be greatly accelerated by the use of computer process simulation tools. As the entire composites industry seems to be moving towards LCM processes (for lower cycle time in the case of high performance composites, and for less volatile emissions in the case of low-cost engineering materials), such process optimization tools have received a great deal of attention in the last few years. Process modeling has been established for draping, filling, resin cure, void formation and mobility, and residual stresses. Such process simulation requires characterization of various material parameters for both the resin and reinforcement, but then a variety of processing environments and tooling configurations can all be virtually evaluated. Thus characterization of resin and reinforcement are significant steps toward optimizing LCM and benefitting the composites industry.

1.1 Research Aim

The goal of this research is to build a characterization portfolio for an LCM resin-matrix system which will not only aid its simulation, but push the state of art forward. Permeability measurements for the fabric in flat, curved, and sheared geometries are evaluated, and new permeability measurement methods are proposed. A new test is developed to test lateral flow around a vertically-oriented curve, and calculation methods are compared. Permeability is characterizing for a stiff fabric sheared beyond the shear-lock angle. Recent fluorescent void flow monitoring research is built upon to implement an automated method of data analysis. A method for obtaining very clear images of in-situ flow through carbon fiber is established. A financial summary of aerospace composites processes is extended to model cost behavior as a function of part count to help illustrate the current state of LCM in comparison to other methods. And finally, a summary of findings, contributions, and recommendations is presented – all to assist with optimization of LCM simulation.

1.2 Coming Publications

The dissertation begins a background chapter, then gets into five chapters composing the content of 4 forthcoming research publications. Chapter 3 evaluates methods for obtaining the 3D permeability of reinforcements. Chapters 4 and 5 characterize the permeability of a stiff unidirectional weave fabric when fabric is applied to advanced geometries. These two chapters are designed to assist with LCM permeability characterization for parts with double curvature, or when both shear and curvature are experienced in fabric draping. The chapters are condensed into a single publication because of their mutual relevance to such geometries. Chapter 6 is a highly novel approach to obtaining *in situ* data on carbon fiber void formation. Chapter 7 is a brief evaluation of part cost in terms of void content and manufacturing process.

2 BACKGROUND

Composite materials offer many advantages over traditional materials. Carbon fiber, for example, is a superior material to Aluminum in many applications, especially in industries which seek to optimize strength- and stiffness-weight ratios. Highly recognized work by Ashby on materials selection charts shows that composites – especially carbon composites – are advantageous in applications such as aerospace parts, where high strength- or stiffness-to-weight ratios are necessary [2].

High-performance composites are primarily made by autoclave-prepreg processing. Autoclave-prepreg processing enable manufacturers to produce composite parts with high percent fiber, or fiber volume fraction (v_F), as well as low void or bubble content (v_B). Pressures from the autoclave compress the composite part during and after cure to reduce trapped bubble size and increase the v_F by squeezing out excess resin. This process allows manufacturers to produce parts with excellent mechanical properties. But these advantages come with a cost. Among other drawbacks, autoclave-prepreg processes are very expensive [3]. Industry and academia are mutually seeking to move away from these processes.

Less expensive materials and processes are abundant. As was already discussed, many alternative materials like aluminum are available. But these materials often make inferior parts. A large family of alternatives processes can be found in the liquid composite molding (LCM)

sector. LCM processes include resin transfer molding, vacuum-assisted resin transfer molding, flexible injection, and a multitude of other processes which involve resin penetration of reinforcements. These are different from autoclave-prepreg processes because their reinforcement fabrics are not previously impregnated with resin.

LCM offers several strategic advantages compared to autoclave-prepreg methods. LCM processes can produce parts typically for a fraction of the cost/lb. LCM processes enable larger and more complicated parts to be made in one go, reducing part count and simplifying manufacturing. LCM parts are not limited by the size of an autoclave.

But autoclaved-prepreg processed parts are still favored over those made by infusion due to a tendency of LCM-made parts to exhibit a thickness gradient and have higher void content. It is also challenging to make sufficiently thick parts with LCM, due to the need of resin to fully saturate the fabric. The push of industry and academia is thus to optimize LCM processes such that desired part thickness and void content are achievable, and make autoclaves obsolete.

Research from industry and academia are aimed at understanding and developing process simulation tools. These can assist in developing optimized infusion processes; less time, less cost, and fewer prototype count come from predictive simulation. Better parts are also possible; lower void content, controlled concentration of voids to strategic part areas, maximized thickness, and part homogeneity are possible. By understanding and developing characterization tools, researchers are enabling LCM parts to approach, and even exceed the mechanical properties resulting in autoclave-prepreg parts. Furthermore, simulation enables larger part sizes and more advanced geometries for performance.

These flow simulation tools require the characterization of the different fluid and reaction phenomena involved during infusion. Each of these phenomena, sufficiently incorporated, improve simulation results and allow the optimization of LCM composite parts. These phenomena are addressed as follows: Darcy's Law, permeability, resin viscosity, rheometry and cure kinetics, compressibility, and void formation and mobility.

After the background of this dissertation is addressed, the document is organized into research papers, with each paper composing a chapter. The first three papers address the topic of permeability for composite processing simulation by considering (1) models for measuring the full permeability tensor, (2) characterizing the effects of curvature on local fabric permeability, (3) characterizing the effects of in-plane shear on local fabric permeability. The final two papers are concerned with void content. These papers are organized into (4) an assessment of void formation and mobility *in-situ* in carbon fiber using fluorescent dye – one of the first studies of its kind, and (5) a consideration of the cost of void content by comparing different composites manufacturing processes. Altogether, these five papers provide a valuable knowledge bank for any LCM process optimization toolbox.

2.1 Fiber and Resin Material Selection

In collaboration with aerospace industry partners, a resin and fabric combination were chosen. These materials were vetted against numerous other candidates, and were selected because of their desirability for high-performance. The LCM resin chosen was RTM-6, and the fabric chosen was Vectorply C-L 0900. RTM-6 functions well in LCM processes (with a low, watery viscosity at high temperature, and good mechanical properties after cure). The fabric was designed for high-performance applications such as light-weight pressure tanks with high tensile

loads. Though its drapability was minimal. This provided some motivation to understand how permeability was affected when the fabric was draped over double-curvature (i.e. experienced in-plane shear).

2.2 Darcy's Law

Darcy's Law serves as a foundational model of fluid flow through a porous medium [4]. Models for flow simulation of advanced composites manufacture utilize Darcy's Law in conjunction constitutive laws and empirical data relationships to predict the velocity of the resin flow front. This law is given by:

$$\vec{V} = -\left(\frac{K}{\mu}\right)(\nabla p - \rho\vec{g}) \tag{2-1}$$

$\vec{V}$ is the volume fraction averaged Darcy velocity, K is a material permeability tensor, μ is the dynamic fluid viscosity, ∇p is the pressure gradient across the porous medium, ρ is the resin density, and $\vec{g}$ is the gravitational acceleration. Originally, this law was used to predict water flows through sand, however, it now serves as a fundamental relationship for the flow of resin through a fiber reinforcement.

For isotropic permeable substrates, such as a bed of sand, permeability (K) is a zeroth order tensor (i.e. a scalar quantity). However, when materials begin to demonstrate any degree of anisotropy, permeability quickly complicates. Composite materials are often anisotropic and have a second-order permeability tensor, shown as follows [5]:

$$\begin{bmatrix} u \\ v \\ w \end{bmatrix} = -\frac{1}{\mu}\begin{bmatrix} K_{xx} & K_{xy} & K_{xz} \\ K_{yx} & K_{yy} & K_{yz} \\ K_{zx} & K_{zy} & K_{zz} \end{bmatrix}\begin{bmatrix} \frac{\partial p}{\partial x} - \rho g_x \\ \frac{\partial p}{\partial y} - \rho g_y \\ \frac{\partial p}{\partial z} - \rho g_z \end{bmatrix} \tag{2-2}$$

For application to reinforcement fabrics, a few modifications and simplifications to Darcy's Law are made. In order to keep a constant permeability tensor for a fabric as the fabric is compressed, a porosity term, φ, is introduced. The definition of porosity is $\varphi = 1 - v_f$ where v_f is the fiber volume fraction. Higher porosity leads to lower flow velocity:

$$\begin{bmatrix} u \\ v \\ w \end{bmatrix} = -\frac{1}{\mu\varphi}\begin{bmatrix} K_{xx} & K_{xy} & K_{xz} \\ K_{yx} & K_{yy} & K_{yz} \\ K_{zx} & K_{zy} & K_{zz} \end{bmatrix}\begin{bmatrix} \frac{\partial p}{\partial x} - \rho g_x \\ \frac{\partial p}{\partial y} - \rho g_y \\ \frac{\partial p}{\partial z} - \rho g_z \end{bmatrix} \tag{2-3}$$

A layer of carbon fiber reinforcement fabric is orthotropic, with axes of symmetry in the three principal directions. Thus Darcy's equation is simplified further to treat the permeability tensor as orthogonal. With three unique and independent terms, K is replaced with its diagonalized equivalent:

$$K = \begin{bmatrix} K_{xx} & K_{xy} & K_{xz} \\ K_{yx} & K_{yy} & K_{yz} \\ K_{zx} & K_{zy} & K_{zz} \end{bmatrix} = \begin{bmatrix} K_{xx} & 0 & 0 \\ 0 & K_{yy} & 0 \\ 0 & 0 & K_{zz} \end{bmatrix} \tag{2-4}$$

In literature, the effects of gravity are often miniscule and ignored so long as the sample is tested above the resin pot. Putting it all together, Darcy's Law simplifies to work as the foundational expression for resin flow in composites:

$$\begin{bmatrix} u \\ v \\ w \end{bmatrix} = -\frac{1}{\mu\varphi}\begin{bmatrix} K_{xz} & 0 & 0 \\ 0 & K_{yy} & 0 \\ 0 & 0 & K_{zz} \end{bmatrix}\begin{bmatrix} \partial p/\partial x \\ \partial p/\partial y \\ \partial p/\partial z \end{bmatrix} = -\frac{1}{\mu\varphi}\begin{bmatrix} K_{xx}\frac{\partial p}{\partial x} \\ K_{yy}\frac{\partial p}{\partial y} \\ K_{zz}\frac{\partial p}{\partial z} \end{bmatrix} \tag{2-5}$$

2.3 1-D Characterization

A common application of the Darcy equation is the measurement of 1-D flow through a composite reinforcement fiber bed. This is done restricting flow in two of the three principle directions. For example, looking at the *x* direction alone:

$$u = \frac{\partial x}{\partial t} = -K_{xx} \frac{1}{\mu \varphi} \cdot \frac{\partial p}{\partial x} \tag{2-6}$$

Solving for K_x and integrating over an assumed linear pressure gradient, the equation for permeability in terms of local resin velocity is determined:

$$K_{xx} = \frac{u \mu \varphi}{\Delta p} x \tag{2-7}$$

This formula is built upon in Chapter 3 in order to characterize permeability of locally-curved regions.

To obtain the tensor values with 1-D testing, fabric must be oriented such that the flow direction matches the desired subscript. For example, if one wanted to obtain K_{zz} (through-thickness permeability), one could stack fabric vertically and control flow such that the flow was uniform in the x and y directions, allowing those terms to drop out of Equation 2-5. Returning to the example in the x direction, integration of each of the derivative terms results in the formula for 1-D permeability in terms of flow distance (and not velocity):

$$K_{xx} = \frac{x^2 \mu \varphi}{2 \Delta P t} \tag{2-8}$$

Here, x is the distance the flow front has traveled, and ΔP is the magnitude of the pressure drop over the sample length. This method is typical for computing simple 1-D permeability. To provide further background, an example of an experiment for the 1-D permeability characterization of a fiber glass sample is shown in Figure 2-1.

Figure 2-1: Top view of a 1D flow test for fiber glass. Flow is shown from left to right

In the image, a rectangular fiber bed is held at a constant thickness. Some fluid (typically oil with similar viscosity and chemistry to LCM resins) is injected on the left. The fluid flows through the sample to the right. Fiber saturation is marked by the dark region on the left. The lighter region is unsaturated fabric. The boundary between saturated and unsaturated fabric is referred to as the "flow front." From this type of test, one can obtain the 1-D permeability of the fabric.

For the doctoral research at hand, testing began with 1-D permeability testing. These tests were used to familiarize the doctoral candidate with fundamental methods of composites processing research, as well as assist with the research of others. After the candidate was familiar

with 1-D permeability testing, an introduction to 2D (in-plane elliptical) and 3D (ellipsoidal) permeability was made.

2.4 2D and 3D Permeability

In-plane elliptical flow, or 2D flow, is another useful type of study for measuring the permeability of fabrics. One can obtain both K_{xx} and K_{yy} simultaneously. The value of 2D flow tests is that one can better understand the interactions of flow between warp and weft fibers. Examples of this kind of research is given by [6]. These results are valuable for simulation when K_{zz} is not of special interest.

While through-thickness permeability is sometimes not of interest, it is important when optimizing composites processes. That is because many composite parts involve a non-uniform flow-front through the thickness of the reinforcement. In other words, one may see a fully saturated on the outside of a composite while underneath the reinforcement is unsaturated. If possible, therefore, it is useful to obtain K_{zz}.

Ideally, the full permeability tensor can be obtained in one test, providing the essential permeability data for basic simulation to occur. In fact, several methods have been developed which obtain the entire ellipsoidal flow tensor values (K_{xx}, K_{yy}, and K_{zz}) simultaneously. These methods are of primary interest in Chapter 3. The first work by the doctoral candidate was to assist with measurements for comparing advanced 3D permeability methods. Further information on this topic can be found in Chapter 3.

2.5 *K* Notation

Now that the background on the permeability tensor has been discussed, its orthogonal components, K_{xx}, K_{yy}, and K_{zz}, will be referred to throughout this dissertation as K_x, K_y, and K_z, respectively. Other K notation will be defined in individual chapters.

2.6 Permeability Standardization

Permeability is one of the most challenging yet important parts of composites processing simulation, because it plays a critical role in defining the flow behavior of resin through a bed of fibers. Permeability profiles can be unique to each and every simulation, with permeability values changing from on unit cell to the next. Furthermore, researchers have had trouble generating consistent results from permeability measurements. Two international benchmark studies made substantial efforts at standardizing permeability methods for 1-D testing [7,8]. Yet even when characterizing the same materials and using the same methods, data spread of 25% was observed [8]. Despite this large permeability data spread, it is still critical for LCM simulation to incorporate researcher's best efforts to characterize fabric permeability. Work has even begun on 3D testing standardization. Chapters 4 and 5 present methods for measuring the permeability of locally curved and sheared (deformed) fabrics.

2.7 Resin Viscosity

Permeability is one of the major topics of this dissertation. However, one cannot fully model the simulation of LCM infusion with a knowledge of fabric permeability alone. Resin cure and viscosity behavior must also be understood. This next section provides background on LCM resin infusion, and shows how RTM-6 properties were verified by comparing data to previous research.

Resin viscosity is related to permeability, resin velocity, and pressure. Higher viscosity resins tend to flow slowly and miss saturating tows of fabric. It is critical from a part quality perspective to understand the viscosity of a resin both during infusion and for simulation infusion. The resin viscosity inputs for LCM simulation during infusion greatly depend on factors such as temperature, speed of infusion, and part thickness. A resin can be a brittle solid at room temperature and a runny liquid at infusion temperature.

There is a balance that must be maintained. The simulator and manufacturer desire to infuse resin at a high temperature for sufficiently long so that the part saturates; but saturation must take place before the resin begins to gel. Gel time is the time required for a polymer chain length to grow to match that of its channel. Once a resin gels, it thickens to a stop, and the part continues to cure with stagnant resin. Air bubbles and unsaturated regions then remain in place.

However, if the operator increases process temperature too high, or if part thickness facilitates internal temperature spikes, a potentially hazardous exotherm (out-of-control exothermic reaction, sometimes leading to explosion) can occur. An exotherm will ruin part production and potentially endanger manufacturers. One instance an exothermic resin reaction was seen firsthand in the research lab while tuning simulation parameters because a tired researcher mistakenly turned the oven too high. Toxic vapors were released and the building was evacuated. Thus many factors need to be considered when considering resin viscosity. For simulation a clear understanding of the resin cure is essential.

As resin cures, viscosity increases according to reaction kinetics. Each resin has a unique cure profile. For the research at hand, RTM-6 was used because of its desirable properties for Aerospace LCM [9]; the resin drops in viscosity for a sufficient time to infuse into a reinforcement, matches carbon fiber sizing well, and has the desirable mechanical properties.

RTM-6 has stayed the same over many years in order to maintain its certifications among the largest aerospace companies, such as Airbus and Boeing. Nevertheless, these companies conduct tests periodically to validate the constancy of RTM-6. Previous research was conducted by Dr. Andy George on developing a cure model for RTM-6 as Swerea SICOMP. If the properties of RTM-6 have held constant, then his previously developed cure model can also be applied to the research at hand for LCM simulation. Rheological and differential scanning calorimetry (DSC) were used to validate the resin sample as consistent with known behavior. A cure model from literature is derived, and DSC and rheometry validation of RTM-6 are presented.

Much of the work for DSC and rheometry had already been completed at the Swedish Institute of Composites (SICOMP) [10]. This next section of background describes the resin chemistry, as well as how the resin properties were verified against existing knowledge.

2.8 Cure Model

RTM-6 and other curing polymers experience an effective maximum cure limit which incorporates diffusion effects. Maximum cure, X_{max} is a function of curing temperature. Thus a sample which cures entirely at 200°C could cure to a higher extent than one curing at 180°C. Cure extent is a desirable feature in LCM because a higher cure extent leads to better mechanical properties. The relationship between temperature and maximum cure extent was modeled in the literature as a quadratic function with three constants B_0, B_1, and B_2 [11]:

$$X_{max}(T) = B_0 + B_1 T + B_2 T^2 \tag{2-9}$$

For RTM-6, the following parameters were shown in :

Table **2-1** obtained [10]:

Table 2-1: Resin cure extent parameters

Parameter	RTM-6
B_0 (-)	-1.556
B_1 (1/K)	$9.276 \cdot 10^{-3}$
B_2 (1/K²)	$-8.300 \cdot 10^{-6}$

There are numerous models for curing epoxy, typically based on the Kamal function:

$$\frac{dx}{dt} = (k_1 + k_2 \cdot x^m) \cdot (1 - x)^n \tag{2-10}$$

The Kamal function describes that the rate of cure with respect to cure extent, $x(t)$, where $m, n \in \mathbb{R}_+$ and $m \leq n \; \forall \; \mathbb{R}$ [12]. Several versions of this equation have been proposed in the literature; many such versions were fitted to data for RTM-6 and the following equations (which have been previously used to describe specifically RTM-6) resulted in the best fits. In the Kamal equation, 1 is assumed to represent the maximum cure extent. However, for greater accuracy 1 can be replaced with X_{max}, giving us

$$\frac{dx}{dt} = (k_1 + k_2 \cdot x^m) \cdot (X_{max}(T) - x)^n \tag{2-11}$$

Furthermore, by making the rate-order dependent on temperature, n can be replaced with $n_A + n_B T$. Thus,

$$\frac{dx}{dt} = (k_1 + k_2 \cdot x^m) \cdot (X_{max}(T) - x)^{n_A + n_B T} \tag{2-12}$$

Finally, k_1 and k_2 are both Arrhenius equations (or terms), where

$$k_i = A_i e^{-E_i/RT} \tag{2-13}$$

In these equations, E_i represent activation energies, A_i are constants, and R is the universal gas constant [13]. This brings the cure rate equation to be

$$\frac{dx}{dt} = (k_1 + k_2 \cdot x^m) \cdot (X_{max}(T) - x)^{n_A + n_B T} \tag{2-14}$$

For both scientific and practical application reasons, resin viscosity is typically a function of cure extent and temperature. A model used with RTM-6 in the past with good fit results is the Macosko percolation model [13]:

$$\mu(t) = f(x, T) \tag{2-15}$$

$$\mu(x, T) = A_{\mu 0} e^{\left(E_{\mu 0}/R(T+273)\right)} \cdot \left(\frac{x_{gel}}{x_{gel} - x}\right)^{[(A_1 + A_1 T) + (B_1 + B_2 T)x]} \tag{2-16}$$

x_{gel} is an actual physical parameter fitted to the data (requiring six constants: m, n, A_1, E_1, A_2 and E_2), representing the cure extent at the point of gelation, when processing becomes too difficult. The cure extent is defined as the percent of epoxy ends which are opened by diamine hardeners, which constitutes the curing reaction. A higher cure extent corresponds with higher glass transition temperature (T_g) and improved mechanical properties. Aerospace resins usually involve tetra-functional epoxies, e.g. the epoxy molecule in Hexcel RTM-6:

The model developed at SICOMP for RTM-6 cure is given by Equation 2-17, and may be used to predict the reaction rate, *dx/dt* at any combination of temperature, *T*, and cure extent, *x*.

$$x_{\max} = -1.556 + 9.276 \cdot 10^{-2} \cdot T + -8.300 \cdot 10^{-6} \cdot T^2 \tag{2-17}$$

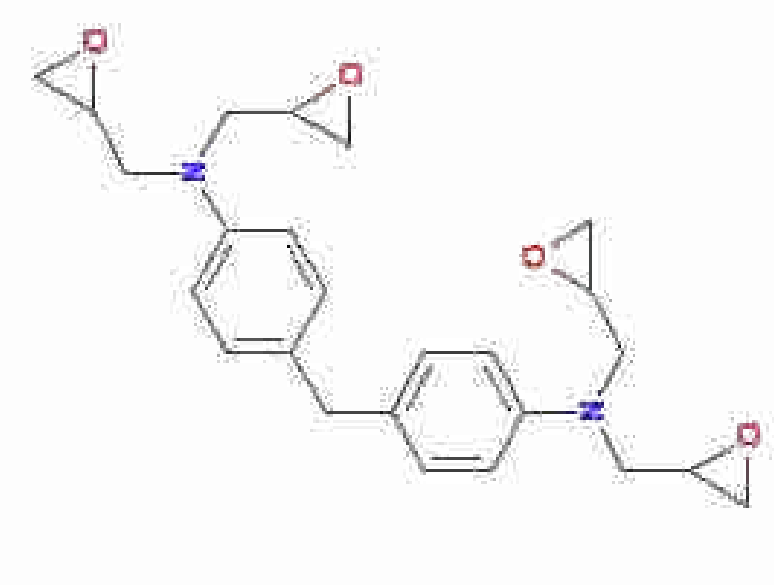

Figure 2-2: RTM-6 molecule

With the combination of a cure model, and a viscosity model based on that cure model, the effects of any temperature history on the processing viscosity can be predicted and optimized. An example is shown below (Figure 2-3) for a room-temperature curing epoxy, where a temperature shift from 25°C to 40°C occurs mid-cure, and the resulting viscosity, both its initial drop and steeper climb afterwards are shown. The graph on the left shows how viscosity changes under a simple temperature shift. On the right is a graph showing cure rate increases after temperature increases during an infusion/cure cycle.

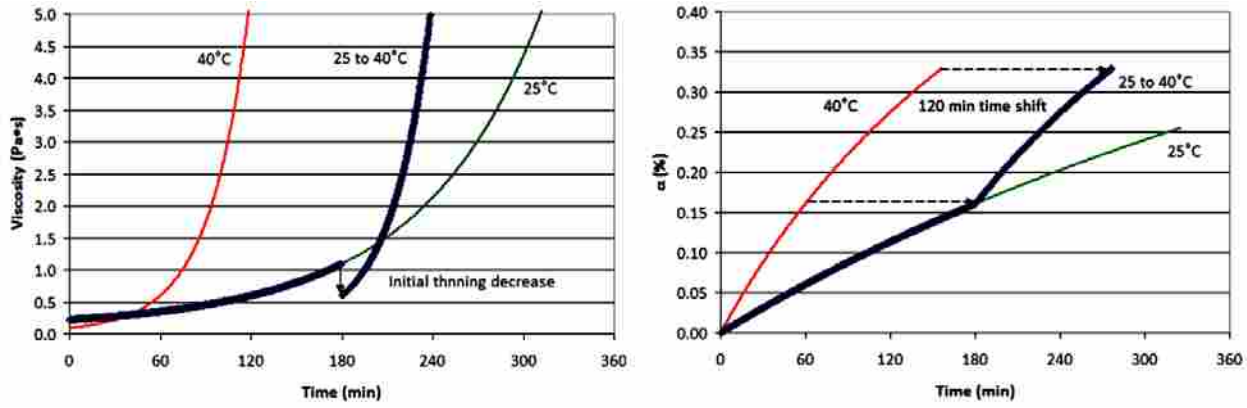

Figure 2-3: Predicted viscosity for switch from 25° to 40°C, compared to isothermal [14]

2.9 Differential Scanning Calorimetry

Differential Scanning Calorimetry (DSC) is a widely used technique to help identify polymeric materials, such as a composite resin. This is largely done by identifying the glass transition temperature for the material. This transition time appears as a spike in cure rate, or a step in cure extent; as amorphous glass rises in temperature, and begins to melt, cure rate rapidly increases because of increased resin mobility. For the verification of RTM-6, a dynamic measurement was taken, where temperature of samples was gradually increased over the desired range and sample heat capacity was monitored.

Dr. Andy George's work at SICOMP (Swedish Institute of Composites) involved the development of three models for RTM-6. The research at hand generated new RTM-6 DSC data and compared results to the models for verification. Results showed behavior consistent enough to conclude that the RTM-6 resin used was similar enough to resin previously studied, however re-testing was necessary to validate the resin behavior in one case because of an initial DSC error. Figure 2-4 shows a comparison of results of the new experimentation to existing models.

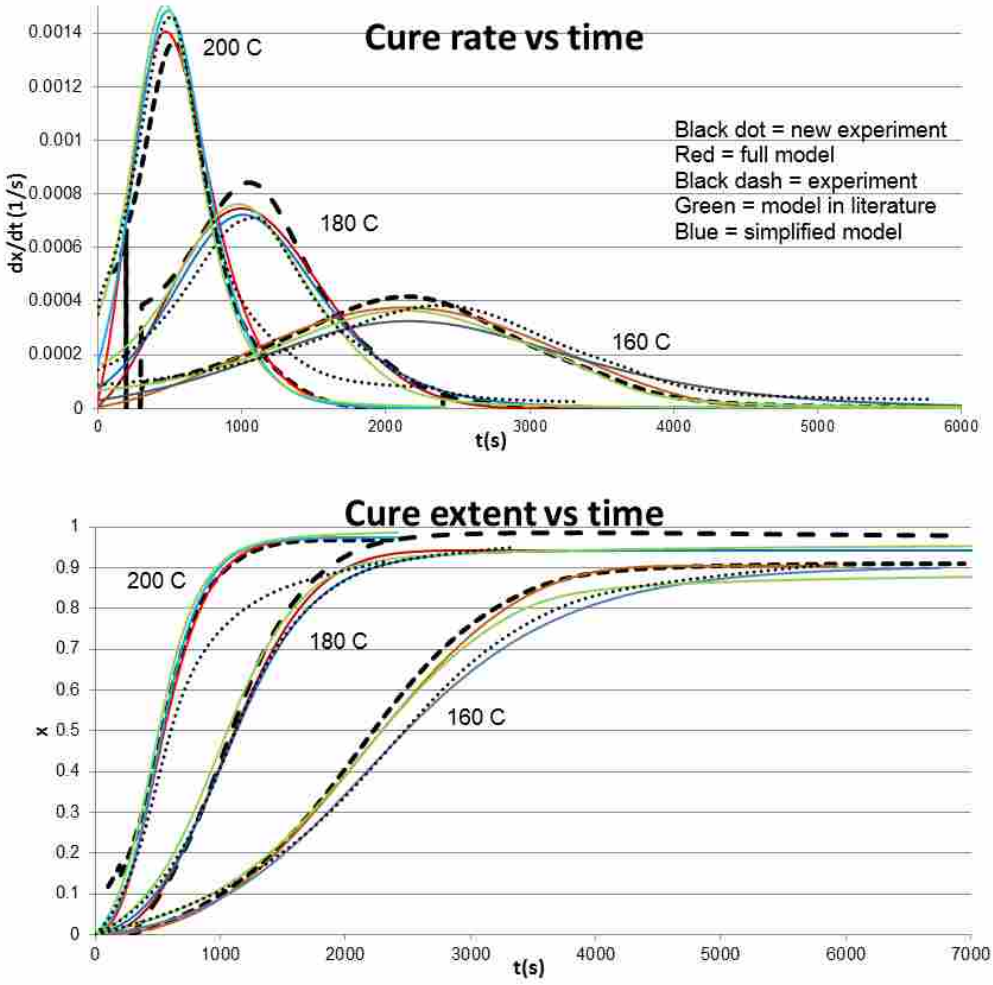

Figure 2-4: Cure rate and cure extent vs time

Although new experiment curves for cure extent and cure rate curves closely match for 180 and 160°C, there is a large visible deviation between the experiment and the models for 200°C. This information suggests that a substantial exothermic reaction was still taking place at the end of the 200°C test. Note how the cure rate does not level off to zero, and that the cure extent continues to ramp upward linearly at the end of the experiment.

The deviation was attributed to an un-evenly full resin cup for the 200° sample. The method of applying the resin to the DSC sample cup may have affected the cure rate of the sample. When the experiment was conducted, the 160 and 180°C samples were examined first. The method of placing resin in the sample cups was simple. Resin was heated slightly until flowing using a handheld heat blower. A pipet was used to pull out a drop of resin. The resin was placed in the DSC cup. In both cases (160 and 180°C), the resin mass was similar. Furthermore, the shape of the resin in the DSC cup was similar. The error and correction are shown in Figure 2-5.

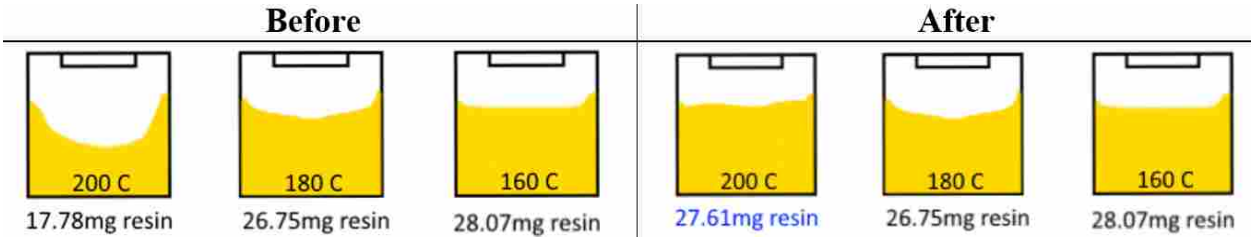

Figure 2-5: DSC cup cross sections and masses for RTM-6 verification

The error was corrected and results improved significantly. The 200°C sample was initially of a significantly smaller mass, almost half of the other samples. When the resin was placed in the DSC cup, the sample clung to the walls of the cup. It is possible that as the sample cup was heated (from the bottom), the lower portion of the resin cured before the upper portion of resin. Results after the correction are shown in Figure 2-6 and provide clear evidence that the models previously generated for RTM-6 in simulation were valid. This result is conclusive of the usefulness of properly applying resin to a test vessel when using DSC to measure cure thermal response.

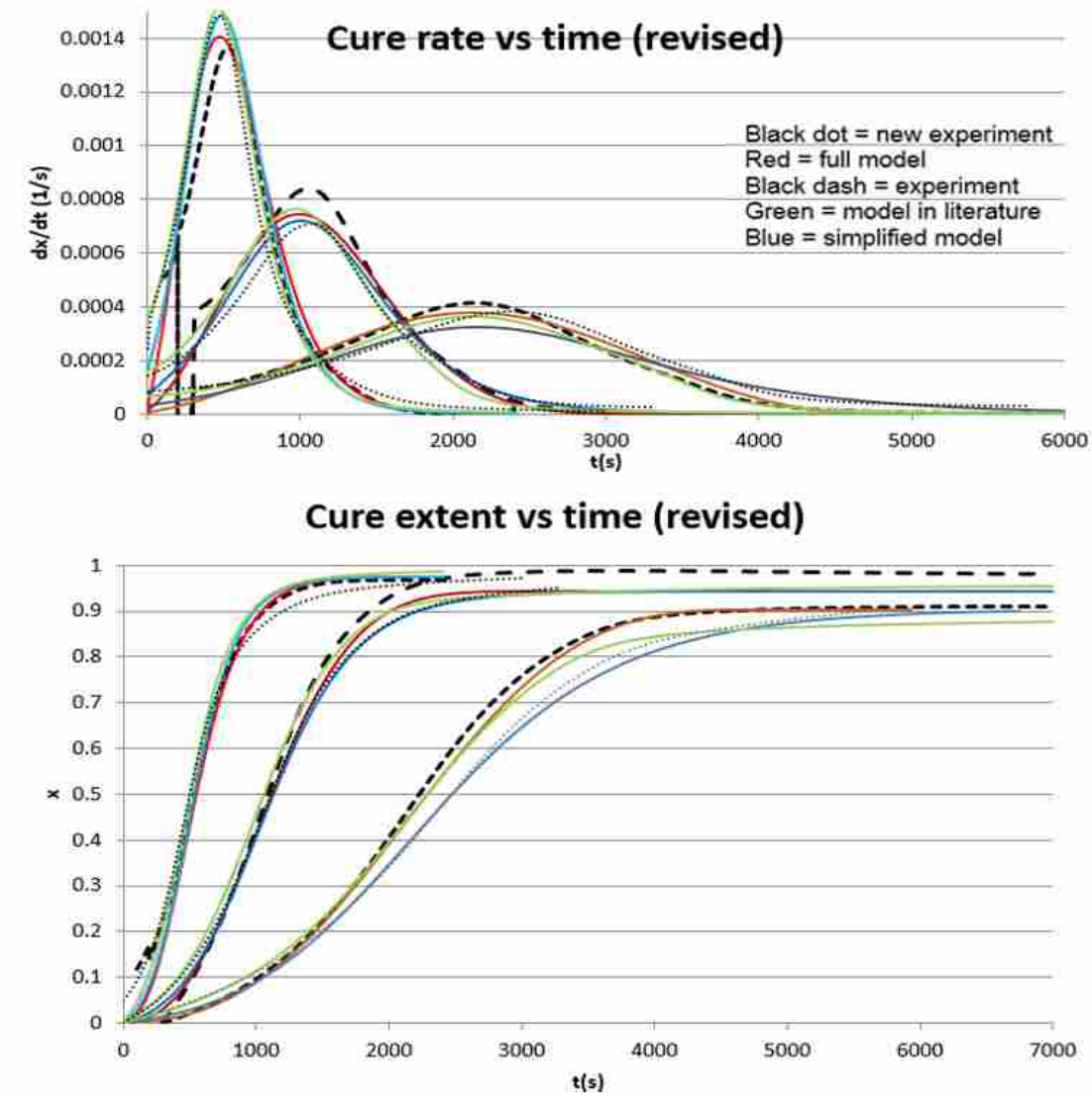

Figure 2-6: Revised cure curves

2.10 Rheometry

Rheometry is the method of measuring the viscosity or "stickiness" of a fluid, typically with a viscometer. Viscosity is often measured in Pa · s. To measure the viscosity of RTM-6 in

preparation for LCM simulation, constant temperature tests were conducted while the viscometer bob was rotated. Researchers at SICOMP previously modeled RTM-6 viscosity, as shown in Equation 7-10. Viscosity, μ was described as a function of cure extent and temperature according to the following model:

$$\mu(x,T) = A_{\mu 0} e^{\left(E_{\mu 0}/R(T+273)\right)} \cdot \left(\frac{x_{gel}}{x_{gel}-x}\right)^{[(A_1+A_1T)+(B_1+B_2T)x]} \quad (2\text{-}18)$$

Table 2-2: μ fit constants

A1 (1/s)	E1 (J/mol)	A2 (1/s)	E2 (J/mol)	m	nA	nB (1/°C)
26387	80952	14672	59214	0.637	-0.503	0.00734

This model is assumed to still apply to RTM-6 because cure results from DSC are nearly identical to existing models. From the plots, it is clear that as cure temperature increases, initial viscosity lowers and cure rate increases. These cure plots are shown in Figure 2-7.

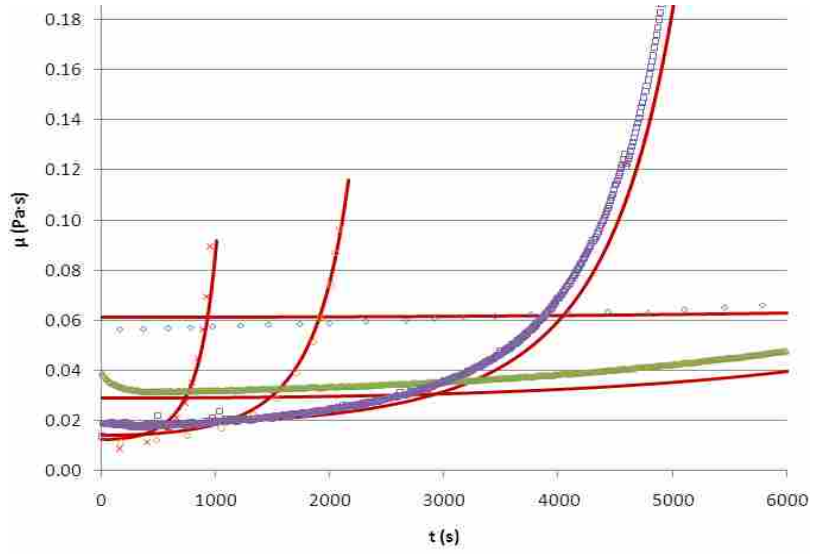

Figure 2-7: Viscosity of RTM-6 when held at constant temperature

2.11 Compressibility

After resin viscosity and permeability have been characterized, the remaining key feature of the Darcy equation to be addressed is compressibility, or a study of porosity (φ) and volume fraction (v_F). Compressibility studies of composite materials express how the fiber layup expands and compacts under pressure. Significant efforts to model the compressibility behavior of composite materials [14-18]. For one-sided LCM processes such as VARTM, compressibility testing can provide insights to assist with predicting fiber volume fraction, v_F, and flow behavior. Recent research has shown that resin pressure and compaction pressure are not synonymous, though they are related [19].

For compressibility experimentation to develop models, an Instron is often used to measure, for example, the pressure response as a displacement profile is applied to a reinforcement layup. Dry and saturated tests are common, and help researchers to isolate fabric and resin behavior for modeling. Figure 2-8 shows a system used by researchers to assess the permeability of the UD weave fabric used for the research at hand.

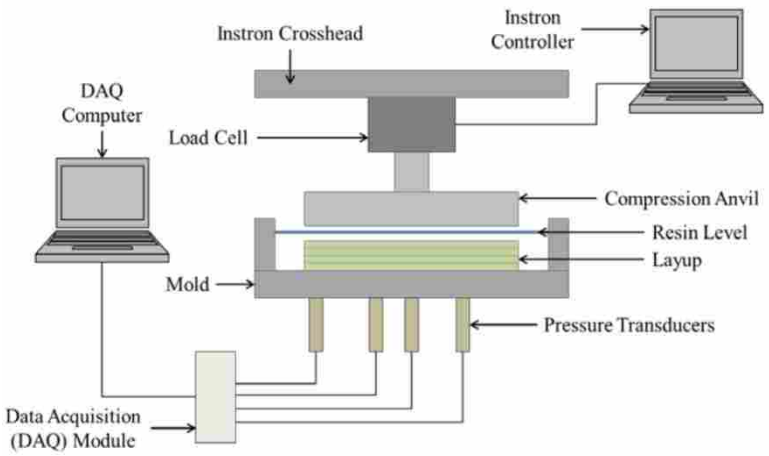

Figure 2-8: Instron machine setup for compressibility testing [19]

For typical VARTM infusions, the non-uniform bag height [15] and pressure distribution is similar to that of a 1-D test [19,20]. This type of experiment can help to measure the thickness gradient of a part under atmospheric pressure during infusion.

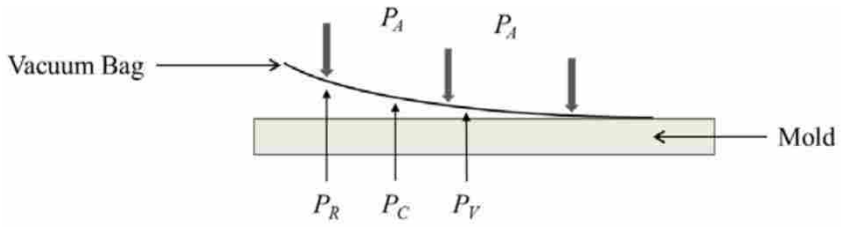

Figure 2-9: Pressures during vacuum infusion processing [23]

A simple force balance shows that atmospheric pressure is the sum of resin pressure, compaction pressure, and vacuum pressure:

$$P_A = P_R + P_C + P_V \tag{2-19}$$

When modeling P_C, it is common to use a power law to describe compaction pressure [15,17].

2.12 Void Formation and Mobility

Now that the background on flow characterization has been described, another key part of LCM simulation will be addressed: void formation and mobility. One of the purposes behind LCM simulation is to assist production quality. Part quality is often measured in terms of void content (v_C), or the percentage of non-matrix, non-reinforcement materials (typically gas bubbles) that remain in a composite after cure. Voids may form as entrapped bubbles, or may enter into a composite during infusion. It should be noted that v_C can be substantially reduced by way of degassing the resin prior to infusion and holding fabric under vacuum pressure long

enough to evacuate embedded gas and moisture. Expensive autoclave-prepreg processes reduce v_C by applying high pressures to parts and shrinking bubbles before parts cure.

By simulating how resin flows, researchers are able to better predict where there will be a local buildup of voids, and how to control void flow such that the part may perform optimally. This is one of the ways that LCM parts may reach a sufficiently high enough quality (i.e. low enough v_C) to make obsolete the expensive autoclave-prepreg parts, which are currently the standard for high-performance applications in aerospace.

The final two papers (Chapters 6 and 7) consider void content. The first addresses void flow behavior, and uses a recently developed technique for *in-situ* flow monitoring of carbon fiber by way of ultra-violet dye mixed into the injection fluid. This paper is regarded as one of the novel contributions of this dissertation because of its success in visualizing bubbles in carbon fiber during infusion so clearly that an abundance of *in-situ* results can be drawn, something that other research have not yet been able to accomplish. The second paper studies the cost of v_B by comparing a handful of important manufacturing processes.

3 PERFORMANCE OF ALT. SOLUTIONS FOR PERMEABILITY CALCULATION DURING ELLIPSOIDAL FLOW

3.1 Abstract

All three directional components of a reinforcement's permeability can be simultaneously characterized by monitoring point-infusion experiments through a stack of reinforcement material. The resulting ellipsoidal flow has been studied by multiple authors, and various solutions with which to calculate the permeability have been presented. Perhaps the most common criticism of this permeability measurement method is that most of these solutions introduce an error associated with initial flow front shape assumptions. This paper compares the accuracy of the available solutions in the context of 75 experiments representing a wide range of materials and test conditions. Modifications to available solutions are suggested, which simplify convergence and reduce the initial flow shape error. Modeling methods are presented, which allow determination of the full permeability tensor in one test while approximating an inlet-shape corrected solution.

3.2 Introduction

Flow simulation of LCM is commonly based on Darcy's Law [21] where the velocity of the flow front (v) through the mold is predicted by:

$$v = -\frac{K}{\varphi\mu}\nabla P \tag{3-1}$$

This requires the viscosity of the fluid (μ), the pressure (P) gradient, the porosity (φ) and the permeability (K) of the reinforcement material to be characterized [4]. The permeability represents the inherent capacity of a reinforcement architecture to allow flow through it [22]. It is often represented as an orthotropic three dimensional tensor [23] with two axes parallel with the reinforcement fabric surface and the third axis through the thickness of the fabric.

Measurement of the in-plane (with respect to the reinforcement fabric) permeability has been the topic of two international benchmarks [7,8]. Many variants of LCM are dominated by in-plane resin flow. For example, resin transfer molding (RTM) is a common composites processing method involving pressure driven flow through a two-sided matched metal-tooling mold. For these types of processes, flow simulation often neglects through-thickness flow as many parts resemble thin shells and the flow is dominated by in-plane flow.

Through-thickness flow may be significant in other cases of LCM, such as for components with part thickness variation, complex 3D part geometries, and inhomogeneous ply lay-up [24], as well as certain process variants such as vacuum infusion (VI), the vacuum assisted process (VAP), resin film infusion (RFI), or prepreg consolidation. Accurate simulation for these processes therefore requires the through-thickness (K_z) permeability. The measurement of K_z remains a more significant challenge than measurement of in-plane permeability values (K_x and K_y), due to less standardization of measurement methods, the high scatter in results [25], and the significant convolution of Darcy flow with wetting effects at the slow flow-rates [26] typical to such testing.

Many reported methods for the measurement of K_z force 1D flow through the thickness and measure either the pressure drop or flow rate [27,28]. Some of these methods involve 1D flow in a compression cell, enabling continuous measurement of K_z and compressibility for a range of volumetric fiber content ($v_F = 1 - \varphi$) [29-33]. Race-tracking is a challenge in 1D measurement [29,34]; care must be taken to avoid low-resistance flow paths in between the tooling and the sample edge. Screens or perforated plates are often used to hold the sample in place, but these cause the flow to deviate from unidirectional (UD) orientation [29]. In addition, most 1D tools are setup to only monitor saturated flow. While saturated flow measurements are more repeatable, they are not as representative of industrial infusion, where flow simulation must capture the movement of the flow front through the reinforcement [26,35].

More complex flow geometries can be utilized to measure K_z, where the weaknesses of 1D experimentation are alleviated. Many studies have employed an inverse estimation method to determine K_z by numerical flow simulation of a non-idealized flow geometry [34,36,37]. This method allows determination of the off-axis skew components of the permeability (e.g. K_{xz}) [38] although most permeability studies assume an orthotropic permeability tensor and neglect these terms.

Another alternative to 1D flow experiments for K_z measurement, which does not require explicit numerical simulation, is the point infusion method [34,37,39-44]. Flow is introduced through a tube into the top or bottom of a stack of dry reinforcement layers, and the resulting spherical (isotropic) or ellipsoidal (anisotropic) flow front is monitored. The term “point infusion” is only simplified nomenclature to distinguish this method from others; in reality, the flow originates not from a point source but from a circular inlet. This test method is more representative of actual composites processing than 1D testing, incorporating both wetting flow

and a multi-directional flow path. Minimal race-tracking results and all three of the diagonalized components of the permeability tensor (K_x, K_y, and K_z) can be simultaneously determined from one experiment.

In this approach, the *z*-direction flow-front is not so easily observed as with in-plane directional flow, as the fabric itself impedes observation. Embedded sensors have been used [37,39-42] to monitor flow progression, but such sensors have been shown to cause flow perturbations [28,42,45]. Other methods (ultrasound [44,46,47] and x-ray radioscopy [48]) require expensive equipment and calibration work. Thus, no practical method to measure *z*-direction flow through the reinforcement is available. However, by using a transparent mold base, the time at which the flow reaches the other side (opposite from the inlet) of the mold can be measured, giving at least one easily obtained data point of through thickness flow length at a given time.

However, this method also suffers from the drawback of inlet flow complications. Flow disturbances near the inlet are common for all *K* measurement methods, and require sufficient distance between inlet and measured flow front to minimize them. As with 2D radial testing [49], the shape of the 3D flow-front begins with the same circular shape as the inlet tube. Assuming that K_x, K_y and K_z have different values, the eventual 3D flow front will be ellipsoidal, and some flow length will be required to develop this ellipsoidal geometry, and thus infer correct values of the three permeabilities [6].

Another inlet flow issue is the point singularity phenomenon. Dual-scale fabrics, for example, will have different initial flow patterns based on the *x*/*y* location of the inlet tube; e.g. this will be affected by the number of channels or stitches that the inlet covers. But this error is also assumed to be mitigated far from the inlet. A small piece of flow media was placed between

the inlet and the reinforcement sample in previous studies [16,37], hoping to allow the correct flow front shape to develop sooner and to reduce the location-to-location point singularity error. No experimental results have yet been published to quantify or otherwise validate the effect of such flow media use. Also this strategy causes a non-ideal flow geometry thus complicating analysis by requiring the use of inverse estimation techniques with three-dimensional flow simulation.

When infused at constant pressure, any geometry of resin flow through a fabric experiences a decrease in flow front velocity with time. This is more pronounced in three dimensional flow due to the volume of reinforcement reducing the applied pressure [40]. Thus 3D permeability testing often involves slow flowrates, low resin pressures, and a more significant role of capillary effects [50,51]. The magnitude of the capillary pressure contribution to the pressure gradient is difficult to predict throughout a flow test, thus studies using 3D wetting tests have recommended only studying flow close to the inlet, where capillary forces are the lowest [40,42,45]. An optimal mold thickness is thus aimed for in such a test, where the flow has sufficient time to develop the correct ellipsoid geometry, but before the capillary pressure becomes significant [42].

Another complication of the point infusion method is that the calculations to simultaneously determine multiple permeability directions from a single test are more complex than for 1D permeability testing. Models have been presented in the literature for such ellipsoidal flow [6,39,42], yet little experimental data (e.g. flow front size at different times) is available [42] with which to evaluate those models.

This paper specifically assesses the practicality of various mathematical solutions for 3D flow, in the context of using the point infusion method for permeability measurement. A brief

outline for the paper may be presented as follows: (1.) Three available solutions to the point infusion method are presented: the analytical solution of Ahn et al. (Equation 3-3 below) [39], the numerical solution of Nedanov and Advani (Equation 3-5) [42], and the analytical inlet shape-corrected solution of Mekic, Akhatov and Ulven (Equation 3-6) [6]; (2.) The robustness of the numerical solution of Nedanov and Advani is examined, and a modified solution method is proposed to improve convergence (Equation 3-8); (3.) All four solution methods are compared for performance on a previously published dataset; (4.) Performance of the solutions is further investigated across a new compilation of 75 experiments in order to determine behavior across a variety of reinforcement types.

3.3 Ellipsoidal Flow Solutions

Modelling Darcian flow (through porous media) in an ellipsoidal geometry is mathematically taxing, and no closed-form solution that deals directly with this geometry has been presented thus far. Ahn et al., [39] were the first to present a solution to ellipsoidal flow by isotropic transformation, defining a coordinate transformation that converts the ellipsoidal shape (r_x, r_y, r_z) to spherical shape (r_x', r_y', r_z'):

$$r_x' = r_x\left(\frac{K_e}{K_x}\right)^{1/2},\ r_y' = r_y\left(\frac{K_e}{K_y}\right)^{1/2},\ r_z' = r_z\left(\frac{K_e}{K_z}\right)^{1/2},\quad K_e = \sqrt[3]{K_xK_yK_z} \tag{3-2}$$

This transformation allowed for a closed-form solution of Darcy's Law. At the flow front the isotropic (i.e. spherical in the new coordinates) flow radius is $r_x'= r_y'= r_z'=R'$. The equivalent isotropic permeability, K_e, determines the hemispherical flow in the transformed coordinate system. Integration with boundary conditions (based on pressures at the inlet and flow front) results in a closed form solution that is then transformed back to elliptical geometry by the

inverse coordinate transformation. The resulting equation gives the permeability for the flow front dimensions at a given time (t) [39]:

$$K_z = \frac{\mu\varphi {b_z}^2}{6t\Delta P}\left[2\left(\frac{r_z}{b_z}\right)^3 - 3\left(\frac{r_z}{b_z}\right)^2 + 1\right] \tag{3-3}$$

Where ΔP represents the pressure difference from inlet to flow front. Similar equations treat the x- and y-directions. Regarding the flow inlet radius shape, b_x, b_y and b_z, this solution requires the assumption of a fictitious ellipsoidal inlet shape, whose aspect ratio is held constant as the flow proceeds from the inlet through the reinforcement. In practice, such an inlet flow shape is impossible to establish. The inlet tube inner radius ($b_T = b_x = b_y$) is not ellipsoidal as assumed for anisotropic analysis, and b_z is not intuitive nor easy to measure. With such difficulties, $b_T \approx b_x = b_y = b_z$ was assumed in Ahn et al. [39], causing an error arising from the difference between the assumed elliptical shape and the actual initially hemispherical shape. However, as previously mentioned, this error decreases as the flow front moves farther from the inlet.

A later solution by Nedanov and Advani [42] adds a further flow rate equation, involving the pressure drop along the injecting tube, to those used by Ahn et al. [39], making the solution a system of three equations with three unknowns (K_x, K_y and K_z). Calculation of the permeability no longer involves independent closed-form solutions, such as in Equation 3-3. As this numerical solution's analytical expressions are complex, the variables are non-dimensionalized, following isotropic transformation (Equation 3-2), for simpler analysis. Non-dimensionalized variables are indicated by an overbar:

$$\bar{t} = \frac{tK_e\Delta P b_T}{C\mu\varphi h^3} = \frac{(1+C)}{3C}\left(\bar{R}^3 - \bar{b}^3\right) - \frac{\bar{b}}{2C}\left(\bar{R}^2 - \bar{b}^2\right),\ C = \frac{16K_eL}{{b_T}^3},\ \bar{b} = \frac{b_T}{h},\ \bar{R} = \frac{r\prime}{h} \tag{3-4}$$

where h is the thickness of the reinforcement sample after isotropic conversion (Equation 3-2) and L is the inlet tube length. Three equations result for the three flow directions by substituting each of the anisotropic flow radii from Equation 3-2, for r' in Equation 3-4. Given the nonlinear nature of the model, the authors elected to solve the equations by minimizing the derivative of the sum of squares with respect to C. The resultant least square method naturally formulates the model for regression-type fitting of the permeability, assuming that N data points can be obtained at different spatial and temporal points during an experiment [42]:

$$0 = \sum_{i=1}^{N} 2\left[\frac{(1+C)}{3C}\left(\bar{R}^3 - \bar{b}^3\right) - \frac{\bar{b}}{2C}\left(\bar{R}^2 - \bar{b}^2\right) - \bar{t}\right]\left[\bar{b}\frac{\left(\bar{R}^2 - \bar{b}^2\right)}{2C^2} + \frac{\left(\bar{R}^3 - \bar{b}^3\right)}{3C^2}\right] \tag{3-5}$$

Mekic, Akhatov and Ulven later presented a closed-form solution where a second transformation (after the isotropic transformation, Equation 3-2) is made to an oblate ellipsoid coordinate system [6], resulting in a series of equations that lead to the desired permeability:

$$\xi_f = \operatorname{acosh}\frac{r_x}{b_T},\quad K_{xye} = \sqrt{K_x K_y} = \frac{F(\xi_f) {b_T}^2 \mu\varphi}{t\Delta P},\quad K_z = \frac{r_z K_{xye}}{b_T \sinh\varepsilon_f} \tag{3-6}$$

In these equations, the (oblate) elliptical flow length coordinate and the in-plane isotropic permeability are represented by ξ_f and K_{xye} respectively. F is a hyperbolic function of ξ_f. This coordinate system allows the solution to include inlet shapes of non-ideal geometries, so the assumption of an ellipsoidal inlet is no longer required. This same transformation was previously used for 2D radial flow [52]. This solution's only significant drawback is that the three permeability components cannot all be determined in a single test as they can with all other solutions; Equation 3-6 can only calculate K_z and K_{xye}. Either K_x or K_y must be determined via an additional test (e.g. 1D flow test) in order to measure all three permeability components for anisotropic in-plane flow. The difference in theoretical flowrate between this solution and Equation 3-5 (with inlet flow simplification) was compared for multiple values of anisotropy

regarding one experiment published in [42] but no other quantification of the inlet shape assumption error was made.

Another study by the same authors [53] used the same oblate ellipsoidal transformation (Equation 3-6) for radial 2D tests, validated the approach against previous models, and showed that 3x higher anisotropy in the reinforcement resulted in approximately doubling of the error caused by the assumption of an elliptical inlet geometry in other solutions. Thus it is probable that the same situation applies also to 3D flow - that higher anisotropy causes greater error from ellipsoidal inlet shape assumptions in the earlier solutions.

3.3.1 Convergence of Numerical Solution

With the nonlinear least squares approach and the additional flow rate equation, Equation 3-5 is generally assumed to be more robust of a solution than Equation 3-3. But the iterations required to numerically solve Equation 3-5 can cause another difficulty compared to closed-form solutions. Nonlinear multivariable optimization algorithms, such as the Nelder-Mead simplex [54], require an initial guess for each of the dependent variables being fitted to the solution. The initial guess values for the simplex are perhaps best estimated by solving the analytical solution in Equation 3-3 [37]. This particular numerical solution (Equation 3-5) was shown to have a narrow minimum error at the solution for each of the three components of the permeability tensor [14], and the solution from Equation 3-3 is sometimes inadequate for convergence. Thus the initial guess values must be close to the solution, and can cause tedious “guess work.” Turner and Hjelmstad [55] demonstrated the difficulties of fine tuning the three initial values required to solve their modified version of Equation 3-3, with the Newton optimization method.

One method of examining the sensitivity of Equation 3-5 to the accuracy of the selected initial values involves varying the initial value of K_z around the true solution for all data points listed in Table 2 of [42] and resolving the equation. This is performed here for both all points in that dataset and using only the last data point (when flow touches the other end of the mold). The true solution for the former (all data points) is $1.41 \cdot 10^{-12}$ m^2 and $1.52 \cdot 10^{-12}$ m^2 for the latter (single data point). The selected initial guess values for K_x and K_y were left constant, and close to (within 20% of) the solution. 500 iterations of the permeability calculation were run by spacing the initial guess value for K_z from -80% to +500% of the solution (with 0% being equal to the solution). The resulting calculations of K_z are presented in Figure 3-1, with K_z=0 denoting no convergence. For the case using all data points, the initial value must be between -42% and +100% of the solution for convergence, and between -41% and +47% for the case using only the last data point. For initial values outside of these ranges, false solutions (local minima) exist, with the incorrect solution most often lying at $K_z \sim 4 \cdot 10^{-12}$ m^2. With permeability measurements often varying across orders of magnitude [8], this underscores the difficulty of guess-work in such optimization approaches. Note that this data only shows variation of one of the three variables; in practice estimates of all three permeability values would need to be accurate simultaneously. These difficulties regarding convergence seem to be magnified in lower permeability reinforcements. In the present authors' experience, determination of a valid solution using Equation 3-5 has proven to be impossible for many low permeability textiles.

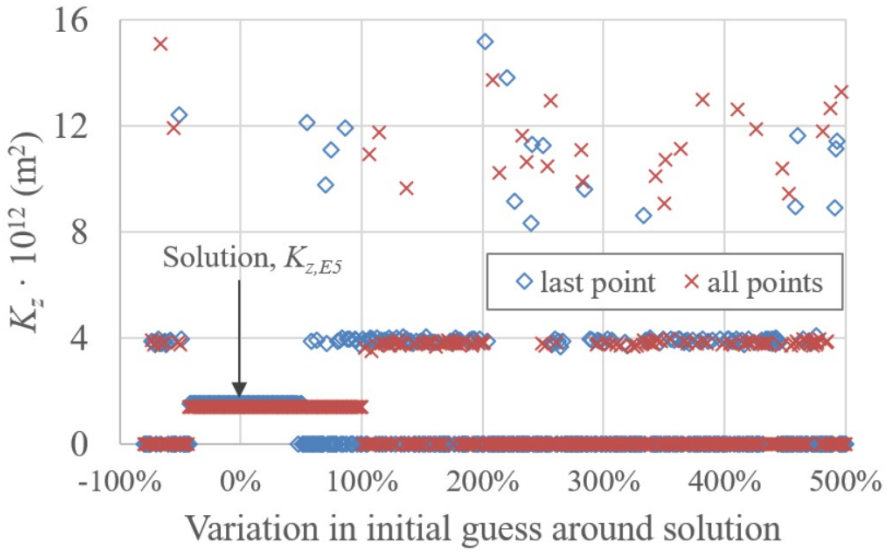

Figure 3-1: Calculated K_z by Eq. 5 for variation in initial guess around true solution, from -80% to +500% of solution; for both all reported flow lengths through thickness and only the last point, when the flow touches the opposite side of the mold. No convergence denoted by K_z = 0. Improved Numerical Approach: Ratio simplification solution

A simplification of Equation 3-5 is proposed here based on ratios between the permeabilities and squares of the flow radii in each of the three component directions [14]:

$$K_x / K_z = r_x^2 / r_z^2 \quad , \quad K_y / K_z = r_y^2 / r_z^2 \quad , \quad K_x / K_y = r_x^2 / r_y^2 \tag{3-7}$$

This same relationship was also suggested by Mekic et al. [6] to apply to Equation 3-5. A similar relationship has been used to simplify data analysis for 2D radial permeability measurement [56]. Mathematical validation of Equation 3-7 for 3D flow analysis is presented in the Appendix. This simplification reduces the isotropic permeability (after isotropic transformation) to a function of the transverse permeability and the ellipsoid shape:

$$K_e = K_z \cdot (r_x \cdot r_y / r_z^2)^{2/3} \tag{3-8}$$

This reduces the three-unknown optimization problem described in Nedanov and Advani [39], Equation 3-5, to a single unknown variable, which is mathematically much simpler to solve. This

allowed calculation of K_z for all the reinforcements discussed in this paper including many reinforcements for which the full three-unknown version of Equation 3-5 did not succeed at convergence. As will be illustrated in this paper, the difference between calculated permeability values from the three-unknown solution and the simplification by Equation 3-8 was insignificant.

3.4 Performance of Permeability Models against Empirical Results

The initial comparison of the four presented solutions is based upon the previously published experimental data sets of flow dimensions at incremental time values, for two experimental point-infusion tests under vacuum bagging, referred to hereafter as "N1" (Table 3 in [42]) and "N2" (appendix in [42]). Both of these experiments involved Vetrotex 5x4 plain weave e-glass (680 g/m^2) and a corn syrup solution for the test fluid. Slight differences in viscosity, pressure gradient, porosity, and inlet tube dimensions were reported for these two infusion tests. The viscosity and porosity averaged 0.12 Pa·s and 42%, respectively. To reduce the error caused by inlet size assumptions, $b_z = b_T\,[r_z\,(r_x\,r_y)^{-1/2}]$ was assumed for Equation 3-3, based on the inverse of the isotropic transformation in Equation 3-2; evaluation of this assumption is presented later in this paper. Equation 3-6 requires data from elsewhere for comparison of the resulting in-plane permeability, as it cannot calculate the individual in-plane components. K_y was used from another study on this same fabric by unsaturated 1D testing [57], and K_x was then determined by solving for it given K_{xye} from Equation 3-6.

3.4.1 Permeability Comparison

Figure 3-2 shows the resulting K_z calculations for each of the four solutions. The permeability is graphed against each time value of r_z/b_T (flow depth to inlet radius). K_z for Equation 3-3 is between the other solutions in Figure 3-2, with similar shape of the data plots.

For both N1 and N2 experiments, no difference can be seen between Equation 3-5 and Equation 3-8 in their respective calculated values for K_z. This was also the case for all other experimental data represented in this study, with the difference between the results never exceeding 1%. Thus Equation 3-5 results are omitted throughout the remainder of this paper.

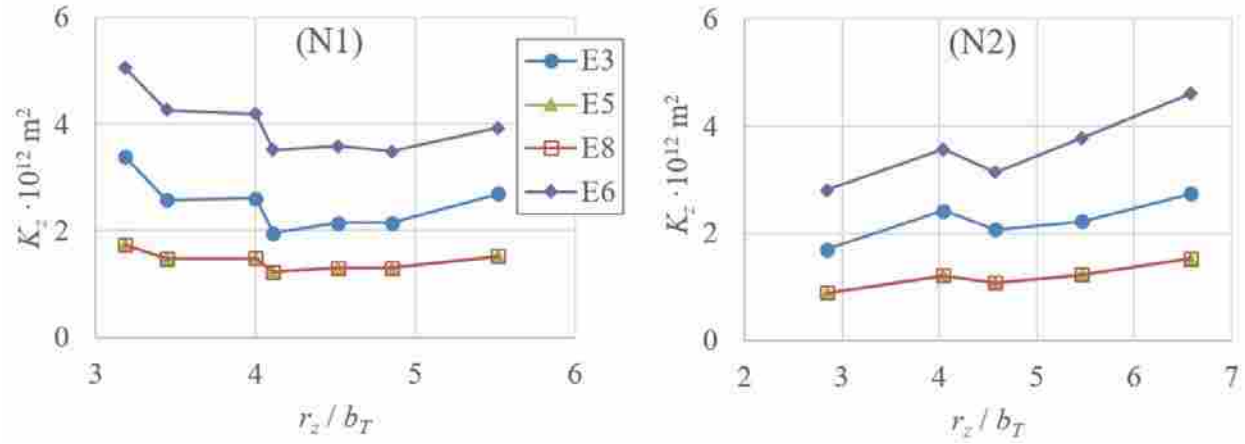

Figure 3-2: Resulting K_z for all four solutions.

Equation 3-3, -5, and -8 are designed to be used far from the inlet, to minimize inlet shape assumption errors; but at distances that are too far from the inlet, capillary forces become significant. Equation 3-6 is meant to correct the inlet size errors and thus the difference between that solution and the other solutions should decrease as the flow front progresses away from the inlet, or at least until capillary forces confuse the issue. Figure 3-3 displays the ratios $K_{z,Eq6}/K_{z,Eq3}$ and $K_{z,Eq6}/K_{z,Eq8}$ to examine the difference between the solutions as the flow progresses away from the inlet. A decreasing trend can possibly be seen for the comparison with Equation 3-8 in N1, all other comparisons give no clear trend. This fails to support the theory presented in [6] that the error caused by inlet shape assumptions should decrease as the flow moves farther from

the inlet. This range of flow length may be too short to show a difference, suggesting the need for further experimental data to validate this theory.

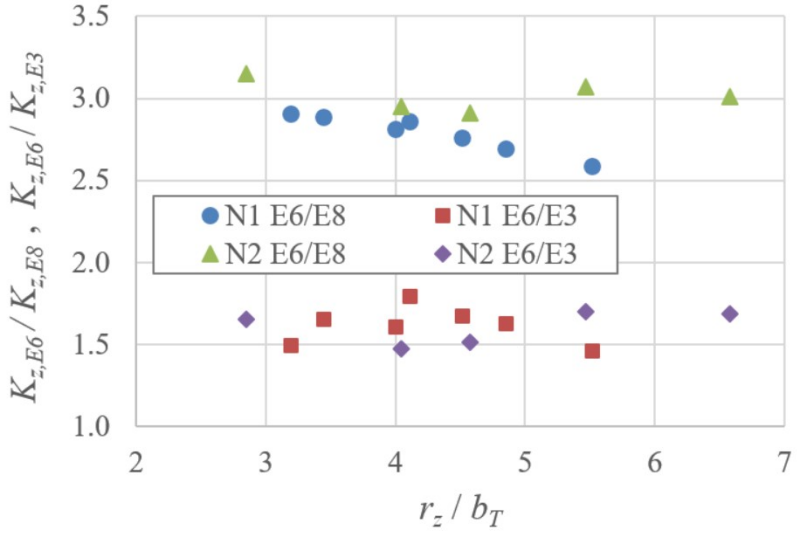

Figure 3-3: K_z for Equation 3-6 compared to Equations 3-3 and 3-8.

3.4.2 Anisotropy Comparison

The anisotropic permeability in the empirical tests causes the flow front shape to evolve from the circular inlet to its natural elliptical (in-plane) shape [45]. Thus the measured anisotropy should begin at 1 by the inlet, and then change from unity to the inherent anisotropy of the reinforcement as the ellipsoidal shape develops. Figure 3-4 illustrates the in-plane anisotropy, K_y/K_x as the flow front advances. For N1, the anisotropy does indeed begin at 1, increases, then seems to level off (parabolic shape) but is still increasing at the end of this experiment. The trend is not as clear for N2. Equation 3-3 and Equation 3-8 results show similar anisotropy and shape of plot in Figure 3-4. As these two experiments (N1 and N2) were made on identical materials and only slight differences in test parameters, the evolving anisotropy should be at least similar. Both experiments have an anisotropy of close to 1 for r_z/b_T of 3, and both show a general

increasing trend. The experimental data from N1 shows a faster increase in the anisotropy, implying that the in-plane ellipse increased in aspect ratio twice as fast as the N2 test sample. This difference is most likely due to the inherent variation in textile geometries for even the same reinforcement, which is at least partially to blame for the high standard deviation reported in permeability measurements. The difference could also possibly be due to differences in the fiber orientation schedule, which was not detailed in [42], e.g. whether the stack was laid up all in the same direction, or in a repeating [0/90] configuration.

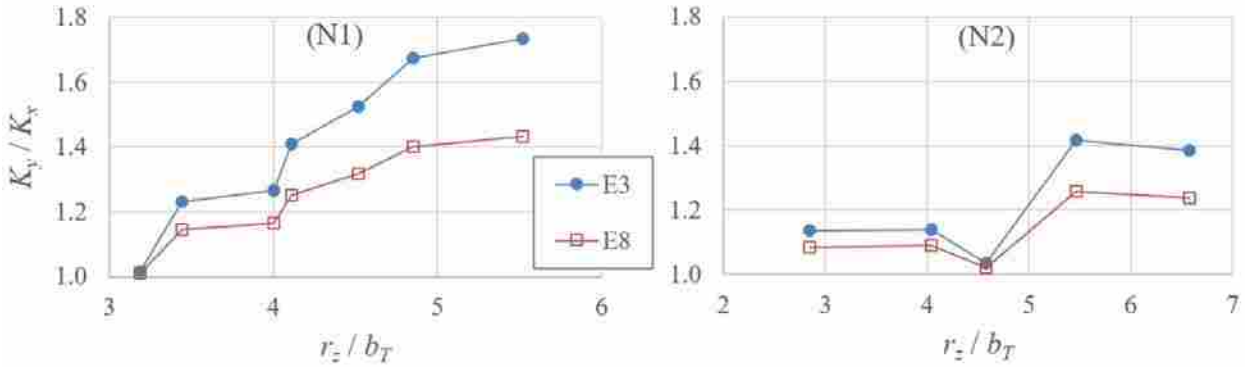

Figure 3-4: Anisotropy K_y/K_x for Equations 3-3 and -8.

The resulting anisotropy between the in-plane and through-thickness permeability was also compared, to look for any "weighting" of a particular solution to either through-thickness or in-plane flow. For this comparison, the equivalent in-plane permeability K_{xye} as defined in Equation 3-6 was used for all solutions. Although significant changes (-25% to +100%) occurred in K_{xye}/K_z between the experimental flow front observations (Figure 3-5), there was no clear trend in the changes, and all three solutions resulted in similar anisotropy for a given experimental measurement. This at least suggests that the mathematical solutions treat the

relative anisotropy of the flow in a nearly identical manner; the scatter in anisotropy is due to the flow front experimental data as opposed to choice of solution.

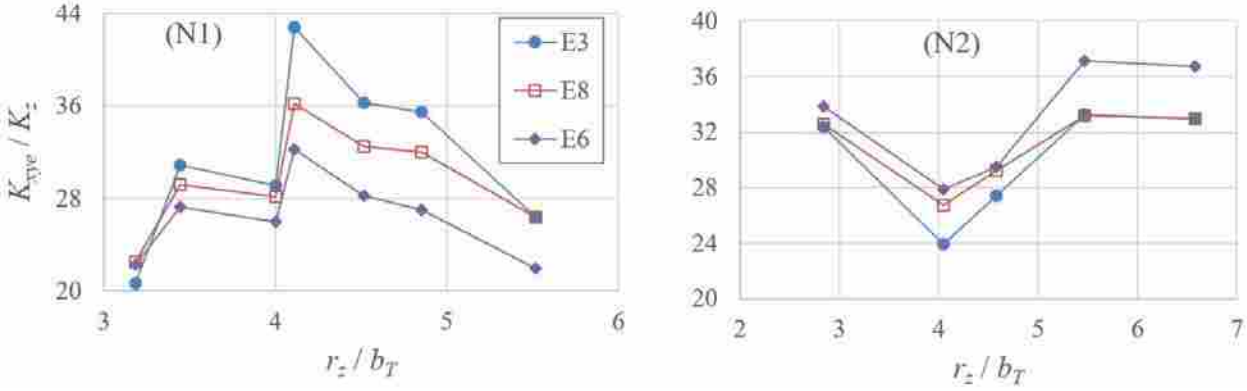

Figure 3-5: Anisotropy K_{xye}/K_z for all solutions.

3.4.3 Sensitivity of Inlet Size

One of the largest sources of error for the solution Equation 3-3 is associated with the assumption that the through-thickness length of the initial flow front (b_z) is equal to the tube radius (b_T). The sensitivity of Equation 3-3 to the assumed through-thickness shape of the initial flow front (b_z), for the last point in N1 is plotted in Figure 3-6. The inlet-corrected solution Equation 3-6 results in $K_z = 39.3 \cdot 10^{-13}$ m^2 for that experiment. Figure 3-6 presents the ratio of the resulting K_z from Equation 3-3 to this inlet-corrected value of K_z. Inspection of Figure 3-6 shows that assuming a b_z value of 0.37 mm in Equation 3 results in the same solution as that obtained by Equation 3-6, i.e. no error caused by the inlet-shape assumption in Equation 3-3. Various suggested formula for b_z have appeared in the literature, in attempts to make Equation 3-3 more accurate. The four individual points along the plot in Figure 3-6 represent: (1) $b_z = b_T$ [39], (2) $b_z = f(K_z / K_{xye})$ [6], (3) $b_z = b_T /10$ [40], (4) $b_z = b_T [r_z (r_x r_y)^{-1/2}]$. The latter option is the new formula presented in Section 3-3. The b_z value resulting in no error (0.37 mm) lies between the

latter two options above for b_z. All of the last three options put the calculated K_z from Equation 3-3 within 60% of that from Equation 3-6. The fourth option will be used with Equation 3-3 hereafter, as the first option yields higher error, the second option is more difficult to apply (requiring iterations), and the third option arbitrary.

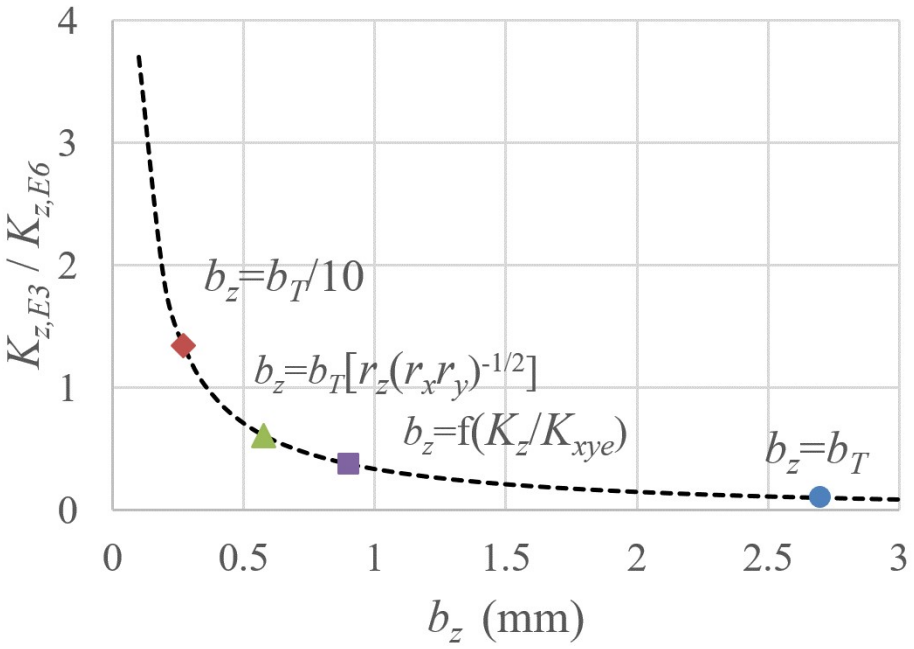

Figure 3-6: Calculated ratio of $K_{z,E3}$ (Eq. 3-3) to $K_{z,E6}$ (Eq. 3-6), with $K_{z,E3}$ evaluated as a function of the assumed value for b_z.

3.4.4 Validation of "Last-Point" Experiments

The data presented thus far (N1 and N2) was the only experimental point infusion data found in the literature with the flow front measured at multiple points through the sample thickness. The difficulties of through thickness flow measurement (Section 1) led the authors of that study to evaluate the agreement in results when only using the last point of data (when the flow touches the opposite mold side) and found favorable agreement [42]. This comparison is

made here again, for both data sets, as the percentage change from the calculated permeability using only the last point, to that from using all points (Figure 3-7).

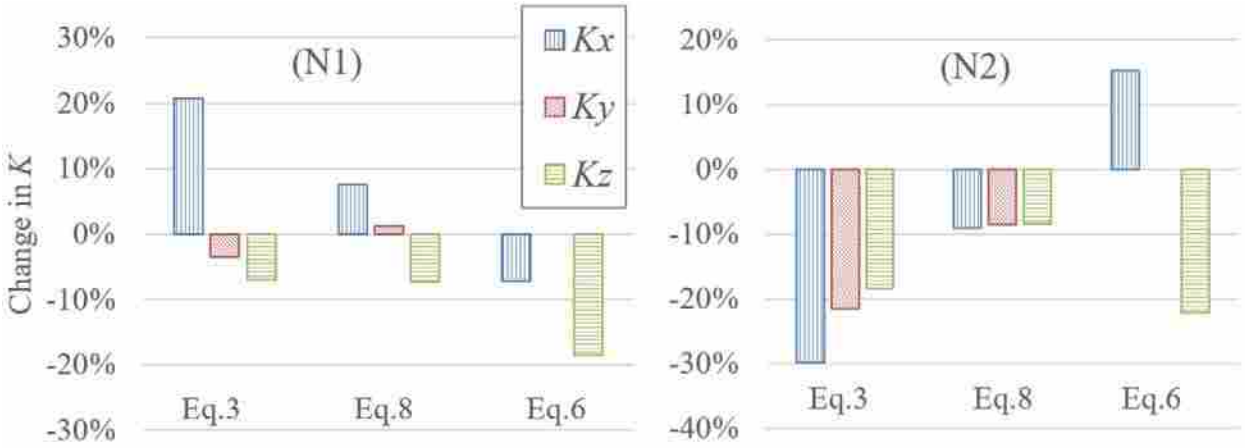

Figure 3-7: Change in permeability, from using only the last data point to all data points.

The results show very close agreement between the two approaches for Equation 3-8, and slightly less agreement for Equation 3-3 and -6. The maximum observed difference between the two methods (of 30%) is comparable to the experimental standard deviation for standardized in-plane 1D testing [8]. Thus, for any of these solutions, the efficacy of using only the last data point is further evinced. Such a conclusion also opens the way to analysis of further data sets for a much broader test of the applicability of the three solution methods; the remainder of this paper only applies the permeability models to “last-point” data.

3.4.5 Solution Performance for Large Dataset of Last-point Experiments

The data from various studies undertaken by the authors and collaborators, including 75 point infusion experiments, is represented here. Many experimental parameters were varied, including reinforcement choice, ply count and layup schedule, fluid choice and viscosity, and

applied pressure. The reinforcements vary greatly in permeability and anisotropy and are listed in Table 3-1 along with a code for each. The carbon UD weave test results (R4) have not yet been published elsewhere. This was point infusion testing of 8 to 32 ply stacks of 150 x 150 mm square samples, in either unidirectional or quasi-isotropic lay-up orientation, compressed to an average 65% v_F. A canola oil (μ = 55 mPa·s) was infused into the top of each sample with 85 to 100 kPa applied pressure gradient. Tooling consisted of both rigid and vacuum bagging setups, as described for other reinforcement tests in [43]. The test conditions for each of the other reinforcements are found elsewhere with respective citations in Table 3-1.

Table 3-1 – Reinforcements Studied

Code	Tests	Reinforcement Type
R1	2	Fiberglass 5x4 plain weave 680 gsm (N1 and N2) [42]
R2	9	Carbon biax NCF 580 gsm [43]
R3	9	Fiberglass UD weave 518 gsm [43]
R4	7	Carbon UD weave 292 gsm
R5	2	Carbon 2x2 twill 285 gsm [8]
R6	26	Carbon bindered UD weave 264 gsm
R7	6	Carbon bindered biax NCF 548 gsm [16]
R8	14	Carbon biax NCF 540 gsm and various others with same tows [14]

Figure 3-8 illustrates a comparison, similar to Figure 3-3, of the difference in solution for K_z between the different solution methods, but now based upon last-point data from all 75 experiments. The graph on the left gives the ratio of K_z solutions from Equation 3-6 and -8, while the right side represents the ratio of solutions between Equation 3-6 and -3. The first observation is that despite the multitude of test conditions and reinforcement types, the difference between Equation 3-6 and the other solutions is fairly uniform and does indeed decrease as the ratio of the

mold thickness to the tube inlet radius increases. This verifies the theory mentioned in Section 3.1 [6], with a much clearer trend than in Figure 3-3. The difference is approximately twice as large for Equation 3-8 compared to Equation 3-3, suggesting that the latter causes less error associated with the point geometry assumptions, when assuming $b_z = b_T\,[r_z\,(r_x\,r_y)^{-1/2}]$ in the latter. As this wide range of experimental conditions produced a fairly uniform power law relationship, the solution in Equation 3-6 without inlet shape assumption error could potentially be approximated using this power law function combined with either Equation 3-3 or -8.

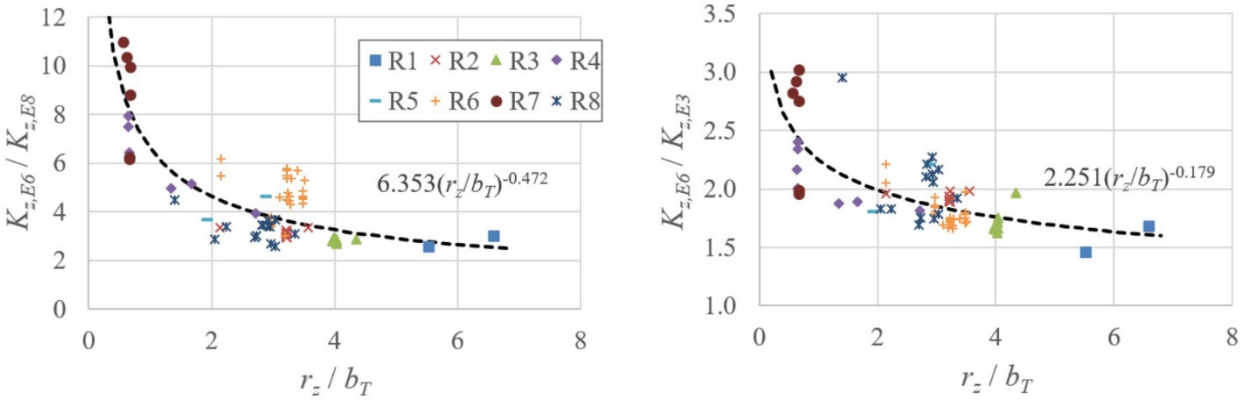

Figure 3-8: Ratios of values of Kz obtained from Eq. 3-6 and -8 (left) and Eq. 3-6 and -3 (right)

This prompted analysis of the solution comparison ratio, $K_{z,Eq6}/K_{z,Eq3}$ over a larger range of hypothetical flow front data. The ratio was evaluated as a function of r_z/b_T, using representative minimum and maximum values for the out-of-plane anisotropy (r_x/r_z = 2 and 8), as well as the in-plane anisotropy (r_x/r_y = 1 (in-plane isotropy), 1.5, and 2). This range of flow front dimensions is characteristic of the data in Figure 3-8. The agreement between solutions (Figure 3-9) increases with increasing out-of-plane anisotropy and decreasing in-plane anisotropy. The

latter result agrees with previous results for 2D radial testing [53] but the opposite result for transverse anisotropy (better agreement with higher anisotropy) is surprising.

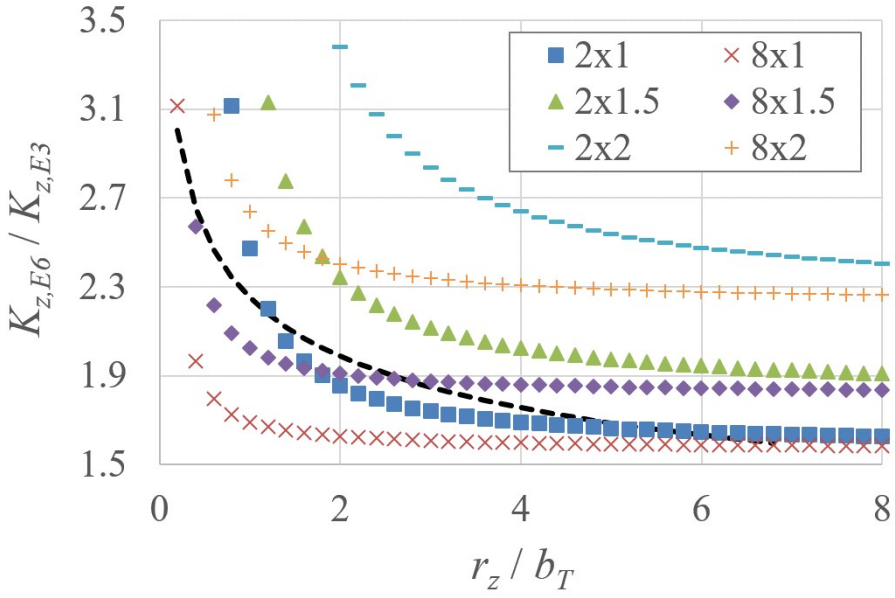

Figure 3-9: Evaluation of ratio $K_{z,E6}/K_{z,E3}$, for a range of flow front dimensions. "2x1" represents (first number) r_x/r_z and (second number (r_x/r_y); dashed line is model in Fig. 3-8.

Also seen in Figure 3-8 is that R1's two data points (from N1 and N2) are the highest r_z/b_T of all 75 tests. Thin samples used to be a concern in point-infusion testing as the flow may not have the time to develop its correct ellipsoidal geometry. But Equation 3-6 accounts for this error at low flow lengths. These results also suggest that the error significantly increases below $r_z/b_T = 2$, or when the fabric depth is less than twice the inlet tube diameter. These lower flow lengths may be desirable, as greater flow length causes an increase in effects of capillary pressure, causing all solutions including Equation 3-6 to incur error between the calculated permeability and that from saturated flow testing [50]. But it is clear that even at the flow profile farthest from the inlet (i.e. the highest r_z/b_T in this data), the point-infusion corrected solution

(Equation 3-6) still results in a minimum (best agreement) of 46% increase in K_z compared to the non-corrected solutions. While permeability measurement is often associated with high standard deviations [8], this difference would cause the same minimum 46% increase in filling time in flow simulation.

The corresponding comparison between Equation 3-6 and the other two solutions for the in-plane equivalent permeability, K_{xye}, is shown in Figure 3-10. Similar profiles to those in Figure 3-8 are seen, but the difference between the solutions is about twice as much for calculated values of K_{xye} as it was for K_z. Again, Equation 3-3 results in closer agreement to Equation 3-6 than Equation 3-8 does. A potential strategy to determine the individual in-plane permeability components from experimental data is to calculate the anisotropy (K_x/K_y) by Equation 3-3, calculate the corrected K_{xye} from Equation 3-6, then use the anisotropy determined by Equation 3-3 to calculate K_x and K_y from that value of K_{xye}. This assumes that the anisotropy K_x/K_y is determined correctly in Equation 3-3, but Figure 3-4 showed minimal differences between solutions for the transverse anisotropy, thus the same agreement is assumed for the in-

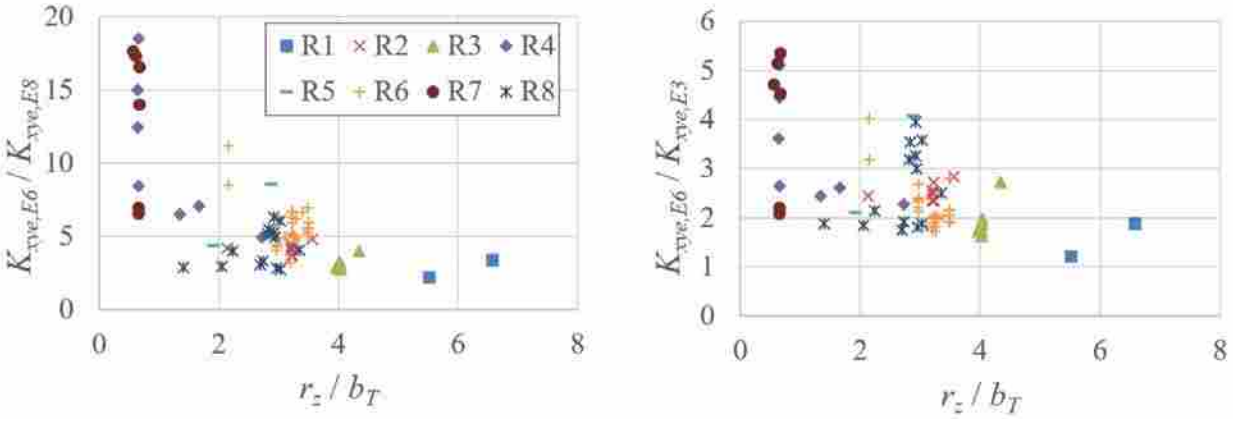

Figure 3-10: Comparison of K_{xye} from Eq. 3-6 to Eq. 3-8 (left) and Eq. 3 (right).

plane anisotropy. Another strategy is to apply the same ratio simplification, Equation 3-7 to this, by using the ratio of the flow front shape and $K_{z,Eq6}$ to determine K_x and K_y.

The ratio $K_{z,Eq6}/K_{z,Eq3}$ was also plotted (Figure 3-11) against the relative permeability ($K_{z,Eq6}$) as well as against v_F (fiber content). A lower permeability corresponds with less agreement between the point-source corrected solution (Equation 3-6) and the non-corrected solution (Equation 3-3). The slower flow in low permeability samples may delay the formation of the ellipsoidal flow front, making inlet shape assumptions more of an issue compared to high permeability reinforcements. The resulting trends are less clear for the fiber content. Higher fiber content is suspected to cause greater error in the non-corrected solution (Equation 3-6) as this usually entails a higher anisotropy and slower ellipsoid flow development. The lowest v_F test, a glass weave sample, does indeed result in one of the best agreements between solutions (lowest value of the ratio $K_{z,Eq6}/K_{z,Eq3}$), and the highest v_F test, a carbon UD weave sample, results in the worst agreement. But many of the tests in between those points have large differences between the two solutions despite being at relatively low values of v_F. This particularly applies to R6 and R7, the two bindered reinforcements. This suggests that the binder's effect of blocking the flow paths may exacerbate the problem of a slowly developing ellipsoidal flow front shape.

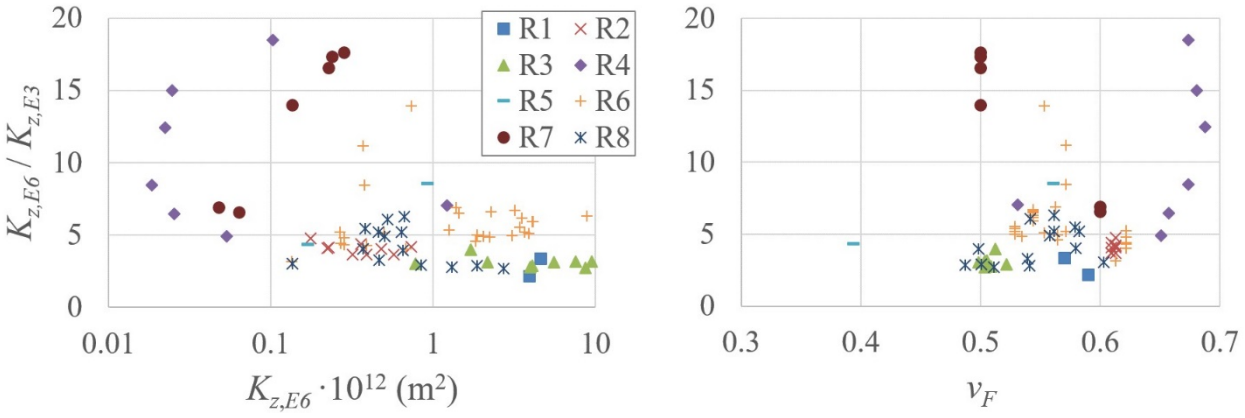

Figure 3-11: Ratio of ($K_{z,E6}/K_{z,E3}$) vs. $K_{z,E6}$ (left) and v_F (right).

3.5 Conclusion

The focus of this paper is to assess alternative models of 3D resin flow for the point infusion method of permeability characterization. Specifically, a much more complete quantification of the ellipsoidal inlet flow assumption error is presented than was previously available. Using data from previously published works, and 73 additional experiments of various reinforcement types, conducted by this paper's authors and collaborators, the assumption of ellipsoidal inlet flow is shown to reduce the calculated permeability by a minimum of 46%. The error caused by the ellipsoidal inlet assumption is minimized for flow farther from the inlet, and for higher transverse anisotropy, lower in-plane anisotropy, higher K_z, and lower v_F.

The error caused by the assumption roughly follows a power law trend with increasing flow length, for all reinforcements and test conditions. Thus a corrected permeability can be approximated by subtracting the modeled difference between solutions. A formulation of the Ahn et al. solution (Equation 3-3) for estimation of the through-thickness length of the initial flow front is given, which minimizes the error caused by the assumption of ellipsoidal initial flow.

Of the four solutions tested, the model of Mekic et al. (Equation 3-6), with correct handling of the inlet flow shape, is assumed to be the most accurate, but cannot be used by itself when measuring the full permeability tensor in a single experiment. Of the solutions which calculate all three permeability components, Nedanov and Advani's solution (Equation 3-5) may be more robust than that of Ahn, et al. (Equation 3-3), based on higher accuracy as the number of experimental measurements decreases. A simplification of the numerical solution by Nedanov and Advani (Equation 3-5) is also presented (Equation 3-8), reducing the dimensionality of the solution from three to one, thus greatly simplifying convergence. However, the solution from

Ahn et al. (Equation 3-3) results in the least error caused by ellipsoidal inlet assumptions when using an assumed value of b_z proposed in this study.

This study does not account for capillary effects at high flow lengths, and does not evaluate the solutions for accuracy against 1D test results. These results are only meant to comparatively evaluate the utility of the different solutions, while the flow is still close enough to the inlet to minimize capillary effects.

3.6 Funding

GKN Aero Engines and VectorPly contributed materials to this study. A portion of the experimental work presented in this study was supported by Sweden's NFFP5-KOMPLETT. The analytical work was supported by NSF grant CMMI 1538447.

3.7 Appendix

For any instantaneous time t during resin flow, if a point is considered on each of the three flow ellipsoid axes, (x,0,0), (0,y,0), (0,0,z) such that the normalized positions with respect to the flow front positions (r_x, r_y, r_z) are equal:

$$x/r_x = y/r_y = z/r_z = \alpha \tag{3-A1}$$

then:

$$\frac{\partial \alpha}{\partial x} = \frac{1}{r_x} \;\therefore\; \frac{\partial P}{\partial x} = \frac{\partial P}{\partial \alpha}\frac{\partial \alpha}{\partial x} = \frac{\partial P}{\partial \alpha}\frac{1}{r_x} \tag{3-A2}$$

where P is the pressure of the infiltrating fluid, and correspondingly $\partial P/\partial z = \partial P/\partial \alpha \cdot 1/r_z$. The flow velocity in any direction is predicted by Darcy as a function of the pressure gradient at the

flow front, either $\partial P/\partial x$ along the x-axis of the flow ellipsoid, or $\partial P/\partial z$ in the through-thickness direction. Thus:

$$\frac{\partial r_x}{\partial t} = \frac{K_x}{\mu\varphi}\frac{\partial P}{\partial x} = \frac{K_x}{\mu\varphi}\left(\frac{\partial P}{\partial \alpha}\frac{1}{r_x}\right), \quad \frac{\partial r_z}{\partial t} = \frac{K_z}{\mu\varphi}\left(\frac{\partial P}{\partial \alpha}\frac{1}{r_z}\right) \tag{3-A3}$$

The pressure profile $P(\square)$ between inlet and flow front was previously shown for one- and two-dimensional flow to appear as approximately the same line or curve for various flow front lengths [15]. This implies that $\partial P/\partial \alpha$ at any given normalized position ($\square$) remains constant with respect to time. It is generally assumed that the same would apply to three-dimensional flow as well. Hence, Equation 3-A3 can be integrated by separation of variables. Here, $\partial P/\partial \alpha$ is assumed to be equal for each of the three principle directions, as the shape of the flow front ellipsoid is assumed to be constant by the solutions mentioned above, and the inlet and vent pressures are constant in any direction. Also assuming homogeneous μ and φ, after integration:

$$\frac{2t}{\mu\varphi}\frac{\partial P}{\partial \alpha} = \frac{r_x^2}{K_x} = \frac{r_z^2}{K_z} \tag{3-A4}$$

This suggests that the ratio between the permeability components is equal to the ratio between the squares of the flow lengths in each component direction (Equation 3-7).

The ratio in Equation 3-A4 can also be proven from a model for the pressure distribution. All closed-form solutions to evaluate ellipsoidal flow have been based on isotropic transformation to spherical flow. The validity of this approach is based upon the assumption that the pressure distribution in any axis' direction in ellipsoidal flow is similar to that for spherical flow. The pressure distribution for spherical flow can be determined from integration of the spherical coordinate version of Darcy's Law combined with conservation of mass [39,40]:

$$P(x) = \frac{\Delta P\, r_x\, b_x}{r_x - b_x}\left(\frac{1}{x} - \frac{1}{r_x}\right) + P_r, \quad P(z) = \frac{\Delta P\, r_z\, b_z}{r_z - b_z}\left(\frac{1}{z} - \frac{1}{r_z}\right) + P_r \tag{3-A5}$$

where P_r is the pressure at the flow front and in the dry reinforcement. The pressure gradient at the flow front is what determines the instantaneous flow velocity as per Darcy's Law. Taking the derivative of each side in Equation 3-A5, and substituting the flow front length for the position in each, gives the pressure gradients at the flow front:

$$\frac{\partial P}{\partial x} = \frac{-\Delta P\ b_x}{r_x(r_x - b_x)}\ ,\ \frac{\partial P}{\partial z} = \frac{-\Delta P\ b_z}{r_z(r_z - b_z)} \tag{3-A6}$$

Substituting these pressure gradients into Darcy's Law (as done in Equation 3-A3), relating the two sides (directions) above through their equality with $\Delta P \cdot \partial t/(\mu\varphi)$, and integrating, gives a more complex relationship between K_x and K_z than shown in Equation A4:

$$\frac{3r_x^3 - 2r_x^2 b_x}{K_x b_x} = \frac{3r_z^3 - 2r_z^2 b_z}{K_z b_z} \tag{3-A7}$$

However, if the ellipsoidal inlet shape assumption from the solution of Ahn et al. ($b_x/b_z = r_x/r_z$) [39] is applied, then Equation A7 reduces to the same ratio in Equation 3-A4.

4 PERMEABILITY OF UNIDIRECTIONAL WEAVE CARBON FIBER WITH VERTICAL CURVATURE

4.1 Introduction

Liquid composite molding (LCM) is of growing importance as an alternative to traditional prepreg-autoclave methods for manufacture high-performance composites. Such optimization can be facilitated through use of flow simulation, which requires that the permeability of the reinforcement be characterized. Permeability measurement methods are well represented in the literature, but usually involve undeformed reinforcement geometries, i.e. flat and unsheared. The high performance composites industry rarely employs parts however with such geometries. Double curvature and bend radii are common. These deformations of the reinforcement may lead to significant changes in the local permeability of the reinforcement, as well as the mechanical properties. The accuracy of flow simulation may be improved by accounting for these changes to permeability for a given part geometry. This requires that the permeability not only be measured in its undeformed state, but that models be developed to describe the permeability for a range of reinforcement deformations.

4.2 Overview

In cooperation with an aerospace company, the research at hand seeks to characterize a carbon fabric (Vectorply C-L 0900) in terms of local permeability in areas of curvature. Other

researchers have sought similar knowledge, but considering multiple radii of curvature, as well as monitoring flow and pressure over tooling corners and triangular plates. These methods have almost all been rigid-mold processes. And fabrics used have nearly always been fiber glass. No researchers have characterized the permeability of highly-packed unidirectional (UD) carbon fiber weaves over cured molds using vacuum-assisted resin transfer molding (VARTM) tooling. Furthermore, most experiments have involved elevation change in their infusion flow paths, such as flow that curves from a horizontally flat to a vertically flat region. These do not address how flow behaves when traveling laterally on a vertical planar surface.

The research at hand aimed to progress the state of art to include by characterizing the permeability of fabric with local curvature for a high-aerial weight UD weave carbon fiber reinforcement. The goal was to determine the effective local permeability of a curved region of fabric. This was done using VARTM tooling with constant-elevation curved flow around a vertically-oriented curve (1-D flow). Four different radii were evaluated: 1.6, 3.2, 6.4, and 25.4 mm.

4.3 Literature Review

Early research on curved fabrics indicated that curvature affects the pressure required to infuse fabrics increases when curves are included in the tooling [58]. The method used is called Liquid/Air Displacement analysis. While this did not produce permeability data, the increase in pressure recorded was likely the result of a locally lower permeability of the fabric at the curved region. Two years later, Friedman measured the LCM flow over a rigid L-shaped tool, showing that permeability does in fact decrease in areas of curvature [59]. This L-shaped tool became common for curved testing, and others followed suit with a similar experimental design [60-63].

In order to address the effects of gravity in the vertically-oriented section of the L-experiment, hydrostatic pressure was incorporated into calculations [64].

Bickerton also did substantial work on curvature and its effects on local fabric permeability [65,66]. His first work examined the effects of different radii molds on a fabric layup. These were conducted with a two-sided mold, and showed that resin-rich areas form at curvatures, but did not define permeability for curved regions. His work also consisted of a radial infusion test set on top of a triangular ridge mold with three curved regions. Results showed significant flow problems due to small anomalies in tooling tolerance at the corners.

Anomalies included race-tracking, resin-rich zones, and sometimes entirely blocked flow (due to high compression) [65]. It is also important to point out that the reduction in permeability over curved regions has often been attributed to local compression [67]. Compression leads to an increased fiber volume fraction, v_F. As v_F of a fabric increases, fibers are pressed more closely together. Increased v_F leads to a decrease in porosity, by the relationship $\varphi = 1 - v_F$. A theoretical limit for v_F of UD fibers is 0.91%. However, a practical limit is 0.80. The maximum v_F was reported to be 0.40 for random fibers [68].

In 2011, Causse began researching the effects of flexible injection (i.e. when a matrix is infused from out-of-plane due to a pressurized flexible tool wall) [69]. The research considered how part quality was affected with curvature, and showed that strong curvature regions exhibit manufacturing defects; sharp corner regions are likely to experience resin build up (for concave corners) and thinning of fabric (for convex corners). Causse suggested preforming techniques to address thickness issues at corners [70]. Hubert also examined the causes of corner thickness deviation [71].

The knowledge gained by early researchers was fundamental to understanding LCM flow over curvatures, but not sufficient for LCM simulation. For such simulation, a model needed to be developed which would predict permeability of curved regions. This is especially valuable for carbon fiber reinforcement fabrics due to their use in high-performance applications.

Some simulation modeling work was created by Lawrence in 2002, where he examined developed an adaptive model for rigid tooling with curvature. The model would adjust so as to define race-tracking, which is the phenomenon when infusion fluid moves significantly faster than anticipated due to small open channels [72]. Nakatani also recommended that gaps around sharp fabric corners need to be modeled in order to more accurately simulate reinforcement saturation [73]. Other researchers have explored modeling of permeability of fabrics with local curvature [44,73,74]. In 2014, Wendling pointed out the need for improved characterization of dry fabric composites by modeling due to high shear, tension, and curvature because of their effect on permeability and part quality [75]. Many researchers have studied how to implement a fabric unit cell in permeability prediction. Sas suggested the creation of a unique zone (or mesh region in simulation) to apply deformation-induced changes in permeability [74]. Bickerton suggests using an anisotropy ratio (K11/K22) in order to model simulation, explaining if the ratio is correct, simulation will be sufficiently accurate even if actual permeability err by orders of magnitude [65].

All research previously conducted on the permeability of locally curved reinforcements has considered only horizontally-oriented curves. No permeability experimentation has been conducted on a vertically-oriented curved region. Furthermore, no published VARTM testing has examined the local permeability effects of a vertically-oriented curve.

4.4 Method

4.4.1 Darcy's Law

Permeability characterization began with Darcy's Law, which serves as a model for fluid flow through a porous medium [4]. This was based on assuming creeping, incompressible flow (Stokes flow, $Re \ll 1$), where high viscosity dominates typically behavior (Ca > 10e-5). For 1D flow through a laterally-oriented channel, the gravity source term effects were regarded as negligible by measuring flow in the center of the channel (as gravity acts perpendicular to the flow direction and is negligibly small along the infusion length):

$$Q = \frac{K_x A}{\mu}\left(\frac{\partial P}{\partial x}\right) \tag{4-1}$$

Here Q is the volumetric flowrate, K_x is the permeability tensor (1D in this case), A is the area of the cross section perpendicular to flow, μ is fluid viscosity, and $\partial P/\partial x$ is the pressure gradient in the flow direction. (A more in-depth discussion of K_x and permeability is provided in the Appendix.) Using the relationship $Q/A = u = \partial L/\partial t = q/\varphi$, where q is volumetric flux and φ is porosity, and u the local experimental velocity of the flow front seen through the vacuum bag:

$$u = \frac{\partial L}{\partial t} = -\frac{K_x}{\varphi\mu}\left(\frac{\partial P}{\partial x}\right) \tag{4-2}$$

Assuming a linear pressure gradient over the region under consideration, $\partial P/\partial x$ changes to $\Delta P/L$. Solving for K and integrating $\partial L/\partial t$ over a region:

$$K_x = \frac{u\varphi\mu L}{\Delta P} \tag{4-3}$$

By re-writing u as dL/dt, separating and integrating, the standard equation for measuring 1D permeability is obtained [8]:

$$K_x = \frac{\varphi \mu L^2}{2\Delta pt} \tag{4-4}$$

This is the equation used to measure local permeabilities. Before further detail on permeability measurement can be given, a description of the tooling and regions must take place.

4.4.2 Tooling and Flow Over Vertically-Oriented Curvature

Instead of measuring flow across a flat sample, as in [8], the flow was measured across a fixture such as that illustrated in Figure 4-1. However, the experiment was different in that it contains curvature, and is vertically oriented. Saturated fabric is shown as brown, and unsaturated is shown in black. The curved fabric region, *R2*, is bounded by *L1* and *L2*. The experiment was similar to previous experiments in that 1D flow equations were used, and the sample was rectangular, with a square flow front.

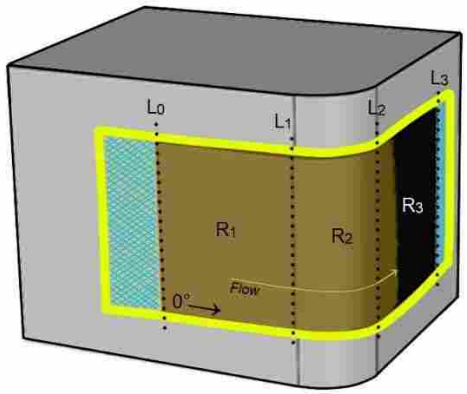

Figure 4-1: Curved tooling showing resin infusion for VARTM-type test over vertically-oriented curvature. Resin enters on the right and flows to the left, driven from atmospheric to vacuum pressure.

Fabric samples were made from Vectorply C-L 0900 UD weave fabric. Each sample cut to be 127 mm long and 76 mm wide, with a ply schedule of $[0]_8$ i.e. reinforcement machine direction aligned with the flow direction. Infusion was made under a vacuum bag with sealant tape applied immediately adjacent to the sides of the fabric to minimize race-tracking. Race-tracking is when unanticipated flow channels lead to accelerated flow, disrupting experimentation. By placing sealant tape adjacent to fabric, the fabric was able to compress flush against the seal. Infusions used canola oil at room temperature as a test fluid, with a viscosity of approximately 60 mPa·s. This fluid was chosen as it approximates the viscosity and chemical functionalities of an infusion grade resin and is common in permeability experimentation. The infusion was driven by vacuum pressure (less than 10 mbar absolute) at the vent with ambient pressure (approximately 860 mbar) at the inlet pot of oil.

During infusion, the times t_1, t_2, *and* t_3 were recorded. These are defined as the times at which the slowest point of the flow front crossed positional lines marked L_1, L_2, *and* L_3, respectively (Figure 4-1, L_0 is included for reference). Each test included a flat initial region, a curved region, and a flat final region. These regions are referred to as R_1, R_2, and R_3, respectively (also in Figure 4-1), and are bounded by L_0, L_1, L_2, *and* L_3. The region R_2 represents the curved region. Because different radii were considered, but total sample lengths were the same, R_2 and R_3 had different lengths for each radius.

During each test, data sheets were collected tracking information about consistent experimental set-up. These included tooling time held at vacuum prior to infusion, the height of resin with respect to the sample, oil temperature, vacuum pressure, inlet tube length, tube depth, layup, initial oil height, oil volume, height of flow front, times to lines (*L1*, *L2*, and *L3*), final oil height whether the curved fabric region experienced bridging or wrinkling, whether oil bulging

occurred, whether vacuum bag leaking occurred and where, and whether racetracking was evident. All of these parameters were controlled so as to generate consistent data. Samples experiencing racetracking or visible fabric bulging were removed from the data. Bulging is a term used to describe when the vacuum bag lifted off of the sample after fabric saturation due to being too loosely set up during experimental set up. Bulging always occurred when the samples were infused below the level of the oil/resin pot. When samples were infused above oil/resin pot, bulging was rare and the flow front was flat. Racetracking occurred when samples were unevenly cut or when the seal was not placed correctly so as to allow unanticipated locally fast flow.

4.4.3 Gravity and Hydrostatic Pressure

Earlier researchers have addressed hydrostatic pressure as effecting the pressure gradient of a sample in the direction of fluid flow. In a vertical region with vertically-directed flow, gravity and hydrostatic pressure would lead to accelerated or decelerated flow of loosely packed fiberglass tested. The research at hand differs from previous methods by considering flow perpendicular to gravity, where the effects of gravity and hydrostatic could be minimal.

To address the effects of gravity and hydrostatic pressure observations were made regarding flow in this experimental set up. First, it was noted that the flow-front was uniformly flat whenever the VARTM sample was infused above the surface of the canola oil. Because of the flat flow front, the effects of gravity were assumed to be negligible. Second, to address hydrostatic pressure, a simple calculation was made. With a height of 76 mm, and canola oil density of 0.92 g/ml, the maximum hydrostatic pressure difference experienced between the top and bottom sides of the sample would be 0.686 kPa. The inlet pressure was atmospheric at

mountain altitude, (~85 kPa), and the outlet was at vacuum pressure. Thus the hydrostatic pressure due to sample orientation was more than two orders of magnitude less than atmospheric pressure. This led to the assumption that hydrostatic pressure was not significant and could be ignored.

4.4.4 Harmonic-Average Permeability

Now that the measurement method has been addressed, the harmonic-average permeability computation can be presented. It accounts for regions with discrete permeabilities and pressure drops. This is standard for evaluating the permeability of regions in series, and assumes a constant pressure drop for each region:

$$\Delta P_{tot} = \sum_{i=1}^{n} \Delta P_i \tag{4-5}$$

The harmonic-average permeability equation is given by:

$$\frac{K_{ave}}{L_{tot}} = \sum_{i=1}^{n} \left(\frac{K_x}{L}\right)_i \tag{4-6}$$

In this equation, K_{ave} is the average permeability up to the total length, L_{tot}. The ratio, $(K_x/L)_i$, is unique for each region in series, with K_x as the local permeability and L as the region length. By knowing K_{ave} for *R1*, *R2*, and *R3*, one can then compute respective local permeabilities. After using the harmonic-average permeability equation, drastically different K_x were obtained for *R1* and *R3*, which should have had identical permeabilities.

4.5 Results

Results from computing regional permeability for the vertically-oriented set up were obtained. Results from the curved regions were organized into a model to assist in understanding

the nature of curved region permeability for the UD weave carbon fabric studied. The validity of the model was then addressed using compressibility. A discussion of results is provided in the following section.

4.5.1 Model of Curvature Reduction of Permeability

The harmonic-average permeability results are shown for four different radii in Figure 4-2. Regions *R1* and *R3* are the planar regions of the sample, while *R2* is for the curved region. Error bars indicate common error of 25% seen in 1D permeability testing [8]. An illustration of the tooling can be found in Figure 4-1. Curved regions (*R2*) showed an overall decrease in K_x for *R2*

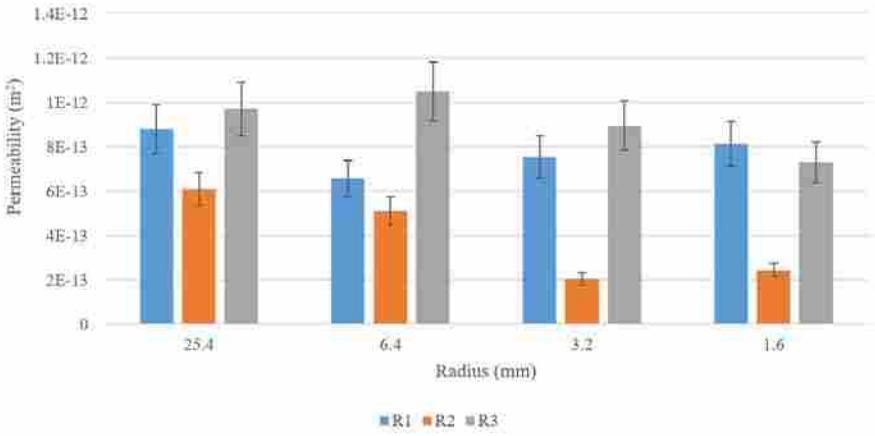

Figure 4-2: Harmonic-average K_x measured over four radii. R1 and R3 were flat non-curved regions. R2 was a region with local curvature of indicated radii. Error bars are set to 25% (such as are common in K_x testing).

across decreasing radii, with radii of 3.2 mm and 1.6 mm showing similar *R2* permeabilities. The two planar, non-curved regions (*R1* and *R3*) saw an increase in K_x for radii greater than 1.6 mm. The average increase in K_x between presumably identical regions was ~20% for four tests, with the maximum being ~60% for 6.4 mm and the minimum -10% for 1.6 mm.

A model for the effects of curvature on local permeability are shown in Figure 4-3. The model presents the measured permeability of *R2* for four different radii. Dotted lines are shown to suggest possible values of K_x by logarithmic (not linear) interpolation. A likely maximum would occur in flat, un-curved fabric and could be expected to resemble the average of regions *R1* and *R3* (~ 8.4E-13 m^2).

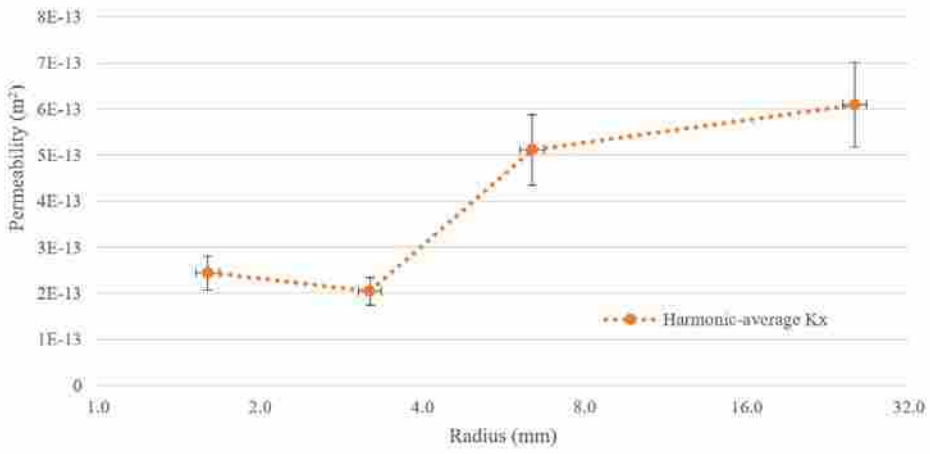

Figure 4-3: Model of K_x for locally curved fabric over vertically-oriented curvature

4.5.2 Model Validation

In order to address fabric compression as a potential cause of the decrease in K_x with decreasing radius, ratios of $K_{x,R2}/K_{x,R1}$ were determined. These ratios are shown in Table 4-1. A connection between ratios and their corresponding v_F is then given to address feasibility.

Table 4-1: Ratios of curved- to flat-region local permeability

Radius (mm)	$K_{x,R2}/K_{x,R1}$
1.6	0.30
3.2	0.27
6.4	0.78
25.4	0.69

First, it was necessary to determine whether the reduction in permeability seen over curved regions is possible. Recall that $\varphi = 1 - v_F$. Equation 4-4 shows that, with all else constant, permeability is proportional to porosity. Porosity then must decrease with curvature to such an extent that the ratios seen in Table 4-1 are feasible. Assuming compression as the only cause of reduction in porosity, it would be logical to conclude that

$$\frac{K_{x,R2}}{K_{x,R1}} = \frac{\varphi_{R2}}{\varphi_{R1}} = \frac{1-v_{F,R2}}{1-v_{F,R1}}, \tag{4-7}$$

where $K_{x,R2}$ and $K_{x,R1}$ are the respective permeabilities of *R2* and *R1*, φ_{R2} and φ_{R1} are the respective porosities of the *R2* and *R1*; $v_{F,R2}$ and $v_{F,R1}$ are also the respective volume fractions. Therefore,

$$v_{F,R2} = \frac{K_{x,R2}}{K_{x,R1}}\left(1 - v_{F,R1}\right). \tag{4-8}$$

Equation 4-8 and Table 4-1 can be combined with the expected flat region volume fraction, $v_{F,R1} = 0.54$ [76]. Data in Table 4-2 shows the required curved volume fractions for different radii in order to obtain the measured flow behavior. This data is based on the two models discussed. The UD weave carbon fabric studied has a theoretical minimum volume fraction of 0.35 [76] and a theoretical maximum volume fraction of 0.91 [68]. Research has shown a realistic maximum of ~0.80 for UD fibers [68].

Table 4-2: Required curved region volume fractions if $v_{F,R1} = 0.54$.

Radius (mm)	Required $v_{F,R2}$
1.6	0.86
3.2	0.88
6.4	0.64
25.4	0.68

4.6 Discussion

The aim of the research was to develop a model to represent permeability of locally curved carbon fiber fabric vacuum infused around a vertically-oriented curve. A model was developed which shows a decrease in permeability with decreasing radius for the highly-packed UD weave carbon fiber. This model can be applied to LCM simulation in curved zones to improve accuracy of flow predictions.

To calculate the permeability of regions in series, the harmonic-permeability method, was used. The permeability of locally curved fabric regions were reasonable in terms of compressibility as the explanation; the permeabilities of *R2*s corresponded with fiber volume fractions within the theoretical upper and lower limits. For 3.2 mm radius curvature, however, $v_{F,R2}$ came within a 3% of the theoretical maximum and was 6% above the realistic maximum [68]. This suggests that there may be other factors at play other than pure compression. A possibility could be that as fabric compressed, flow channels may have become narrow enough for flow to be less viscosity driven and more capillary force driven.

An evaluation of data sheets recorded during flow experimentation sheds some light on possible other factors affecting the permeability of vertical fabric under vacuum bagging. Two experiments were removed from the data set because of extreme racetracking between the top

face of the fabric and vacuum bag. This was referred to as bulging in the data sheets, because the vacuum bag appeared to fill with resin and bulge away from the sample. Bulging occurred when the sample was positioned at any height below the level of oil in the resin pot. For the data shown, no bulging was visible. The flow fronts were flat and reasonably uniform. The shape of a flow front stayed flat and vertical during the infusion. A change in preform thickness was also not visually observed.

Nevertheless, the thickness of samples was not measured during infusion, and could have changed minimally. An increase in sample thickness (i.e. an invisible bulge) would increase permeability in *R1* and that effect would carry over and lead to increased K_x in *R2* and *R3*. This may have accounted for the increased permeability in *R3*. These behaviors are unique to VARTM infusion because the non-rigid vacuum bagging can allow for small thickness changes (such as invisible bulging). If the vacuum bag is loose, as pressure inside the sample approaches atmospheric, the vacuum bag can loosely fill up with resin. If permeability was to increase after saturation, then the harmonic average permeability method for computing permeability would show a steady increase in actual permeability over the length of the sample. This may have been the cause of the 20% average increase from *R1* to *R3*, which were both non-curved regions.

Another factor that may have affected K_x may have been non-uniform compression due to fabric wrinkles. Curved regions for each test were observed to form small bridging wrinkles. These wrinkles would form as the sample was sucked tight under vacuum pressure prior to infusion. Vacuum bagging would push inward against the thickness of the sample and create vertical wrinkles in-line with the axis of curvature. When flow testing took place, some lateral flow was observed as the oil reached wrinkles.

This is the first known research to present this behavior in terms of the permeability of fabric with vertically-oriented local curvature. This is also the first to consider such effect of permeability due to VARTM behaviors. Results and noted flow behavior are valuable to aerospace industry members who wish to predictively model lateral flow across vertical panels and curvatures. Future opportunities for research include testing over other radii, examining the nature of fabric wrinkles, and incorporating bulging effects into permeability calculations.

4.7 Conclusion

Research evaluated the permeability of fabric with local curvature, such that flow was maintained at a constant elevation around a vertically-oriented curvature. This was done for four radii (1.6, 3.2, 6.4, and 25.4 mm). In agreement with previous research for other types of curvature, the research showed a decrease in permeability with decreased radii. Curved regions also experienced some vertical wrinkling or bridging when vacuum bagging compressed onto the fabric preforms. Experimentation hints at a different effect due to hydrostatic pressure than has been seen in previous literature called bulging. It is possible that in dynamic pressure environments, such as VARTM of lateral flow on a vertical wall having vertically-oriented curvature, fabric may thicken slightly, forming “invisible bulging” and increase permeability after fabric has saturated. This is valuable to aerospace industry members who wish to predictively model lateral flow across vertical panels and curvatures.

This research is the first to have considered curvature around a vertically oriented curve. Results showed a decrease in permeability of curved regions. The reduction in permeability can be justified by local fiber compression in curved regions, as compressed regions did not exceed

the theoretical v_F, but maximized just under the theoretical v_F. Other research has shown a reduction in local permeability that corresponds to an increasing. The reduction in permeability can be incorporated into simulation zones of fabric to better represent lateral flow of vertical profiles in VARTM. Such incorporation will allow for more predictive manufacturing of LCM parts.

5 PERMEABILITY OF LOCALLY SHEARED CARBON FIBER BEYOND SHEAR-LOCKING ANGLE

In the composites industry, significant efforts are being made to improve part quality and reduce part cost among high-performance parts (e.g. aerospace and automotive). Liquid composite molding (LCM) is regarded as an economically viable alternative to traditional methods. However, in order to achieve the high quality parts desired (and make LCM comparable to autoclave-prepreg processes), process optimization by way of infusion simulation must take place.

For the best simulation results, several parameters must be characterized. One such parameter is the effect of permeability on flow. The local permeability of various types and regions of fabric must be well-understood for accurate simulation. To understand how some advanced geometry applications affect permeability, much work has been conducted to characterize the in-plane permeability effects of sheared regions of fabric. Some work has been conducted on the through-thickness permeability of fabric layers bonded with thermoplastic binder material.

However, no work has been found which provides data on the permeability of fabric sheared beyond its shear-locking angle. This area of study is becoming ever more important as part designers push the limits of composite parts, using highly-packed fabrics with little drapability for complex part geometries (such as double curvature). Furthermore, in the study of

sheared permeability, no work has been done to simultaneously obtain the in-plane permeability and through-thickness permeability of a sheared region of fabric. The research at hand aims to evaluate permeability of fabric regions sheared beyond the shear-locking angle, and to adapt a method of obtaining the full permeability tensor to sheared fabrics.

5.1 Literature Review

For years, the permeability of sheared fabrics has been a topic of interest. Once a fabric type is characterized and permeability is understood for sheared states, predictive modelling and more accurate infusions are possible [77]. There is a vast amount of research on fabric permeability and sheared fabric permeability, because each fabric affects flow differently due to unique fiber geometry and surface chemistry. Each engineered fabric needs to be individually characterized [39,78], which is why a standardized method for measurement of sheared permeability would be beneficial to the flow simulation community. Such a standard has only been developed for non-sheared, 1D, in-plane permeability [7,8].

Models have been developed to predict sheared fabric permeability when the non-sheared fabric permeability was known [79-83]. The Carmen-Kozeny equation has been used to model the permeability of sheared fabrics [84]. This model is for unidirectional (UD) weave reinforcements, and shows that as fiber volume fraction (v_F) increases, permeability decreases. Experimentally validated models for non-UD weave fabrics have shown that shear can actually increase in-plane permeability, even as much as 230% [85-87]. Their data showed a local increase among in-plane permeability measurements among low-mid sheared angles. While other models have been developed, none shed light on highly-sheared fabrics. Researchers simply have said that they do not explore permeability of fabrics beyond the shear-locking angle

because of fabric deformations, noting that shearing beyond the shear-locking angle can cause a "significant increase in [in-plane] permeability" [84].

When fabric is sheared beyond the shear-locking angle, fibers wave in and out of plane to accommodate a decrease in area. Such wrinkling causes an extensive spring-back among fabric. Spring-back is defined as when an amount of elastic deformation is applied to a fabric, such that after deformation, the fabric tends to return somewhat to its un-deformed shape. Spring-back is normal for fabrics sheared both under and over the fiber-locking angle. However, when a fabric is sheared beyond the fiber-locking angle, spring back is extensive. And it becomes challenging to maintain shear while transporting fabric into infusion tooling. This is one reason why little or no permeability data is collected on samples sheared beyond their shear-locking angle. Another reason is that mechanical properties of composites have been shown to reduce with shear wrinkling [84], causing most manufacturers to avoid designing a process that incurs shear above the lock angle, thus making such permeability measurements less relevant to industry. However, industry has also shown interest in pushing the shear limits of highly packed (high fiber volume fraction) reinforcements.

To incorporate homogeneous shear throughout a reinforcement, a picture-frame or trellis tool is often used [87-92]. Such a tool however would be difficult to incorporate in the usual permeability measurement methods which involve the tight closure of a molding cavity around the reinforcement sample. Removal from the tool is usually followed by spring back of the reinforcement. For highly stiff materials, then spring back can be especially high, causing the reinforcement to return nearly to the un-sheared state. No method has yet been presented in the literature to hold sheared fabrics in place and prevent spring-back after removal from such a tool. In order to do so, a thermoplastic binder would need to be pre-melted into the fabric, or a unique

tool would need to be developed to hold the highly sheared fabric in place throughout subsequent permeability testing.

Some work was found on the effects of binder on fabric permeability. A recent research group, studying the effects of binders (on un-sheared fabric) noted that through-thickness permeability improved or increased [93] for compression resin transfer molding (CRTM) testing. This increase was due to micro-sized undulations created by binder particles the fabric. These undulations increased through-thickness permeability the most when mid-sized (not large, not small) binder particles were used.

While in-plane permeability [84,94,95] has been examined for sheared fabrics, little or no information was found on the through-thickness permeability of sheared fabric. Furthermore, no method has been found which obtains the full permeability tensor (in-plane and through-thickness permeability values) of a sheared fabric in one experiment, though such a method was alluded to in [30]. Establishing a means of characterizing the full permeability tensor in one experiment would help to establish a permeability measurement standard for sheared fabric.

There are three important areas to research concerning characterization of the permeability of sheared reinforcements. First, permeability measurements have not been obtained for a reinforcement sheared beyond the shear locking angle. Second, a method has not been developed to hold fibers in place for sheared fabric permeability measurements after removal from the shear-inducing tool. Third, a method has not been developed for obtaining the full permeability tensor in one test. This needs to be applied to sheared fabrics to facilitate standardization. The research at hand meets these opportunities by studying the effects of in-plane shear on the full permeability tensor of highly packed UD weave carbon fiber.

5.2 Method

5.2.1 Sample Preparation

Working in conjunction with an aerospace sponsor, a highly-packed carbon fiber reinforcement was chosen for evaluation of permeability under shear. The fabric was a UD weave fabric, Vectorply C-L 0900, with an aerial weight of 292 g/m^2 [76]. Each sample was cut to be square with edges 250 mm in length. Samples were trimmed such that there were four "wings (25 x 150 mm)" along each of the four edges, with an internal square of 150 x 150 mm. Layers were then stacked into sample laminates of eight plies each, with all layers aligned in the same direction $[0]_8$. It was found that the fabric was too stiff to shear at any other layup pattern. A trellis, or "picture frame" tool was used to shear the reinforcement samples. This tool introduced a reduction in fabric surface area, but applied uniform shear across the entire surface area.

To mitigate for spring-back, a thermoplastic binder was used. Four 150 mm x 25 mm strips of Pellon Wonder-Web strips were placed in between consecutive plies along the outer perimeter edges of the sample. Because there are eight layers of fabric (with seven interfaces), 28 total strips of binder were used. The sample was sheared in the trellis tool, locked in place with a steel bolt, and placed into an oven to melt the binder. The central region of the sheared laminate sample (where infusion measurements were to take place) was left untouched by the binder. The sample was then cooled outside of the oven to ambient temperature to re-solidify the binder and then the sample was removed from the trellis tool. Samples were sheared to 20° and 40° and locked with binder in this way. It should be noted that the shearing of the fabric introduced out-of-plane undulations in the eight layers of fabric, which would later be pressed flat by the rigid tooling. When the sheared fabric was pressed flat, the undulations visibly flattened, with tows

expanding laterally in some places to still allow for compression in the fiber. These compressed undulations are addressed later in the discussion.

5.2.2 Tooling and Experimentation

The trellis tool used for this research is pictured in Figure 5-1. It pressed on the outer edges of the sample, and used a number of sharpened screws to lock the fiber in place. While the thermoplastic binder was setting into the fabric, a steel diamond shaped plate was used to control the shear angle. The fabric sample was cooled, removed from the trellis tool, and the wings were cut off to leave a sheared trapezoidal shape with 150 mm sides, as shown by the red dotted lines in Figure 5-1. Acute corners were also trimmed ~25 mm (shown in Figure 5-1 with blue dotted lines) to fit the sample into the permeability testing equipment. Care was taken to transport the sample into the permeability testing equipment in a way that did change fabric architecture.

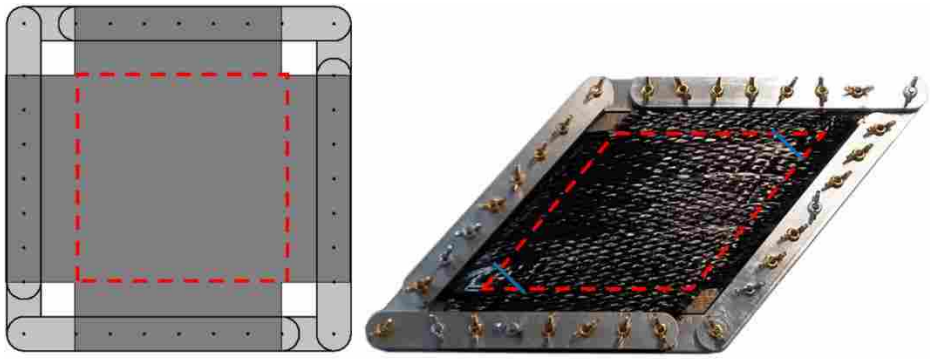

Figure5-1: Trellis tool, un-sheared (left) and sheared to 40° (right)

For 3D testing, a two-sided acrylic tool was used. This tool was used in previous work by George et al. [96], and is shown in Figure 5-2. Tool sides were 74 mm thick after polishing. The tool had a central inlet (a) and corner outlet to vacuum (b) on the top mold-half. The inner

surface of the acrylic tooling was polished to planarity tolerance of 0.2 mm. To maintain the desired cavity thickness between the two mold-halves, gauge steel was used (c). The sample was thus pressed to a constant thickness despite prior out-of-plane deformations due to shear-induced undulations. Sealant tape (d) was used to maintain internal vacuum pressure. A small mirror (e) was placed underneath the tool to allow visibility of the through-thickness flow when it reaches the bottom tool surface. Eight bolts were patterned evenly around the perimeter of the tool (f).

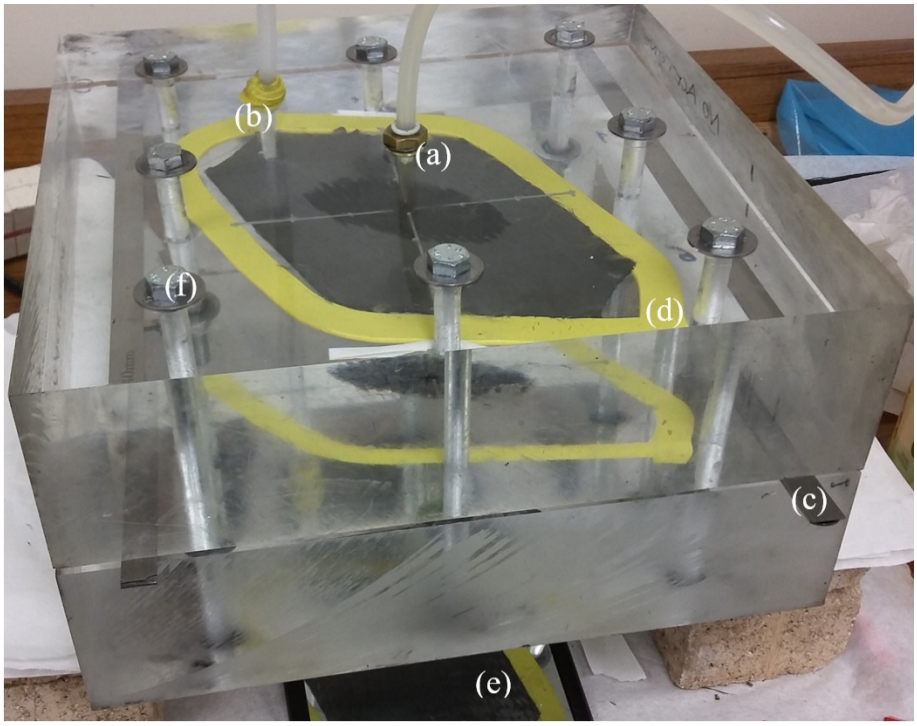

Figure 5-2: 3D Permeability tool with sample in place

After each sample was prepared, it was placed in the 3D tool and infused with canola oil. The infusion parameters are as follows. Ambient temperature (T) was typically 22°C. Viscosity [$\mu(T)$], was typically 0.056 Pa·s. Thickness was set at 2.4 mm with gauge steel. Inlet ambient pressure was recorded to be typically 86 kPa (due to altitude), and vacuum pressure was on the order of 1.0 kPa. After flow parameters were recorded, infusion began.

The flow began at a point in the top of the sample just below the inlet tube, and then spread as a semi-ellipsoid formed through the reinforcement. The bottom half of the mold was visually monitored with the assistance of them mirror to help researchers know the moment when fluid had penetrated the thickness of the sample. At that moment, the flow profile was photographed for permeability measurement.

5.2.3 Permeability Measurement

After testing, the permeability was measured to determine in-plane permeability and through-thickness permeability [96]. There has historically been a substantial amount of error in comparable permeability measurements, with 25% data spread being common for 1D characterization in the same lab with the same method [7,8], even higher spread can be seen with 3D characterization. Thus, to mitigate error as much as possible, the tool face was modified so as to show cross hairs on the fabric. These can be seen in Figure 5-3. As soon as the test fluid

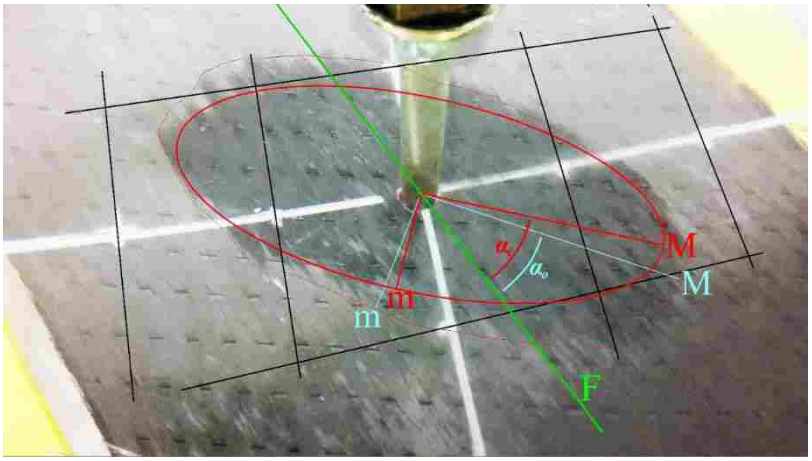

Figure 5-3: Digital measurement of the flow front ellipse major (*M*) and minor (*m*) axes with angles to flow orientations. Red lines represent axes to the fully saturated bulk flow front. Light blue lines represent axes to the unsaturated flow front.

visibly touched the bottom tool, indicating wetting through the entire sample thickness, a photograph was made through the top mold-half of the top surface of the sample.

This photograph was then post-processed to determine more accurately the dimensions of the formed ellipsoid to help with flow analysis. From this information, the in-plane permeability and flow orientation were determined. Figure 5-3 shows an example photograph of the top surface at the end of an experiment. A grid was digitally overlaid to assist with ellipsoid measurement of major (M) and minor (m) axes. In red are the M and m measurements of the fully-saturated region, i.e. the trailing flow front or "bulk" flow front. In light blue are the M and m measurements of the farthest reach of the oil, i.e. the leading edge of the flow front. The orientations of ellipses were marked by α_i and α_o to denote the angles between the fiber line (green F) and the major axes of the inner (red M), fully saturated ellipse and the outer partially saturated ellipse (light blue M).

The difference between the inner and outer ellipses is caused by the dual-scale nature of the flow in a typical composite reinforcement [97], where the flowrate between the tows (yarns) is driven by the applied pressure gradient. The flowrate inside the tow (between individual filaments) is driven by capillary forces. To better understand the effects of this dual scale flow, the permeability was evaluated using both the bulk flow and the leading edge flow front dimensions.

After M and n were recorded, the 3D permeability (K) tensor was evaluated using a formula for K developed by Mekic et al., because it is the only method which accounts for the true circular shape of the initial flow front at the circular tube inlet [6]. More information for K is provided in the Appendix. It should be noted that K can be broken into its orthogonal components, K_X, K_Y, and K_Z. The other solutions in the literature for such elliptical flow have to

assume an elliptical inlet shape, which imparts an error in the permeability calculations. This error is greater when the sample thickness is low [6,53,98]. As the through thickness permeability (K_Z) for this UD-weave is relatively low compared to other reinforcements, the sample thickness was correspondingly low, thus implying the need for the inlet-shape corrected solution. The only weakness of the Mekic solution is that the in-plane permeability separate components, K_X, and K_Y, cannot be calculated. The equivalent isotropic in-plane permeability (K_{XYE}) can be calculated, which is the square root of the product between K_X and K_Y. K_{XYE} is often referred to as the normalized in-plane permeability. The orientation of the flow ellipsoid (α) was also measured. The angle, α, is the rotation angle between the major axis of the ellipse and the warp machine direction of the reinforcement.

5.3 Results

Results of shear beyond the shear-locking angle are provided. These include the effects of in-plane shear on the full permeability tensor. Permeability anisotropy and flow orientation are also presented with respect to shear angle. A discussion is provided thereafter to evaluate results.

5.3.1 Permeability

The in-plane permeability K_{XYE} results are plotted in Figure 5-4. Because K_{ZZ} values are significantly smaller than K_{XYE}, K_Z results are plotted separately in Figure 5-5. Error bars indicate the standard deviation. The un-sheared results shown are from previous testing using the same tooling except that no binder was applied, nor was the trellis tool employed on these samples. The leading edge measurement method resulted in a 32 to 46% increase in K_{XYE} compared to the bulk flow measurement method. The same increase was 15 to 16% for K_Z. The error bars overlap the difference between these two methods, suggesting that it is not a statistically significant

difference for this sample set. Filling simulation usually assumes complete saturation, thus permeability values in the remainder of this paper will refer to those of the bulk flow region. Note from Figure 5-4 that samples sheared to 20° and 40° still showed spring-back of 3 to 4° after binder application, resulting in the recorded shear angles.

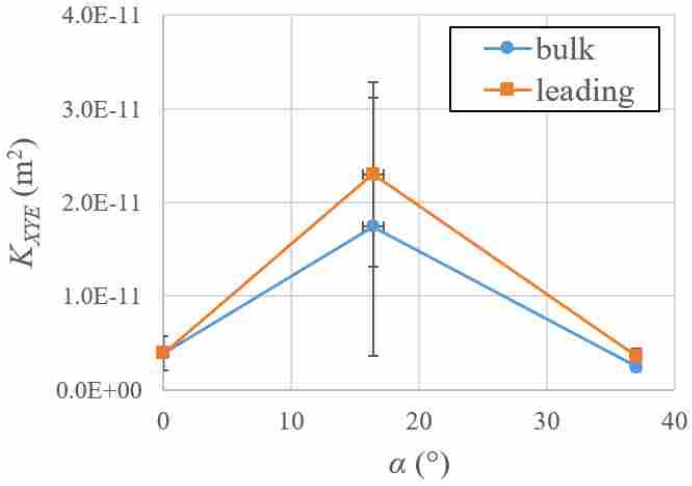

Figure 5-4: In-plane permeability of sheared samples of [0]$_8$ VectorPly C-L 0900

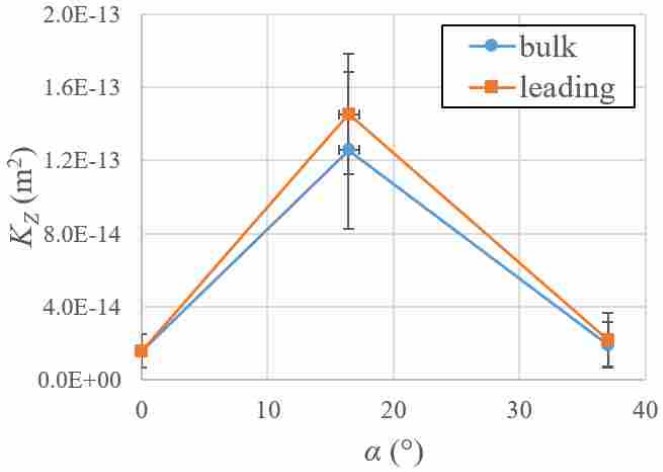

Figure 5-5: Through-thickness permeability of sheared samples of [0]$_8$ VectorPly C-L 0900

For the data set in both Figure 5-4 and Figure 5-5, a shear angle of ~16° shows the highest permeability for both in-plane and through-thickness directions. This shows that as fabric was sheared, permeability increased. As shear increased further to ~37°, permeability values restored to the un-sheared permeability results, evident for both K_{XYE} and K_z.

A summary of permeability data from different methods is presented in Figure 5-6. In this figure the individual test results are presented, rather than the averages, for a comparison of the scatter. The maximum difference between measured permeabilities was roughly half an order of magnitude difference between K_Z measurements found at the high shear angle (37°). While a curve is shown to highlight trends, there was not sufficient data to conclude whether a best fit is in fact a parabola. Rather, for data obtained, permeability was highest among fabric sheared to around 16°, including through-thickness permeability (green). The lowest permeabilities in general were found at high shear angles.

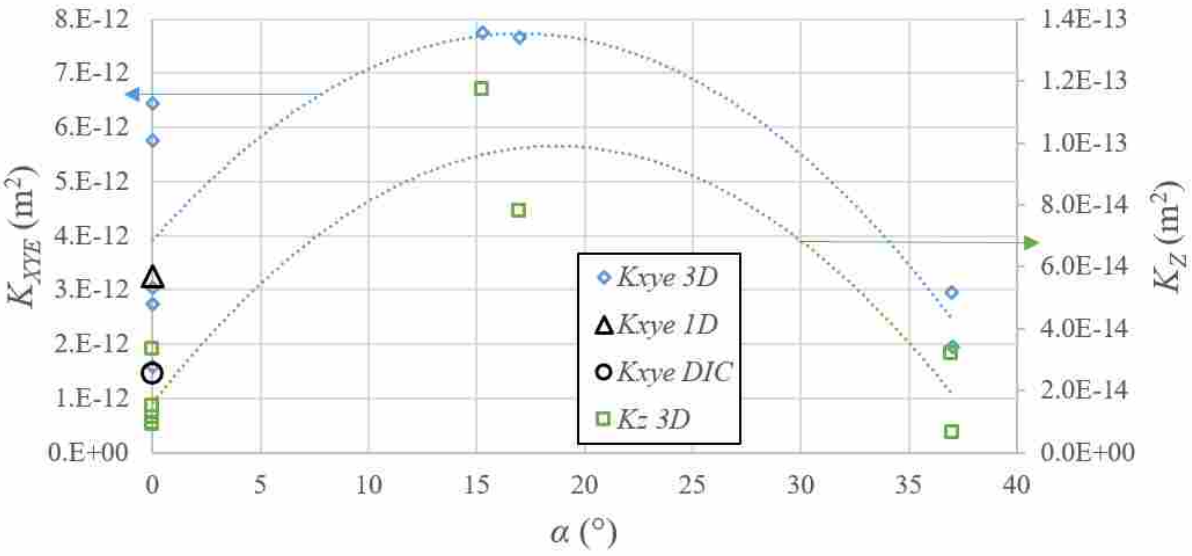

Figure 5-6: Summary of permeability for UD carbon testing

For comparison, the results for the same reinforcement (un-sheared) by two other in-plane permeability measurement methods are also presented in Figure 5-6. Data labeled K_{XYE} *1D* comes from a 1D flow measurement using a rigid tool as outlined in the permeability benchmark [21]. Data labeled K_{XYE} *DIC* is from a 1D flow test under a vacuum bag employing digital image correlation (DIC) to determine the permeability [99]. These other in-plane measurement methods showed a lower in-plane permeability than what was measured in the 3D radial tool. The 1D rigid tool measurements resulted in approximately half of the 3D measured in-plane permeability, while the DIC measurement method resulted in 24% of it. This may imply some difference between the tooling methods, or an experimental error associated with one of the measurement methods. Even larger differences in permeability have been measured across different methods for even 1D flow in the first worldwide benchmark [7].

5.3.2 Anisotropy

A summary of orientations for the fully saturated ellipse shown in Figure 2-6. Shear angles are shown, indicating the measured angle of the sheared sample after the sample was prepared. The ratio, *M/m* gives insight as to the anisotropy of the in-plane flow ellipse (where unity would indicate a circular ellipse flow front). The ratio serves as an estimate of $(K_X/K_Y)^{1/2}$. The anisotropy M/m shows the opposite trend from the permeability in Figures 5-4 and 5-5; a decrease is seen (showing closer to isotropic flow behavior) for the mid-range shear measurements, with higher anisotropy seen in the un-sheared samples, and the highest anisotropy in the high-sheared samples.

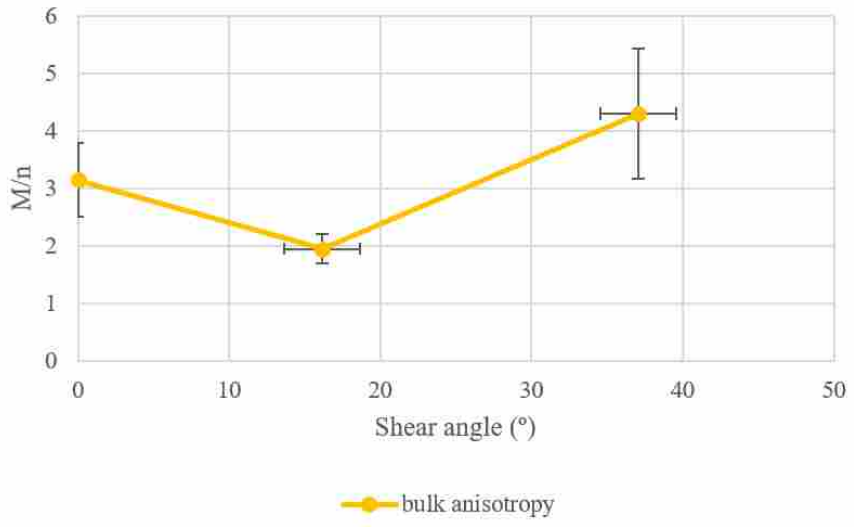

Figure 5-7: Summary of shear-induced anisotropy

5.3.3 Ellipse Orientation

Figure 5-7 compares the orientation angle α for both bulk and leading flow fronts. All samples demonstrated flow dominated by a tendency of resin flow to maximize within the acute angle, approximately 45°, i.e. between weft and warp reinforcement directions. At low shear angles, flow tended to align with the reinforcement fibers. For mid-range shear angles of ~16°, the leading flow tended toward the weft fiber direction. The outer flow front showed higher angles for the mid-range shear angle, but the ellipse was difficult to define for the "fingered" flow at these short flow radii. Thus the high shear angles may be caused simply by the capillary vs bulk flow differences (Figure 5-8). Meanwhile for mid-range shear angles the bulk flow front rotated nearly linearly with shear angle. At high shear angles of ~37°, the leading flow front aligned again with the bulk flow front.

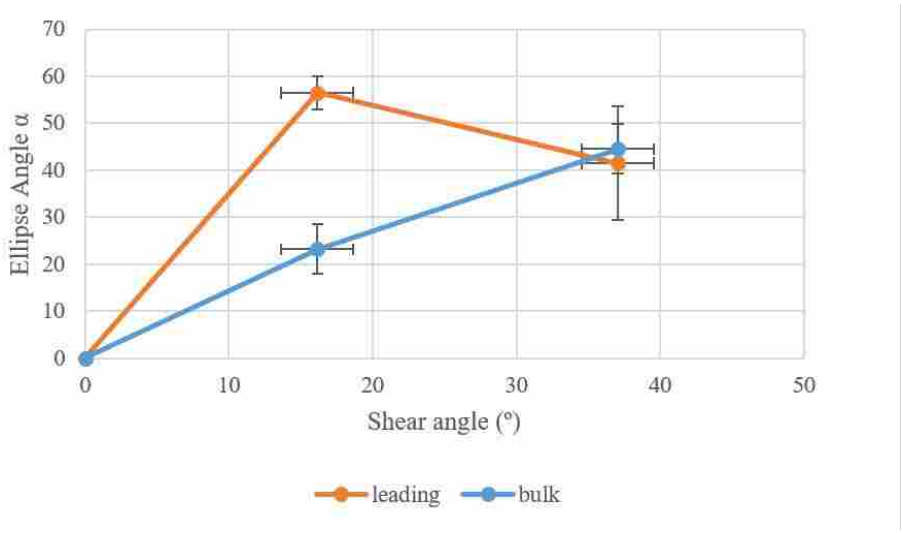

Figure 5-8: Bulk and leading ellipse rotation angles

5.4 Discussion

The UD weave reinforcement used in this research was expected to show a decrease in permeability with increasing fabric shear, as the gaps between the fibers were expected to reduce with shear. Such was predicted by the Carmen-Kozeny model in a previous paper [11]. However, the results demonstrated a very different flow behavior. K_{XYE} and K_Z values increased for mid-range shear (all beyond the shear-locking angle, ~5°), and decreased for the highest shears. Thus, the Carmen-Kozeny model for UD weaves in the previous study did not represent behavior seen here, as well as in other research [86]. As shear beyond the locking angle may incur out-of-plane deformation (though the overall thickness of the preform remains fixed because of rigid tooling), the increase in permeability (in all directions) may be caused by an increase in porosity associated with the post-lock-angle shear. The permeability data shown in this paper may serve as the foundation for developing such a model.

An important result of this research was the generation of data beyond the shear locking angle. After shearing to about 5°, visible shear wrinkles formed. Such a low locking angle confirms the high stiffness of this reinforcement. The shear wrinkles were out-of-plane deformations that increased the thickness of the sample during sheared sample preparation. The sample thickness was then reduced to less than the un-sheared state by the 3D permeability tool. It was during this "flattening" that micro undulations could not simply straighten out. They were forced to fall to one side (residing sinusoidally in the flat fabric plane), or were perhaps compressed into tighter out-of-plane undulations. Though the overall preform sample was constrained to 2.4 mm (eight layers at 0.3 mm each), vertical undulations of layers may have pressed into adjacent layers. This likely produced micro buckling.

These shear-induced wrinkles may have created in-plane flow channels, perhaps due to a grid of locally high and low compression regions, i.e. tight buckle-bends or local micro-wrinkles. This allowed for faster in-plane flow despite a decrease in overall porosity with shear at mid-range shear angles. High shear angles (~37°) involved such high compression (even higher v_F) that both in-plane and through-thickness permeabilities reduced. By shearing fabric even farther beyond the locking angle, to ~37°, both the in-plane and through-thickness permeabilities decreased. This suggests that the channels introduced by undulations were compressed and closed off at the higher shear angles.

While increased permeability may be desirable for faster flow, increased fabric undulations can lead to a significant reduction in mechanical properties. This is because undulating fibers are essentially buckled fibers. The overall composite tensile and compressive stiffness would then diminish accordingly. If tow micro undulations were compressed so far as to become kinks, then the effective fiber length would also diminish. This could cause problems in

terms of fiber pull-out and load distribution. Further work to assess the mechanical properties of fabric sheared beyond the shear-locking angle for this fabric would need to be conducted in order to adequately address the tradeoff between significantly higher permeability and lower mechanical properties for high shear.

Not only were overall permeability and mechanical properties affected by shear, but the orientation of flow ellipses changed with shear. As the shear angle increased, lateral flow channels shifted due to weft yarn translation, i.e. rotated with shear and slid between the tows. This sliding of the weft yarns with shear were the primary cause of the rotation of the major axis of flow, because weft yarns form relatively large flow channels with this fabric.

The major and minor dimensions of flow were also affected by shear. This observation can be drawn from comparing the values of *M/m*, shown previously in Figure 5-7. A *M/m* ratio close to unity would represent a circular in-plane flow ellipse. A high ratio would represent a long ellipse, indicating greater in-plane flow anisotropy. For mid-range sheared samples, overall anisotropy decreased; *M/m* was at a minimum, and K_Z was at its highest. This means that with mid-range shear values, the disorder in fiber orientation was maximized, and flow was slightly more isotropic.

While binder was placed only on the perimeter of samples to prevent spring back, there is reason to believe it may have altered K_Z. Binder may have been able to distort the geometry of the central region of the samples beyond simply holding fabric in a sheared state through promotion of undulations around the sample perimeter. Undulations in fabric are a major cause of increased flow both in-plane and in the through-thickness directions.

Future work for the research at hand would be to obtain more data points to fill in the permeability vs. fabric shear curves (Figures 5-4 through 5-6). This would facilitate the comparison to similar curves of fabric which has been sheared below the shear-locking angle [86]. Another opportunity for future work is creation of a micromechanical model of the fabric to analyze the theory of micro-buckling. The validate the model, micrographs of the dry sheared textile could be taken before tool closure (and perhaps within the tool). This would help researchers to identify in-plane and through-thickness flow channels created by the undulations. Buckling behavior could also be mathematically and experimentally characterized. Yet another opportunity for future work would be to include a comparison of the benefits of increased permeability for tightly-packed fabrics vs. reduction in mechanical properties due to shear.

5.5 Conclusion

A new application of the 3D permeability characterization is presented for measuring the sheared fabric permeability by estimating the three-dimensional permeability in one test. This is the first research seen to provide permeability data for fabric sheared beyond the shear-locking angle. The method shows promise in producing results compatible with previous research's suggestions about the effects of shear wrinkling increased permeability. Permeability increases with fabric wrinkling. This was true for fabric tested with rigid tooling (i.e. undulations remained within the controlled preform thickness). This was contrary to the Carmen-Kozeny model which suggested that permeability would decrease with increased v_F. As shear (beyond the shear-locking angle of ~5°) increased to mid-range shear, permeability increased. Permeability decreased as shear angles reached highest values, likely due to fabric compression and fiber nesting.

In order to research in-plane shear beyond the shear-locking angle, a method was developed to hold fibers in place for sheared fabric permeability measurements. This method involved a trellis tool, binder, trimming fabric, and transporting the fabric to a rigid 3D permeability tooling.

To most accurately capture the flow shape during experimentation, a digital photography analysis method of measuring the flow front ellipsoid was used. Multiple techniques of in-plane permeability measurements with respect to shear were compared to help with LCM optimization. The effect of binder on the fabric permeability was discussed.

6 FLUORESCENT VOID FLOW MONITORING OF CARBON COMPOSITES

6.1 Abstract

Liquid composite molding (LCM) is growing in importance as an alternative to traditional prepreg-autoclave methods for manufacture high-performance composites. The most significant roadblock to industry's implementation of LCM is its higher void content. One tool for reducing void levels involves optimization of flow, which requires models to be developed to describe *in situ* void behavior. To help solve this problem, the following research generates the first known method for optical void flow monitoring for carbon fiber *in situ*. The work utilizes fluorescent dye and a digital camera to produce sufficient contrast and resolution for good image analysis. Visible void content is tracked against the opaque carbon fiber background. 230 images for three different orientations of a single fabric are used to produce the highest amount of *in situ* data seen so far on void content vs. flow velocity during resin infusion. Void content vs. resin flow velocity is investigated for a unidirectional weave carbon fiber with velocities ranging from about 1e-3 to 1e-5 m/s. This data verifies previous work and identifies a velocity threshold for minimal macro-void content. Data also indicates that flow along the fiber orientation is most sensitive to macro-void formation. An automated method of image analysis is presented to enable tracking of high volumes of void data from the high-contrast *in situ* images. The resultant void tracking framework will enable modeling and experimental validation of void flow *in situ* for LCM of carbon fiber composites.

6.2 Introduction

The composites industry is seeing growing demand, particularly for low cost, high volume production of carbon fiber parts with desirable mechanical properties for aerospace and automotive applications [100]. For example, the Boeing 787 line is now composed of 50% composites (by weight), and the carbon fiber composites industry has grown at a steady 10% per year for over six years [101]. For decades, aircraft composites have been made using autoclave-prepreg manufacturing methods. Those methods, however, limit production rate and involve high material and processing costs. Less expensive, more versatile methods for manufacture are sought to keep up with economic demand. Liquid composite molding (LCM) methods, including resin transfer molding (RTM) and vacuum infusion (VI), are seen as potential viable alternatives to prepreg-autoclave because of their low costs, if resultant composite quality can be increased.

The primary differences between parts produced via LCM and prepreg-autoclave manufacturing methods are part homogeneity and void content. Void content, or bubble content (v_B), is a measure of the amount of gas that is trapped within a finished composite part. Void content significantly affects the mechanical properties of a composite, with high v_B leading to lower tensile-, flexural-, interlaminar-, and shear strength [102,103]. Typically, macro-voids, or the larger voids located between composite tows or yarns lead to a greater reduction in mechanical properties than the smaller micro-voids, which are located within tows.

Voids form in a composite during infusion and cure. For LCM methods, as resin enters the fiber lattice, small amounts of gas are mechanically entrapped as bubbles [104]. This gas comes from either the resin itself, or from lingering atmospheric gas amid the fiber / fabric (even if it has been held under vacuum pressure for some time). As the infusion continues, the bubbles often remain trapped where they were formed, and sometimes move through the reinforcement

toward lower pressure at the flow front [105]. Voids can also grow from bubble compounding or shrink from bubble division or diffusion into the resin [106]. Pressure changes, fabric architecture, and tooling surfaces can affect void size, shape, and flow [107]. Void behavior is affected by capillary forces (which lead to multiphase flow [108,109]), and by a bubble's tendency to form spheroids and cylindroids for lower surface energy. When the part cures, resin motion slows and stops. Any bubbles remain trapped in the polymer matrix as voids.

Inter-tow macro-voids are formed when the flow front velocity is low and the intra-tow capillary flow outpaces the inter-tow bulk flow. Intra-tow micro-voids are formed in the opposite case when the flow front velocity is high and outpaces capillary flow [110,111]. Predictive models have been developed to optimize manufacturing – usually showing void formation as a function of flow front velocity and identifying a target velocity threshold for minimum v_B [105,112,113]. To validate such models, some experimental work has been conducted. However, the most thorough experimental work to validate such models, has been limited to a few data points, and only in fiber glass reinforcements [110,114-116].

More data would help to validate the models defined for optimization of void content during the infusion process. Particularly, this data is needed for carbon fiber, since it is carbon fiber LCM which manufacturers are seeking to optimize for high performance applications due to its higher mechanical performance compared to fiberglass. The local void content has previously been characterized in carbon reinforcements by electrical conductivity measurements [117] and via ultrasound [118], but these studies give no information on individual bubbles. Thus process optimization would benefit greatly from a methodology to acquire high-resolution, high-contrast images of *in situ* bubbles during infusion of carbon reinforcements.

The need for high-resolution, high-contrast *in situ* images would better allow for automation of void content through automated digital analysis. With higher quality images, more accurate digital tracking of voids and automatically analyzing hundreds of images would be possible. With so much data, stochastic characterization could be performed to address the micro-variation found typically in composite reinforcements [119]. Researchers would no longer need to color in void pixels of each individual micrograph, a process that can take several minutes to hours for each image.

This study addresses the need for in-situ data of void evolution during LCM of carbon composites, and makes several contributions to the field of LCM flow and void monitoring:

1. A framework for in-situ bubble tracking in carbon fiber LCM is created. Camera, dye, and lighting parameters are presented for optimal bubble contrast.
2. An automated methodology is developed for filtering images, to isolate visible bubbles and report statistics on those bubbles. This method is calibrated against manual measurements of bubble content. High volumes of bubble evolution data can now be generated for the first time.
3. The framework is validated across 0º, 45º, and 90º fiber orientations in 1D infusion testing. Tests are performed using atmospheric to vacuum pressure, which produces a range of flow velocities. Visible void content was measured and plotted against flow velocity, showing results that generally conform currently accepted trends.

6.3 Literature Review

A major drawback to LCM processes is that they produce higher void content (typically ~2% for RTM and ~2.5% for VARTM) than traditional prepreg-autoclave methods (~1%) due to

bubble entrapment during infusion [110,114,115]. If void flow and formation can be mitigated or at least controlled such that voids are concentrated in less structurally critical regions of a composite, then LCM processes may serve as a low cost alternative. In light of this, characterizing void formation and mobility during infusion of composites continues to grow in importance [105,107,111,120-122]. Researchers seek to narrow the gap in mechanical properties between LCM and prepreg-autoclave processes through optimized processing. Efforts to begin this transition were conducted in 1993 by Lundstrom [123]. This work identified that high bubble or void content formed at the flow front of resin as it infused parts. Though, at the time, virtually no prior investigations had taken place to explain the mechanisms behind such flow.

Voids are spaces of non-matrix, non-reinforcement material that are developed or trapped in a composite during molding and that reside after cure. Voids can be in the form of evaporated moisture trapped in the part, or gas residing in the resin or mold during infusion. In literature, there is some overlap of the terms void, dry spot, and bubble. Voids and bubbles are used synonymously. Large voids or void clusters are both referred to as dry spots. Void content is defined as the volumetric percentage of voids residing within the composite material volume.

High void content greatly reduces the mechanical properties of composite material parts. Research has established that increased void content leads to a widespread reduction of key mechanical properties of composites [124,125] with matrix dominated properties being most affected [102,111,126] – especially in cases of fatigue loading [127]. Numerous studies have examined the effects of void content on properties such as surface finish [128], damage in large structures like wind blades [129], and failure mechanisms [130]. The mechanical properties of composites reduce substantially with rising void content [102,131].

Researchers have sought to find ways to reduce the void content in LCM processes by characterizing void formation *in situ*. For example, the relationship between flow front velocity and void formation rates for infusion processes has been proposed and studied [132]. Benefits of such modeling include process optimization for minimal void formation as well as anticipating where dry spots are likely to form based on RTM inlets, outlets, fiber layup, flow characteristics, and geometry [112,133]. Park et al. point out the need for more research in characterizing macro-pore (or macro-void) formation [111].

In order to characterize void behavior with carbon composites, researchers have commonly utilized microscopy to validate methods *ex-situ*, or after processing [104,134]. Microscopy can only give insights after the bubbles have moved and been entrapped, giving little information on bubble formation and migration.

Non-optical *in situ* methods for void characterization in carbon reinforcements include flowrate comparison [135], pressure sensors [136], electrical conductivity [117], thermal conductivity [137,138], x-ray scanning [139,140], ultrasound [141], dye penetration inspection (DPI) [142], and embedded electronics [39,133]. Only one of the x-ray sources [139] was found to show bubble mobility clearly enough to describe void transport in situ. However, the entire data set involved flow through a single tow of fiberglass. Experimental void behavior was described and compared to models, but no presentation of void content vs. flowrate was given. There is a need for much more experimental data for in situ void flow across the composites processing cannon.

As was briefly mentioned, previous research has utilized another means for monitoring void flow *in situ* called dye penetration inspection (DPI) [142]. This method involved mixing 0.1 g/L of fluorescent tracer into 99% pure hexadecane (cetane) and tracking flow through a

bidirectional E glass preform. The purpose of the research was to monitor wicking capillary flow within tows. The method estimated micro-void content (i.e. voids within tows) and macro void content from fiber saturation. While no "optical" images of voids were obtained, the method was useful in calculating void content for the hexadecane-E glass system.

In the literature, a variety of fluids have been used when conducting composite processing flow experimentation, such as water [115] syrup-water mixtures [139], silicone oil [114], dioctyl phthalate (DOP) [114,135], canola oil [143], and resin itself [114,117,140]. The goal is generally to use liquids which have similar viscosity and surface tension to typical epoxies used in LCM, but which do not cure, enabling re-use of the tooling. Each choice of fluid has some advantage (such as cost or transparency), but with other disadvantages. For example, hexadecane is a low viscosity fluid (~3.5 mPa·s) [142]. Viscosities of typical high-performance resins for infusion are on the order of 50 mPa·s during infusion [9,144]. Interactions with unique resin-tooling surfaces and resin-fiber sizing (chemistry) combinations also introduce variety.

Glass reinforcements are translucent, allowing for accurate optical *in situ* experimentation. Void behavior with fiberglass can be easily back-lighted and photographed to gain insights into bubble kinetics. Even still, very little data has been found to show *in situ* void behavior for fiber glass. Furthermore, glass fabrics differ enough in fiber diameter, sizing (and resultant surface chemistry) and packing from carbon fiber fabrics to suggest that glass void and flow characterization may not be valid for that of carbon fiber.

Monitoring void flow in carbon fiber is challenging because of the limited visibility of voids against the opaque (black) carbon fiber background. Until now, no previous research has provided *in situ* data for void flow of carbon fiber. Yet *in situ* experimental data is critical to validate existing composite processing models for void flow in carbon fiber. Data is needed in

the areas of measuring void content as a function of flow velocity for dual scale flow (as existing literature only has a few fiber glass data points for this kind of model [111,115,132,142,145], capturing and measuring images of bubble migration, size, and shape [107,111,113,120,122,146], as well as more data on void content as a function of distance from the inlet [110,114,115]. This kind of *in situ* data for carbon fiber will substantiate models and provide bubble flow insights which may benefit LCM processing optimization.

6.4 Method

6.4.1 Overview

The developed method uses fluorescent dye and UV lighting to track macro bubble evolution in carbon fiber LCM. The camera, dye, and lighting parameters by which images were obtained are described. A digital method of filtering images to isolate visible void content is created, and captured in a flowchart. Three different lay-ups of a UD weave carbon fiber were monitored in a typical 1D-type flow test, giving insight on the void kinetics of different fiber orientations. Samples were infused with a canola oil and UV dye mixture; the choice of canola oil fluid is discussed in the materials section below. The infusion took place in a dark room with a UV light over the sample, illuminating the dye and adding contrast to voids. Resultant digital images were processed using two computer scripts. The first determined good threshold and image filter settings for a data set with a representative image selected from the full image set; the second applied the image settings to a set of images, collecting data on each image such as visible void content, flow front location, and void orientation.

6.4.2 Tooling

The tool used for bubble observation resembles other 1D flow tools as described in a recent permeability benchmark exercise [8]. The purpose behind using similar tooling was to allow the method to easily disseminate to other labs with existing 1D infusion equipment. Tooling is primarily comprised of a lower plate made of 12.7 mm thick steel and an upper plate made of 76.2 mm polished acrylic. Planar tolerances on the steel and acrylic are 0.025 mm and 0.02 mm, respectively. Acrylic was selected due to its high transparency, low cost, and sized to provide an equivalent effective stiffness to the steel. The two plates were bolted together using a long steel C-channel on each of the two sides of the tool, to distribute the compressive force along the acrylic plate [99]. Surface chemistry and wetting properties of the acrylic, when compared with carbon fabric, was not considered. Since the fluid-acrylic interface is where void images are captured, the effect of the acrylic surface properties should be studied in future work. For the current test campaign, the acrylic was soap-washed of oil in between tests. For future tests, it is also recommended that a thin, transparent membrane with known surface chemistry be placed between the sample and acrylic to correctly determine surface interactions in bubble behavior.

An RTV silicone bead was traced around the perimeter of the test area and allowed to cure with calibration shims to ensure a pressure seal of uniform thickness. The seal bead was set to a height of ≈ 0.2 mm above each sample's uncompressed thickness so that compression would close the seal. After curing, the seal was trimmed with a razor to match the fabric sample width.

6.4.3 Materials

A carbon UD weave, VectorPly C-L 0900 (292 gsm) was used as the reinforcement. Samples were made from three different fiber lay-ups: $[0]_5$, $[45,-45,(45)\overline{]}s$, and $[90]_5$. For simplicity, these will be referred to as 0°, 45°, and 90° samples, respectively.

All tests were performed with canola oil due to its similar viscosity (57 mPa·s) at ambient temperature), surface tension (0.033 N/m), and chemical structure to many thermoset infusion resins at infusion temperature. For example, RTM-6 typically involves a viscosity of 59 mPa·s after 2 hrs at infusion temperature of 120 ºC [9,10,144]. Canola oil was also chosen because of the inexpensive cost, lower skin irritation, and ease of clean up. While there is no perfect substitute for infusion resin, the oil/dye mixture for this research was regarded to fit the scope of research objectives.

To enhance the contrast during visual examination of the infusion process in the opaque fibers, an oil-based UV dye was mixed in the test fluid (Tracer Products Dye-Lite TP-3400-0601). The UV dye was mixed into the test fluid at approximately 5% of the total volume and was thoroughly mixed. A Brookfield DV-E viscometer was used to measure the viscosity of the mixed solution, which was 63 ± 1 mPa·s at room temperature in the temperature controlled laboratory. Addition of the tracer dye increased the viscosity of the canola oil, though its effects on surface tension were not investigated.

6.4.4 Camera

To photograph the infusion process and obtain consistent images of the void formation across the sample, a DSLR camera (Sony α77, with a SIGMA 50 mm 1:2.8 DG MACRO lens) was attached to a rail that was suspended above the experimental tool. The rail allowed the

camera to capture images across the entire sample with constant orientation to the flow front. Attached to the base of the camera was a nylon pulley system that could slide the camera along the rail as the infusion progressed. The camera was moved according to the location of the flow front. Photos were taken automatically with a timer. The camera was manually focused to show maximum fiber clarity *before* the lab lights were turned off. The camera was maintained at a height level to the sample so as to maintain focus during flow and camera motion. A 25 cm ruler was embedded in the seal of the flow below the acrylic window to act as a reference (partially shown in Figure 6-1) for image post-processing.

6.4.5 Lighting

In earlier studies [147], a commercial UV light was used for maximum contrast between voids and non-void features inside the mold. For this research, a United States standard 120 V 61 cm black light fixture and bulb were used. This provided uniform lighting across the sample. In an otherwise total dark room environment, this UV light was sufficient to create excellent contrast to capture void behavior.

6.4.6 Sample Preparation

Each sample of the reinforcement was cut to the dimensions of 50 x 250 mm and stacked on top of each other in the sample lay-up orientations listed above. The ply stack or preform was then placed onto of the steel plate and within the RTV seal such that there were no gaps between the fabric and the seal (to prevent fluid racetracking). 1.3 mm of gauge steel was placed on the steel plate outside of the seal and adjacent to bolts to ensure uniform sample thickness (at 1.3 mm, $v_F = 0.62$) after mold-closure and prevent any tooling deflection as the two plates were bolted together. The tool was clamped shut with six bolts which were torqued to 40 N-m. A 6

mm inner diameter tube connected the tool inlet to a pressurized air tank that contained a cup full of the UV-dyed canola oil solution. The oil cup was held below the infusion sample height to mitigate the effects of hydrostatic over-pressure. Vacuum was drawn through the sample using an outlet tube that was connected to a resin pot and subsequent vacuum pump drawing ~85 kPa (atmospheric at mountain elevation).

6.5 Automated Image Analysis

A typical approach to void identification involves thresholding the intensity of an image and classifying low intensity features as voids. However, automated recognition of voids in micrographs or optical images using the thresholding method is difficult. Difficulty comes from optical similarities between voids and fibers, surface defects, optical aberrations, and sometimes non-discrete boundaries between voids and fluid. But certain characteristics of bubbles can help distinguish them from other parts of an image. Distinguishing characteristics were found to be color, size, shape (aspect ratio of cluster), orientation, and the porosity of pixel clusters (not to be confused with fabric porosity). In this section we describe the software tools developed based on these characteristics to achieve accuracy with automated bubble identification.

6.5.1 Definition of Visible Void Fraction

Visible void fraction (v_B) is an aerial-view measure of bubble or void content, measured as the ratio of the bubble area to total sample area. Such areal analysis of void content is commonly reported, especially for two-dimensional micrographs of cured laminates [103,104,123,131,134,141,148,149]. This paper does not include a measurement of volumetric void content. In other studies, the assumption is made that area fraction is reflective of volume fraction. Due to the nature of the tooling in this particular study, only those bubbles at the top

surface of the laminate are visible. It was explained earlier that no analysis was performed on the surface interactions (i.e. tooling shear) between the infusion oil and the transparent upper acrylic tool. This research assumes that the visible behavior is representative of bulk resin and bubble evolution. Future analysis might extend the 2D measurement of v_B to 3D bulk void content via surface chemistry (Young's Equation), geometry considerations accounting for non-ellipsoidal voids, and through-thickness flow models.

6.5.2 Void Filtering

The automated image analysis script can be divided into two parts: (1) an initial script in which a series of digital filters are presented to create a binary image showing only the voids in the image, and (2) automated application of the filter settings to multiple images and generation of results for a large data set. Data form part (1) was compared to manually void isolation (i.e. "hand painting") of the images to determine the accuracy of the method and to devise a correction function that could account for remaining noise following the automated image processing.

In order to perform the initial calibration step, a sample image was chosen from the set of captured photographs from each infusion in order to optimize the image processing filters for that sample type. The criteria for choosing a sample image was that it should have a high number of voids of a variety of shapes and sizes, relative to other images from the same test campaign. This criterion increased the probability that the filters would work across a range of void shapes and sizes.

The area of interest for this research was the region shortly behind the oil flow front. This was chosen because fluid close to the flow front is typically where the highest void content is

observed [123], and the need for high image quality required zooming in to a portion of the experimental sample. Synchronizing multiple cameras across the full sample would give a fuller picture of void flow across the sample. The script used here automatically recognizes the location of the slowest point in the flow front, draws a line perpendicular to the flow direction at that point, then defines a representative image area (RIA) behind that line as a rectangle with set dimensions. For the experimentation at hand, the RIA was extended back to 4, 6, and 8 cm from the flow front. This was to determine whether there were any significant effects of RIA size on void content measurements. Up to 8 cm back from the flow front, visible void content measurements were relatively insensitive to RIA size. It would be appropriate in future experimentation to view an entire sample with one wide-angle image (RIA width of 25 cm). Such an image would require a higher resolution camera or blending multiple images. After the region was defined, parameters for five filters were applied manually using a graphical user interface.

1. Color Filter

First, the image was split into three color channels (RGB). A monochrome green version of the original image showed the highest visible contrast between dark blue UV reflection off of carbon fiber and the bright yellow fluorescent oil. The resultant green image was then converted to grayscale for subsequent processing.

2. Threshold Filter

Next, a gray-level threshold was manually selected by the user in order to segregate voids from non-voids as accurately as possible. This is where a user needs to use good judgement to distinguish between void and non-void features. The image is then converted into a binary black

and white image with potential void space represented as white pixels, and fiber/resin space represented as black.

3. Size of Pixel Group Filter

Next, the program maps and labels each connected group of white pixels for size filtering. Size filters subsequently allow the user to set an upper and lower limit for the pixel groups. This effectively filters out regions where groups of fibers contact the acrylic creating high contrast patches which may appear like voids to the computer. It also filters out individual white pixels or small groups that represent noise. The downside of a pixel group size filter is that sometimes actual voids were eliminated from the image. For the research at hand, white pixel groups smaller than 100 pixels were eliminated. Due to the fact that some void pixels were extremely large, the maximum size was set to be 500,000. Large, non-void pixel groups which fell within this range were typically removed by successive filters.

4. High Entropy Pixel Group Filter

Void pixel groups tended to be uniform areas of white pixels. The majority of non-voids tended to be high entropy (i.e. with areas of mixed black and white pixels). By filtering out high-entropy pixel groups, blotches of fiber and other noise could be removed without removing too many void regions. The script performed this task by recognizing quantities of black to white pixels in individual pixel groups and filtering out groups with a ratio of black to white above 1/100.

5. Long & Skinny Group Filter

Finally, after applying the previous filters, prevalent long, skinny non-void pixel groups can remain in the image, generated by high contrast lines corresponding to the fiber orientation. The 45° orientation sample, for example, had a notable number of lines oriented in the fiber direction

corresponding to regions where fibers pressed against the upper surface. The other orientations saw similar noise. A filter was thus applied in which the researcher would define an orientation and aspect ratio for detecting this type of noise. For the 45° orientation, pixel groups with angles of 45 ± 2° and an aspect ratio greater than 85:1 were filtered out.

While each of these five filters may unavoidably remove some actual void content from the final image, they were visibly good at creating a binary image identifying voids. An example of images filtered by this method is shown in Figure 6-1. As can be seen, the filters allow the user to distill an image to a point where almost all of the only remaining features in the binary image are voids (actual error quantification is discussed later). The script filtering process takes some time for the user to set up, but only needs to happen once for thousands of data points. A machine learning script could conceivably be developed in the future to automatically develop unique filter parameters for each image.

6.5.3 Accuracy and Rescaling of Automated Void Fraction Results

Accuracy of the automated void detection framework was determined by selecting an image from each layup type and comparing automated vs manual void identification. For the manual approach, each void pixel identified by a user was painted white by hand on a computer. As was the case with the threshold filter mentioned earlier, the hand-painted images (for comparison) involved a transition region between void and oil. Best judgement was made by the researchers to accurately paint void space, though an error of up to 5% could reasonably be anticipated.

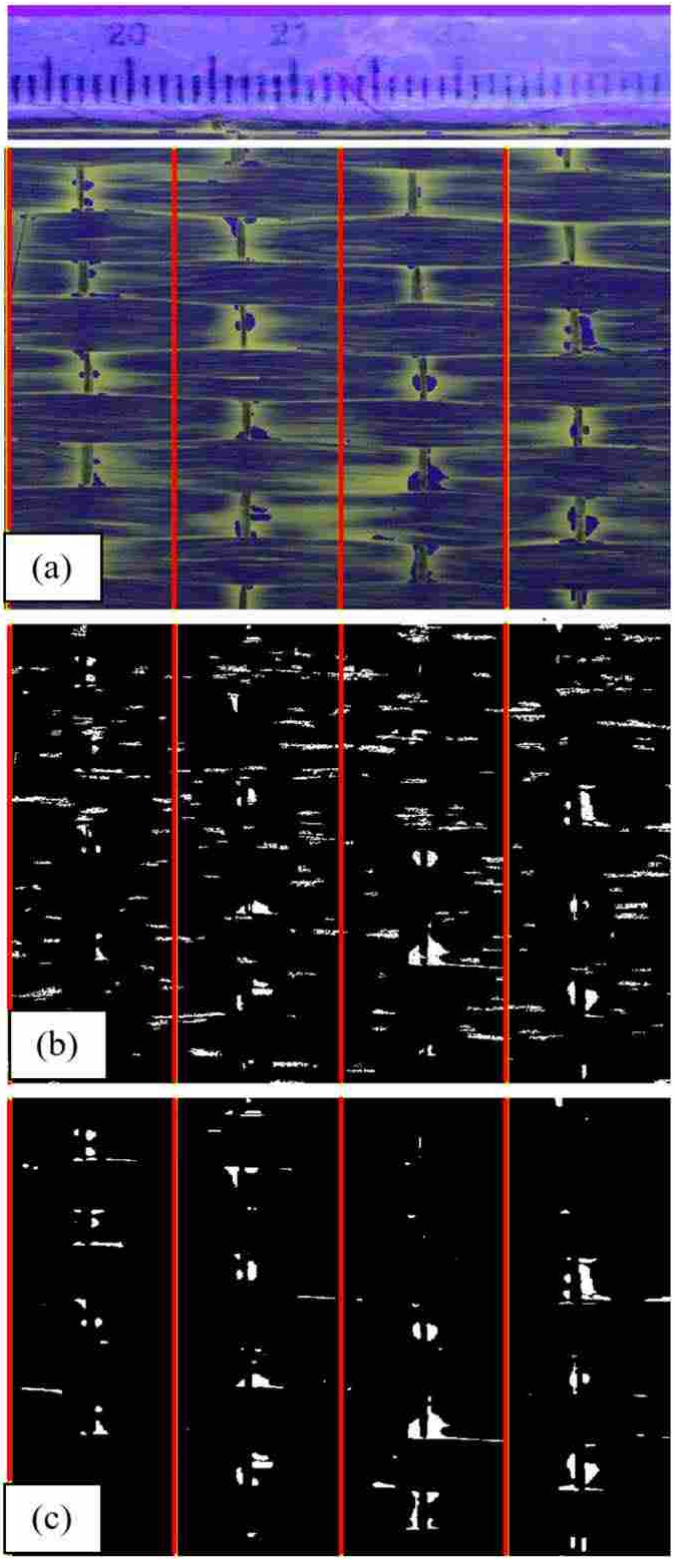

Figure 6-1: Comparison of (a) original RIA, (b) automatically generated image, and (c) manually painted image for the 0° orientation. Regions are divided into 1 cm-wide sub areas for comparison and script calibration.

A sample RIA for a 0° infusion with both methods represented is shown in Figure 6-1. The yellow regions in Fig. 1a correspond with areas where a thin film of the test fluid has pooled above the fibers due to the local depression between the weft yarns which are tightly compressed against the tooling in a vertical orientation. The darker blue regions denote voids as well as fibers pressed against the transparent tooling. Figure 6-1(b) shows void delineation in the image by the automated script, referred to as the automated void image (AVI). A visual comparison of the raw image (a) with the AVI shows visible noise but with many voids successfully identified.

Figure 6-1(c) displays the same sample image with all voids manually painted, referred to as the manual void image (MVI). This represents the best possible image, or what the program would ideally come up with, if the program recognized visible voids in the same way that the researchers did. Most of these non-void artefacts in the AVI appear to be high aspect ratio features following the shape of the tows (hence the long and skinny filter). This filter also caused some voids to be filtered out, suggesting that there is no shape filter setting that can respectively identify and dismiss all objects correctly. This disparity is identified by blue circles in Figure 6-1(a) and (b).

To compare the results of the AVI and MVI, the image was divided into equally spaced regions of 1 cm width as shown by the vertical yellow lines in Figure 6-1(a). The total areal percentage void content, v_B, for that region was tabulated according to the white area showed in both the AVI (v_{BA}) and MVI (v_{BM}) images. Figure 6-2 shows a plot of the $v_{BA}$and v_{BM}values for each of the four regions for the one image chosen from each of the three test infusions (0°, 45°, and 90° orientations).

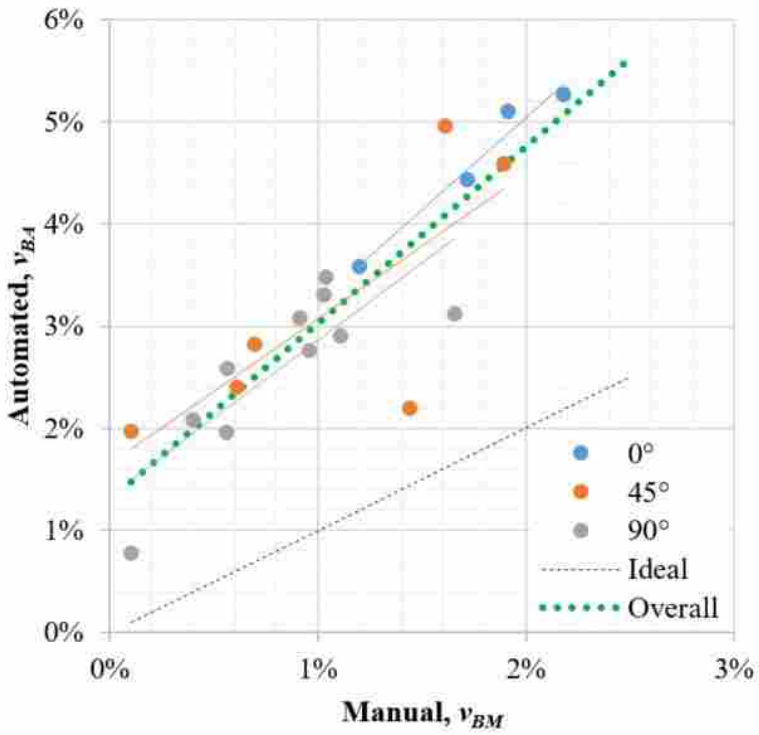

Figure 6-2: Comparison of v_{BA} and v_{BM} showing a linear trend between digitally or automatically filtered images and manually painted images; the "Ideal" line represents what a perfect agreement of manual and automated results would look like.

Note that perfect correspondence between v_B by both methods would result in a slope of 1 and intercept of 0. There is a linear relationship between $v_{BA}$and v_{BM}, though the slope is not equal to 1 and there is a vertical offset. This suggests that a the AVI corresponds to the MVI data plus a linearly (slightly) increasing amount of noise; i.e. there are roughly a constant amount of non-void pixels appearing in the AVI across the images. Hence, the automatic void results can be calibrated by the subtraction of a noise factor represented by the difference between 'Overall' and 'Ideal' in Figure 6-2. Table 6-1 shows results for each orientation, as well as a linear regression for data from all three flow orientations.

Table 6-1: Trendline parameters for data from manual and automated comparison.

Orientation	Intercept, $v_{BA}(\mathbf{0})$	Slope, dv_{BA}/dv_{BM}
Overall (Green Dotted)	1.30%	1.73
0° (Blue)	1.34%	1.52
45° (Orange)	1.65%	1.43
90° (Gray)	1.42%	1.82
Ideal (Black Dotted)	0.00%	1.00

Results from the AVI and MVI relationship were used to generate corrected measurements of v_B for the 0°, 45°, and 90° orientations. First the noise at 0% void content (the y-intercept) was subtracted from results, then v_{BA} data was divided by dv_{BA}/dv_{BM}. This correction is demonstrated in Figure 6-3, with several images chosen from distinct positions along the 250 mm sample length for each of the three flow orientations.

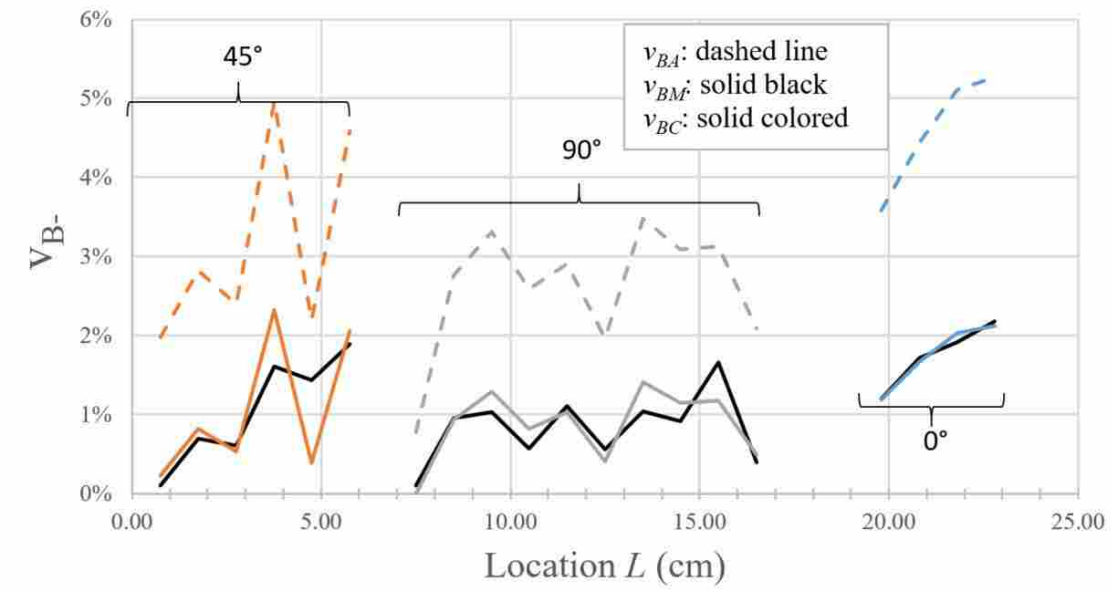

Figure 6-3: Void content correction summary; how calibrating results from the automated data (v_{BA}) to actual results (v_{BM}) leads to a reduction for the three different orientations. The locations of images chosen for calibration location corresponds to distance from the start of flow.

6.5.4 Verification of Automated Analysis

The automated void detection approach described above was applied to each image in a large set. This includes the filters as identified in the sample image for that test infusion, as well as the AVI to MVI correction. Various statistics regarding the morphology of that region's voids are then calculated by the script. A flowchart is shown in Figure 6-4 to illustrate the image filtering and subsequent calculations performed by the automated script.

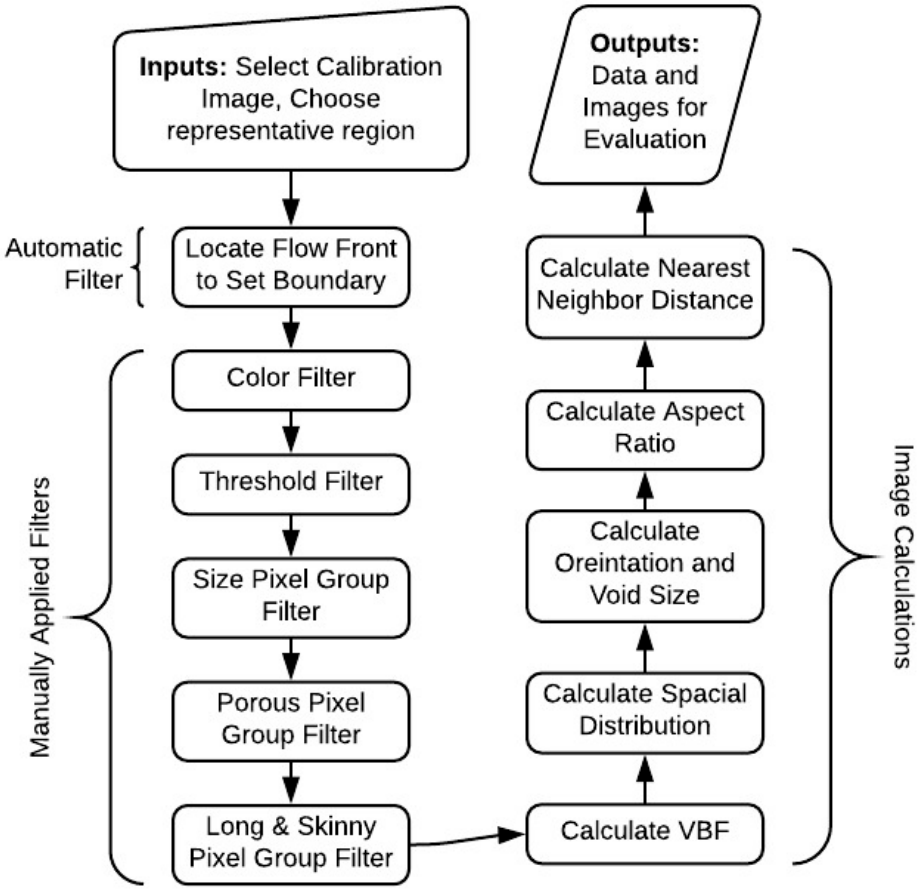

Figure 6-4: Flowchart of automated script for a single image. The script takes raw images, filters the images such that voids remain, and analyzes the images for visible void content.

6.6 Results and Discussion

6.6.1 Void Identification

The spatial distribution of voids was evaluated for the 0° sample image. Results are shown in Figure 6-5, which compares void content generated from both the AVI (non-corrected) and MVI in Figure 6-1. For the purposes of this graph, v_B is fraction of a vertical line that is identified as void, for a line of a given distance from the flow front. There is good agreement between AVI and MVI results at locations of high void content. For example, at a distance of 0.72 cm from the flow front, the highest local v_B was found to be 0.48 cm (18.6% of sample height] by the MVI, and the AVI matches this result very closely. Trends visible in the data are systematic peaks of high void content, located just under 1 cm apart, which corresponds to the spacing of the weft yarns. This critical role of weft yarns in bubble entrapment has been

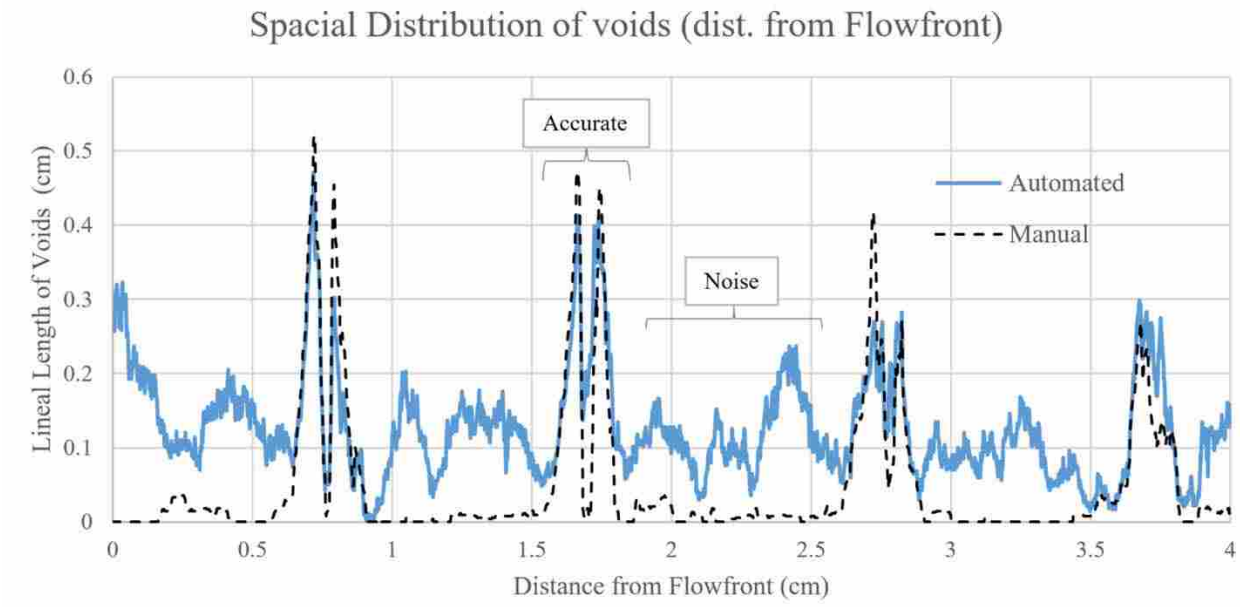

Figure 6-5: Vertical length fraction of voids across the RIA for the [0] orientation showing local maxima that correspond to weft fiber spacing. Automated data matches the peaks at weft fibers, where larger voids reside. Between weft fibers, high amounts of noise are present due to the automation mistaking fiber contrast for voids.

previously documented by micro-computed tomography (CT) analysis for another UD weave [124]. There are also random pulses of noise in the AVI results, pulsing between the weft fibers, as shown in blue between the high peaks in Figure 6-5. These pulses correspond with fiber regions, where many fibers are pressed against the acrylic. Overall, the automated results show promise in being able to describe locations and magnitude of high void concentrations.

A similar comparison between the automated and manual results in Figure 6-1(b) and 1(c) was made, showing void size distribution (Figure 6-6). The black line is for the MVI, and blue is for AVI. Results showed an average of 3.65 times as many voids of a given size in the AVI compared to the MVI. Plotting results with a log scale on the ordinate axis shows a generally consistent ratio is for void sizes across the entire range of sizes. At some void sizes the

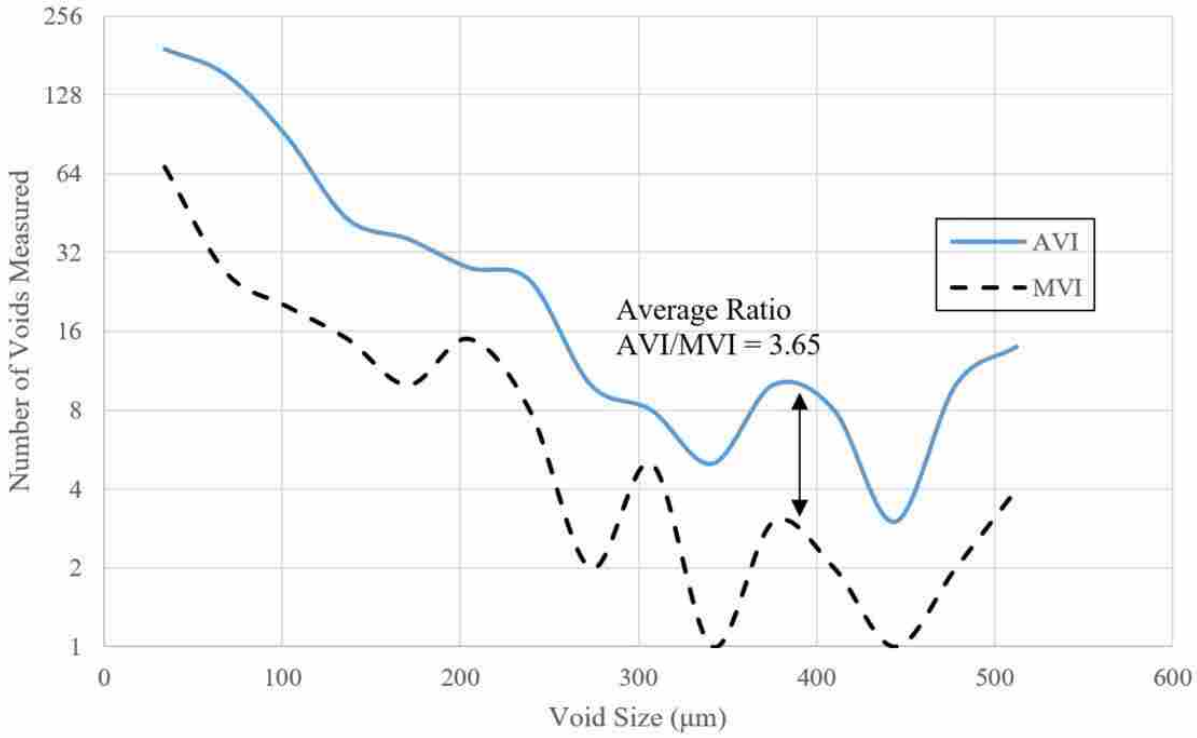

Figure 6-6: Automated (blue) and manual (black) data of void size frequency for the [0] orientation. Plotted with the ordinate axis on a log scale, the AVI and MVI have a typical ratio of 3.65.

ratio is less accurate, for example between about 250 and 350 μm and below 135 μm. This discrepancy seems to correspond with the signal to noise ratio in Figure 6-5; in the region of weft fibers, larger voids were identified well by the automated method, but small voids were over-approximated in the interim regions, accounting for the majority of the noise present in the automated approach.

6.6.1 Bubble Migration Tracking

An individual micrograph gives no information regarding velocity of the detected voids, i.e. whether they are stationary or mobile. Voids in a given image may have formed at that point, or they may have formed earlier and are moving through the fluid, escaping towards the flow front. To investigate the evolution and mobility of the voids, the void size and velocity were examined by visually comparing consecutive images at two key locations for the 0° infusion. Locations chosen were L = 12.5 cm (exactly mid-way on the 250 mm sample) and 22.5 cm. These images are shown in Figures 6-7 and 6-8, respectively. Consecutive images were taken 20 s apart. Each image is overlaid with a 20 mm x 20 mm grid, making each white sub-square area 4 mm^2. At this flow front location, the flow velocity was measured to be 4e-5 m/s.

Figure 6-7 shows void behavior in a short range behind the flow front at L = 12.5 cm. Voids circled in orange underwent no significant changes over the 20 second interval, while voids circled in light blue had changed in shape or location. Velocity and distortion rate can be computed from the grid. For example, the void circled in light blue on the top right has a speed of approximately 15^{-5} m/s. The blue-circled voids on the bottom right are moving at approximately 5^{-4} m/s. Overall, 31 voids (57% of all voids in the image) evolved in some way

between the images. The voids that moved often flowed much faster than the flow front speed. The same approach for evaluating void behavior was used near the outlet end of the sample.

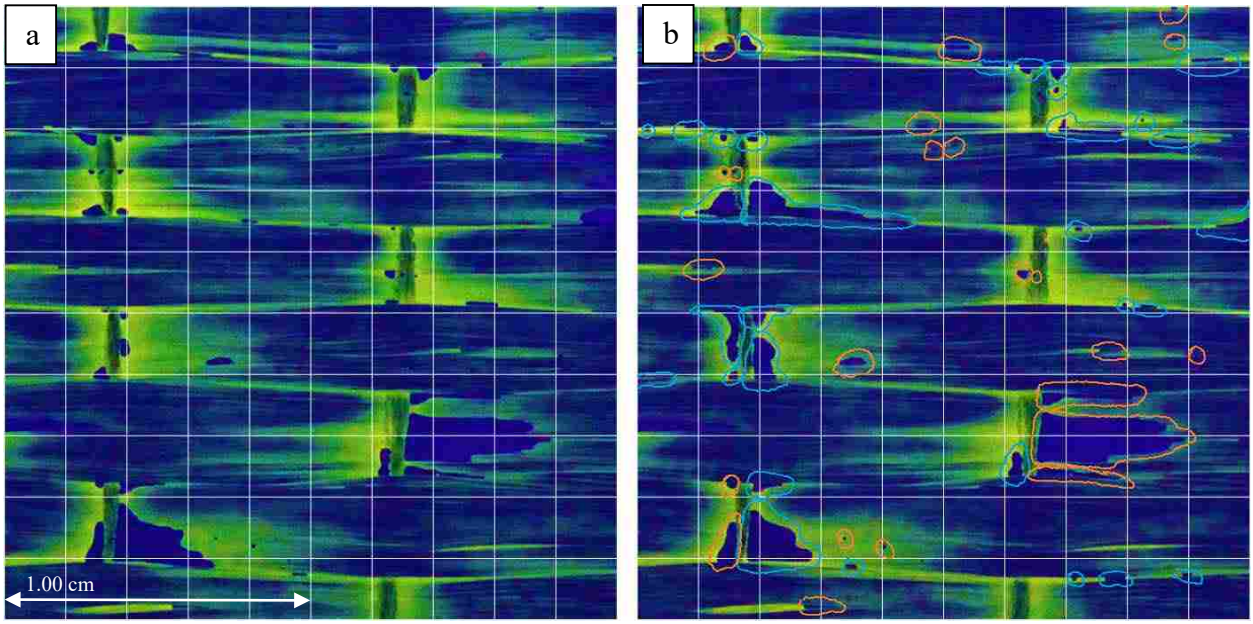

Figure 6-7: Flow front bubble migration images at L = 12.5 cm, 0° sample. The flow front is at the right boundary of each image. Image (a) was taken 20 seconds before image (b). In image (b), Migrant/evolving voids are shown circled in blue and stationary voids are shown circled in orange.

Figure 6-8 shows void behavior adjacent to the flow front when the flow front location was at L = 23.5 cm. This location is close to the outlet end of the sample, at a level where v_{BC} had plateaued (as will be shown in Figure 6-9). Circled in blue are voids that have changed. These voids are all near the right end of the sample. Of the four voids which moved during the 20 s interval between the images, two moved slightly backward toward the inlet. The two voids which moved with the flow direction had velocities of approximately 2.0e-4 m/s and 2.5e-5 m/s. Only 10% of voids in this image actually moved. For the most part, voids were entirely stationary and immobile over the 20 s interval.

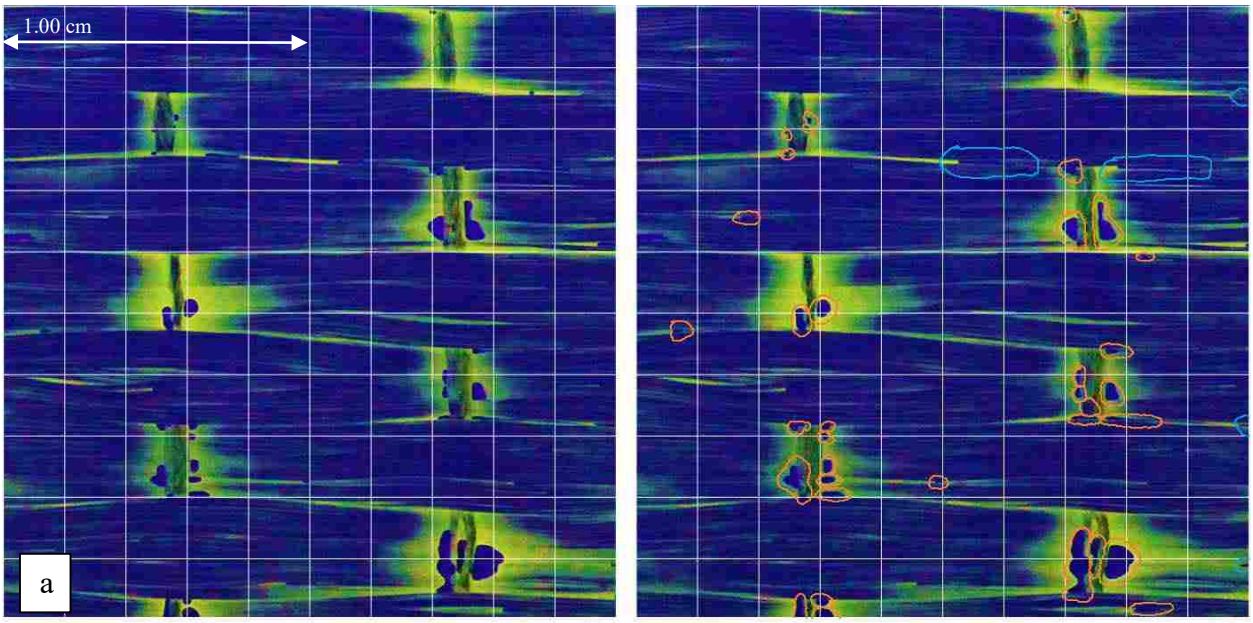

Figure 6-8: Flow front bubble migration images at L = 23.5 cm, 0° sample. The flow front is at the right boundary of each image. Image (a) was taken 20 seconds before image (b). In image (b), Migrant/evolving voids are shown circled in blue and stationary voids are shown circled in orange.

This analysis highlights a change in void mobility during the LCM process. When pressure drives flow (Figure 6-7), voids are able to move quickly along with flowing resin in between tows. Figure 6-8 shows flow with a much lower pressure gradient because the image is taken near the end of flow. At sufficiently low pressure gradients, capillary forces begin to dominate fluid behavior. Oil wicks through tows at low velocities and traps many voids in the process. This slower capillary-driven flow is typical of the late stages of such a constant-pressure infusion.

The nature of void size and mobility near the outlet is apparently totally different than that of the middle of the sample. Comparing results, it is evident that voids near the vent end (Figure 6-8) to be small, round, grouped, and stationary. Whereas at the middle of the sample

(Figure 6-7), voids have a higher variation in size, higher aspect ratios, merge and separate, and are likely to move every 20 s.

6.6.2 Flow Front Progression vs. Time

The flow front progression across many images was evaluated and compared to v_B for each of those images as determined by the corrected automated script. In the literature, void formation rates have often been related to the instantaneous flow front velocity [1,18]. The integrated version of Darcy's Law for one-dimensional flow and constant applied pressure was used to model the flow front distance from the start of the sample (L) through the time (t) of the infusion [4,78,150,151]:

$$\frac{L^2}{t} = \frac{2K_x\Delta P}{\varphi\mu} \tag{6-1}$$

Here K_x, ΔP, φ, and μ represent the flow direction permeability, the pressure drop (positive), the porosity, and the oil viscosity, respectively. Figure 6-9 shows the flow front length L vs t as experimentally measured from the images captured during a test infusion in each of the sample fiber orientations. The data was obtained by tracking the location of the slowest point in the flow front and time of each evaluated image. Best fit lines were applied to the data using the relationship $L^2 = Ct$, where $C = 2K\Delta P/(\varphi\mu)$ is regarded as constant (see Eq. 1). An important advantage of applying these fit lines is that K can be determined based on the fit line, where all other variables are known. The value in this comes from being able to ascertain permeability from the best fit line while visually comparing the fit line to the flow.

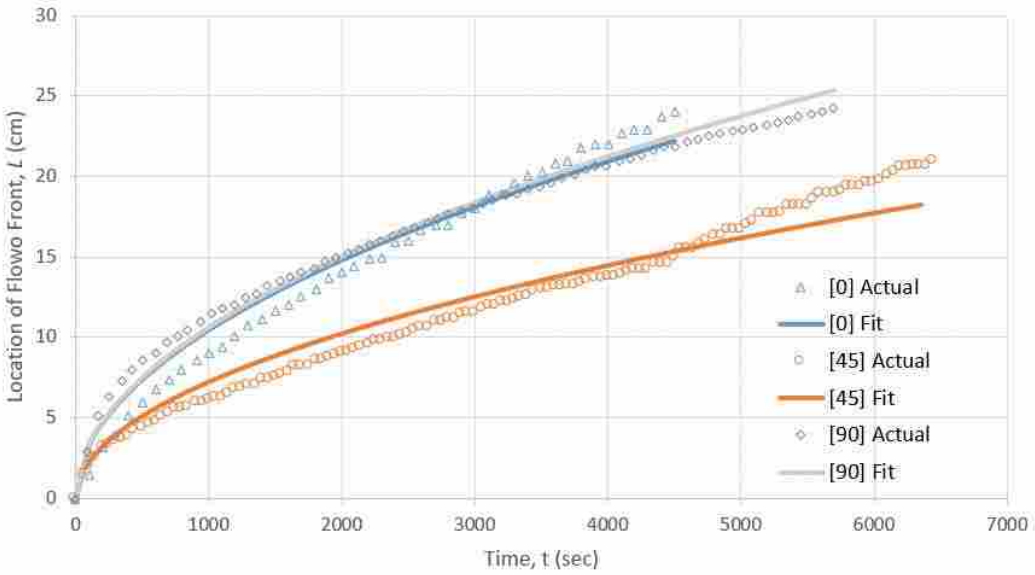

Figure 6-9: Flow front position vs. time for multiple orientations. Darcy's law was used to fit an appropriate form of trendlines.

The overall flowrate in the 90° sample was nearly identical to that of the 0° sample. The 90° test follows Darcy's Law most closely. The 45° sample showed a slower flow rate, most likely due to not having either the inter-tow gaps or the weft yarns aligned with the flow direction, thus eliminating all low-resistance flow paths. The 45° plot does not follow Darcian behavior after $L \approx 15$ cm, as the flow accelerates. The 45° plot ends at $L \approx 21$ cm because the slowest point in the flow front of the 45° sample (from which L was measured) stopped due to significant race-tracking. One of the benefits of *in situ* analysis is that infusion results can be analyzed at any point of flow, not just the using the end time required to cross the full fabric. This is useful if, for example, race tracking is seen toward the end of a sample. In contrast, post-cure analysis of the resulting laminate by microscopy would have no way of discerning between data affected and not affected by the race-tracking.

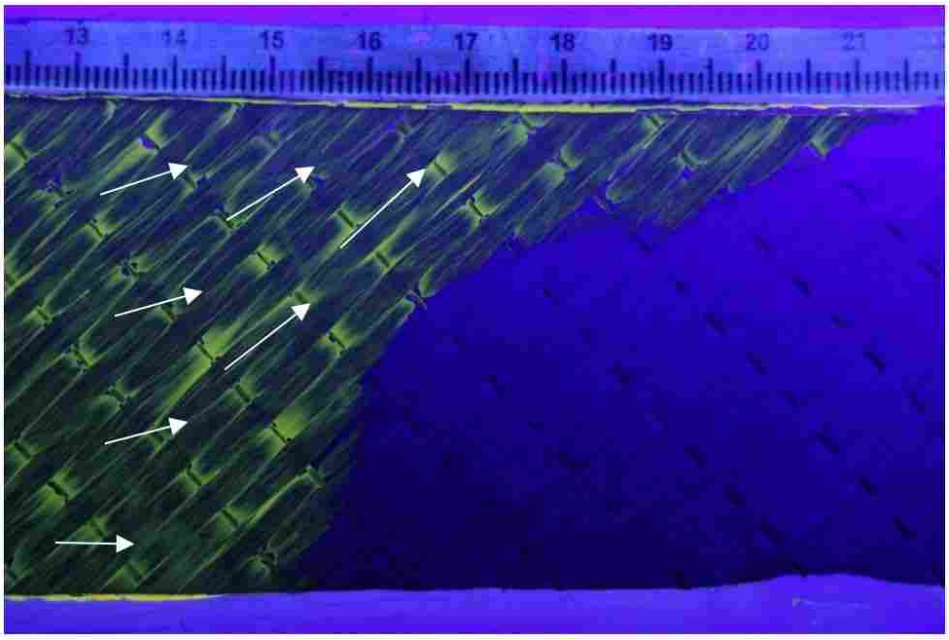

Figure 6-10: Raw image of 45° sample showing tendency of fiber flow in the 45° direction. Racetracking along top and bottom shown. Racetracking is a likely cause of the acceleration in the flow front progression of the sample after L = 15 cm, shown in Figure 6-9.

As already mentioned, the 45° sample's ply schedule is [45,-45,(45)$_2$]s. As there is a 3:2 ratio of +45° layers to -45° layers, and as flow is faster along the fiber direction, the bulk flow may favor "leaning" towards the +45° direction. The uppermost ply pressed against the tool surface is also in the +45° direction. This means that as oil flows from left to right, there is a tendency for the oil, especially in the visible uppermost layer, to build up on the top wall of the sample, which conforms to the fiber direction in that top layer. As the automated script detects the slowest point of the flow front, such flow anomalies are easily detected.

6.6.3 Void Content vs. Flow Front Progression

Images were analyzed using the rescaled automated method to determine the void content behind the flow front over time due to the automated method's tendency to measure higher than actual void content. A region for analysis was defined in each of several images for a given test infusion, referred to earlier as the RIA (a representative image area following the flow front). Several RIA sizes were considered. So long as the representative image area did not exceed 8 cm behind the sample, no significant in measured void content difference was observed. The rescaled void content, v_{BC} was then measured by the script for that region, and plotted against the length of the flow front (L) for each of the images from the 0° sample in Figure 6-11. Both script-measured v_{BA} and corrected v_{BC} plots are shown to illustrate the effects of the correction.

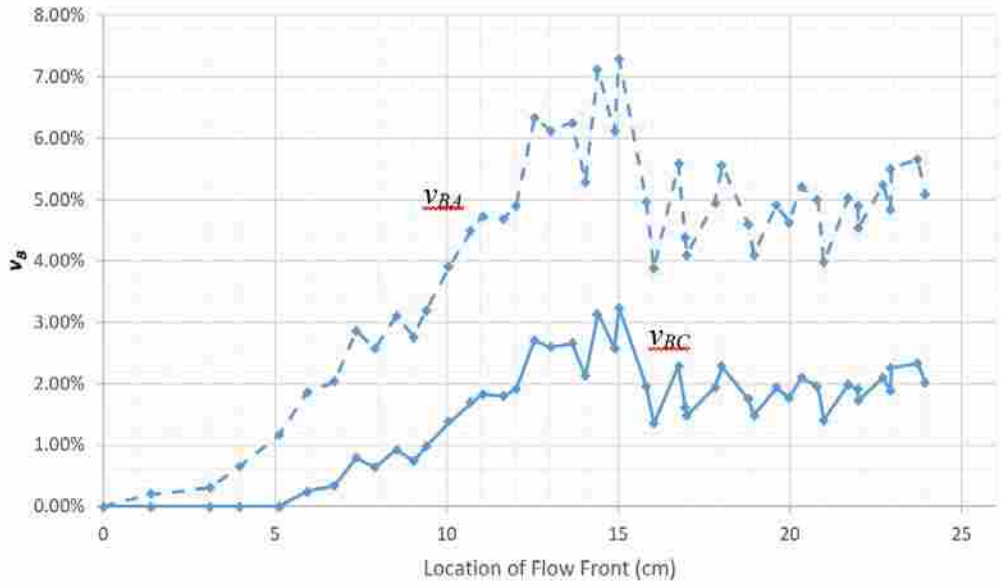

Figure 6-11: Results for both automated and corrected void content (v_{BA}, v_{BC}) as a function of flow front location, shown for 0° orientation. Corrected results involved both a vertical translation and vertical scaling, leading to "zero" void content in the first 5 cm of flow.

This increase in void content shown in Figure 6-11 is assumed to be due to the decreasing flow velocity. Decreasing flow velocity leads to greater intra-tow macro bubble formation rates as the flow capillary number drops below about 10e-5 (the typical transition point between pressure and capillary driven flow). It appears that this happens around L = 15 cm, where v_{BC} reaches a plateau. The continually decreasing velocity would result in a continual increase in macro-void formation rates, but the velocity changed little from 15 to 25 cm (as seen by a nearly constant flow rate progression in Figure 6-9), which could explain why no further increase in void concentration was seen.

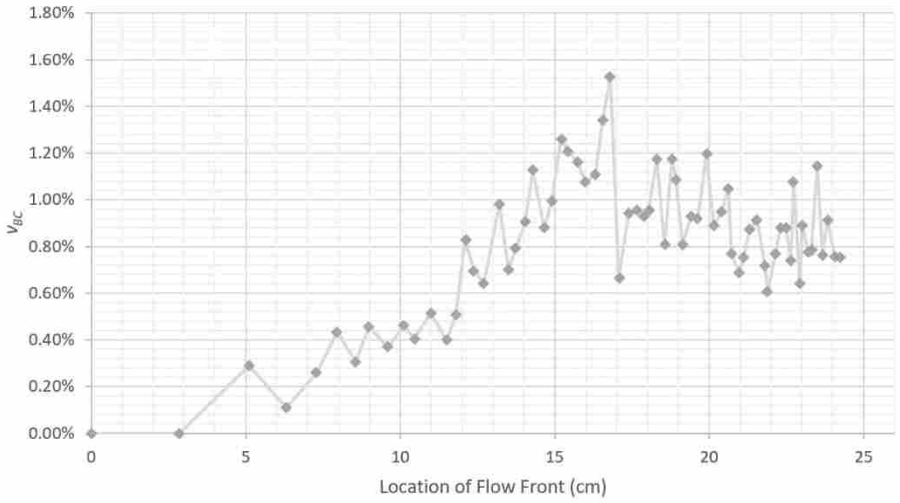

Figure 6-12: Results for corrected visible void content (v_{BC}) as a function of flow front location, shown for 90°. infrequency of peaks (wavelength) comparable to the fiber tow width.

Figure 6-12 shows similar results for the 90° test, except that local minima and maxima were more closely spaced. These oscillations corresponded with fiber tow width, suggesting that the voids concentrated at the inter-tow gaps. At L = 16.5 cm, there was a drop in visible void content. This maximum by another void content plateau region. Referring again to Figure 6-9,

this is a point where velocity appears to be constant (because flow progression is at a nearly constant rate).

The 45° sample also rose and dropped in v_{BC}, but its behavior was significantly different from that of the 0° and 90° orientations. The 45° sample showed acceleration in flow rate after about 15 cm, as shown in Figure 6-13. The drop in void content seen after 17 cm (in Figure 6-13) should match the increase in flow rate seen at 15 cm earlier (in Figure 6-9), but they do not match up (i.e. 15 cm ≠ 17 cm). The mismatch is due to the racetracking (shown in Figure 6-10).

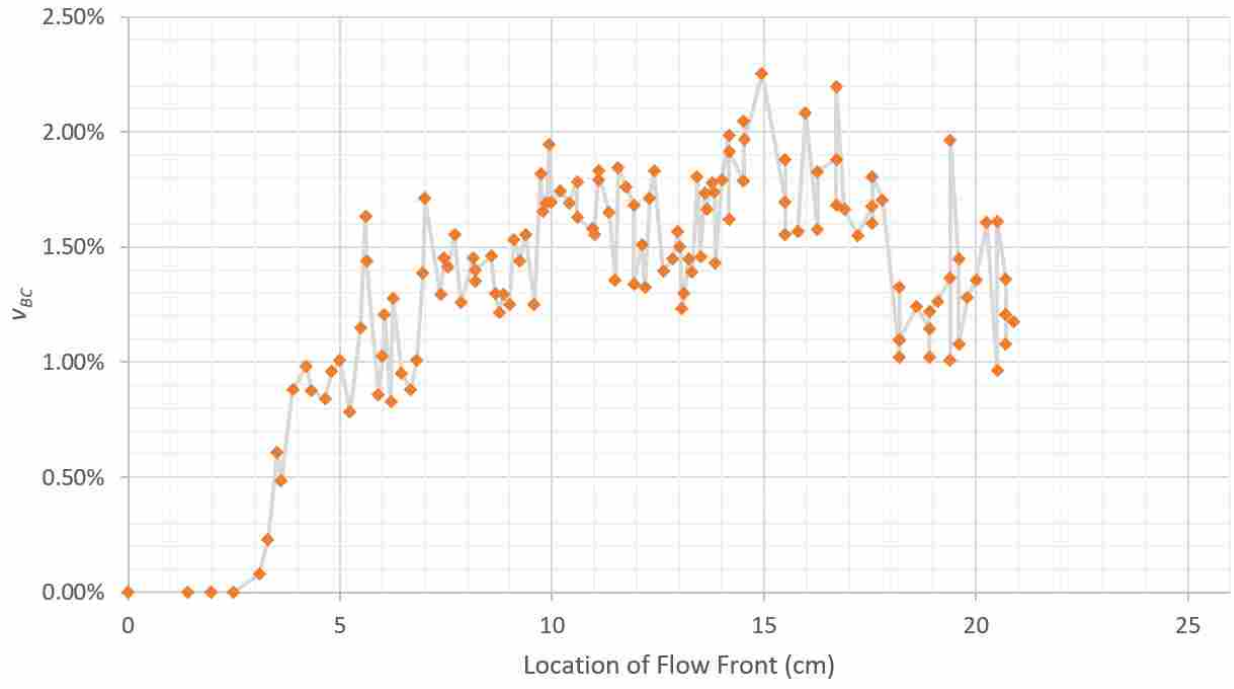

Figure 6-13: Results for corrected visible void content (v_{BC}) as a function of flow front location, shown for 45° flow. Very few voids were picked up for early flow, due to both high flow rates (forming micro- and not macro-voids) and calibration.

Though not desirable, racetracking can be insightful. In looking at Figure 6-13, one can see a drop in void content from 17-21 cm. The void content over that interval is comparable to 7-

10 cm range in the same figure. Referring back to the Figure 6-9 and looking at these same intervals, one sees identical flow front progression over time. The take-away here is that because racetracking led to faster flow later in the sample, the racetracking region void content matched an earlier portion in the sample with the same velocity.

6.6.4 Void Content vs. Flow Rate

The composite industry has shown substantial interest in comparing void content to flow rate. By such a comparison, optimal flow rates can be determined to reduce void content in LCM processing. The visible void content (v_B) was plotted against flow velocity in Figure 6-14, and showed similar behavior to the results in [110], with the v_B decreasing as flow velocity increased. The recorded v_B appears to be negligible for flow velocities greater than approximately 0.001 m/s. The figure does not account for micro-voids, which exist inside of tows and are most often formed at high flow velocities because of dominating inter-tow channel flow in dual scale reinforcements [132,152,153]. Furthermore, the experiment was driven by an atmospheric inlet and a vacuum outlet. With over-pressure creating a pressure gradient (instead of a vacuum pump), more gas is trapped inside the reinforcement prior to infusion. This leads to a higher void content, as explained in [123]. If over-pressure was driving flow with the same pressure differential, it is assumed that higher void contents at all velocities would be seen then those in Figure 6-14. This emphasizes the need during process simulation to characterize void formation at whatever applied absolute pressure is intended in the actual manufacturing.

Figure 6-14 also has three exponential trendlines shown, illustrating a “best fit” for the data. However, from such low R^2 values, visual trends are perhaps more evident. The 0° orientation shows the highest void content sensitivity to velocity, and the 90° orientation shows

the lowest. This is due to flow in parallel with open inter-tow channels governing macro-void formation. Each of the orientations shows a minimum v_B above about a flow velocity of 0.0001 m/s.

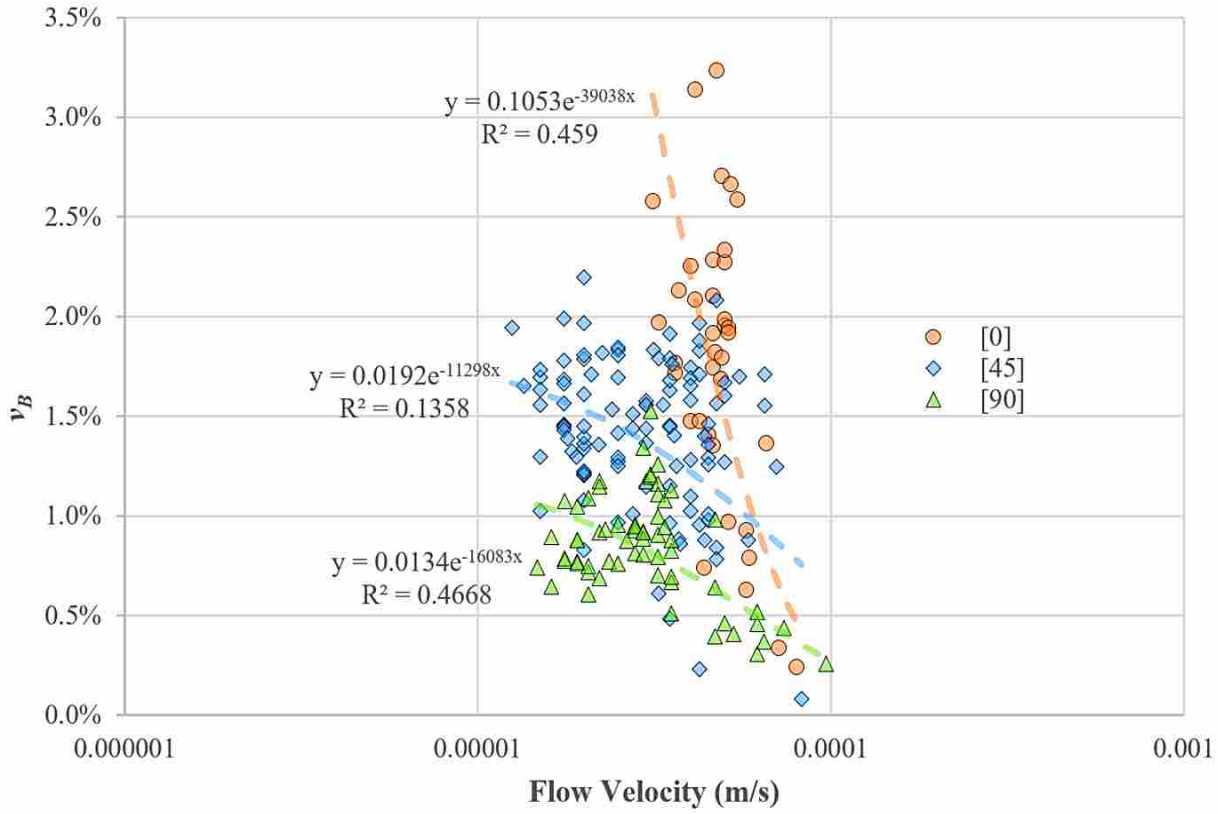

Figure 6-14: Visible void content as a function of flow velocity and orientation. Both exponential trendlines and visually following data points suggest a minimum threshold beginning at 0.0001 m/s. Low R^2 suggest a wide spread in data.

Figure 6-14 provides visible void content as a function of velocity, and suggests a minimum threshold (in this case, flow velocity below 0.0001 m/s) to avoid in order to minimize void formation. At speeds near 0.0001 m/s, one can expect $v_B < 0.5\%$ for this oil-fiber combination. Though the data presented is for canola oil/dye flowing through UD weave carbon fiber, this type of data is extremely valuable to the composites industry in terms of processing

optimization. If engineers know the optimal velocity (or velocity range) for acceptable void content, they can design processes such that resin flow never crosses a low velocity threshold. Such a range would need to also take into consideration (1) fiber washout at high velocities, (2) micro-void formation inside of tows associated with high velocity, and (3) tooling pressure limitations.

Figure 6-14 shows only macro void behavior (or voids formed in between channels). An example of this is shown earlier in Figure 6-1, where the detected voids are located on top of, or between the tows, but not within the tow structure. Smaller micro-voids form and typically reside within the tows themselves, within the tightly packed tows of opaque carbon fiber. These intra-tow micro voids are expected to increase in formation rates with higher flow velocities [154]. Such velocities may be seen at the beginning of the flow experiments, when the flow front velocity is the fastest in a constant-pressure infusion. The absence of detected micro-voids is due to either absence true lack of them, an inability to detect them due to camera resolution, or the opacity of the fibers creating dark areas surrounding the micro-voids (Figure 6-1(a)).

This particular UD weave had a lower permeability than most composite reinforcements presented in the literature. Low permeability led to low flow rate, which may have remained low enough throughout the infusion to never result in high formation rates of micro-voids (which are entrapped inside of tows during high inter-tow channel flow). Further testing at higher pressures (and therefore higher velocities) is planned to validate this theory.

Besides velocity, the temperature and surface chemistry between the fluid and tooling, are also thought to affect the resulting bubble formation and thus the visible void content. The temperature of a fluid affects its ability to absorb gas, with higher temperature resin absorbing more gas (e.g. Henry's Law). Temperature and gas volume are also related (e.g. ideal gas law).

Tooling surface chemistry in the case of this study depends on the surface tension of the oil and the contact angle between the acrylic tool and the oil. The surface chemistry of oil against acrylic was not studied in the research at hand, but may cause significantly different bubble formation from that of epoxy on steel tooling, for example. The canola oil used was similar to infusion resin in both surface tension and viscosity. But no analysis was made to assess the contact angle differences between the resin and canola oil. The dependence of bubble formation on such surface chemistry could be evaluated by repeating the current experiments with a wetting agent applied to the acrylic tool surface, and should be considered in future work. The purpose of the research was primarily to generate high resolution images and demonstrate how an automated program could shed light on flow phenomena.

Other limitations have to do with the visibility limitations of the experimental tooling. Only the top surface is visible. Transient bubbles are often non-spherical and constrained by fiber geometries. Bubbles may be "stuck" to a weft fiber on one end, and pulled along on the other to have a misleadingly large visible area. Hence while the image analysis may accurately show the visible (aerial) void fraction, it is necessary for these images to be correlated to void content through the sample thickness in future work.

Several other opportunities are possible for future work on void flow monitoring of carbon fiber. One essential area for study is to consider the error associated with this method. A useful way to assess this would be to perform constant flowrate tests (within tool pressure limitations) over a single or multiple RIAs in order to determine the repeatability of visible void content measurement at a constant velocity. Future work should include correlating data from fluorescent void flow monitoring with physically created parts to measure the predictive ability of this *in situ* method.

6.7 Conclusion

A framework for automated *in situ* detection of bubble evolution in carbon fiber composites has been developed. The framework provides information on how to obtain high-contrast, high-resolution images of matrix bubbles migrating through carbon fiber using a fluorescent dye-oil mixture, a UV light, and a DSLR digital camera. Visible void content from images was filtered out and analyzed using an automated script.

Results were compared to hand-painted images to assess accuracy. On average, automatically obtained results produced about 3.65 times the number of voids. This was due to not being able to filter out some of the noise in the images. However, a plot comparing automatically obtained and manually obtained void content was given, showing that the automatic script can be easily calibrated for higher accuracy.

The script was found to be most accurate when tracking large voids along weft fibers. The script was least accurate in tracking smaller voids between tows. Pulses of noise (i.e. script recognizing some fibers as voids) were shown to exist in regions between weft fibers. Typically, the script would misinterpret fibers for voids when sufficiently high contrast regions between fluid and fiber was present.

Several other insights were found from tracking *in situ* flow in carbon fiber. Due to the large volume of data that can be obtained through automated image analysis, hundreds of images were compared to evaluate void content as a function of flow velocity. For the oil-fiber combination present in this research, a minimum velocity of 0.0001 m/s was shown to yield the lowest visible void fraction ($v_B < 0.5\%$).

Automated analysis enables researchers to obtain significantly more data when performing 1D flow tests. For example, flow front progression was tracked for different orientations.

Racetracking in one 45º sample led to ending the infusion test before resin reached the outlet, but sufficient data was available from the hundreds of data points obtained earlier to model flow behavior, track visible void content migration, and estimate the velocity for minimum void formation.

Fiber orientation was shown to affect void content. Analysis studied *in situ* 1D flow for reinforcement oriented at 0º, 45º, and 90º; all three orientations showed similar minimum void formation velocity, but different behavior for lower velocities. Flow more parallel to fibers and inter-tow fiber channels showed the highest amount of void content for velocities under 0.0001 m/s. Flow perpendicular to fibers yielded the lowest void content formation for the same velocities.

Not only was void content captured in images, but so was the evolution and migration of bubbles. Data showed several differences between flow behavior when the flow front was at the middle of the sample and when the flow front was at the end of the sample (near the outlet). Bubble size, flow rate, evolution rate, and count were substantially different. This was due to pressure-driven flow in the middle of the sample and capillary-driven flow toward the end (outlet).

7 COST OF VOID CONTENT IN PER PROCESS AND PART COUNT

7.1 Introduction

Aerospace applications of composite materials continues to grow and spread. In order for a composite part to be "aerospace grade," low void content is essential. Lower void content leads to better mechanical properties. But low void content comes with a price, and is highly dependent on the manufacturing processes involved in production. However, very few models exist which actually identify the production cost effects of void content (without paying a premium). This paper provides aims at providing a model for estimating the cost per part as a function of void content and number of parts produced. The goal is to generate a rule of thumb calculator to help industry members know when it is economically viable to switch to a liquid composite molding (LCM) process. In this research, the model developed from publications available to the public, industry members, and researcher experience in the composites industry. The model approximates the cost per part for mid-sized aerostructures made by a variety of processes.

7.2 Background and Literature

Void content (v_B) is a driving design variable for aerostructure and other high-performance parts. Void content is defined as the volume percent of open space to total composite. Voids usually take on the form of air bubbles trapped inside the final cured part.

Voids are a driving design variable because of their effects on composite part mechanical properties. One author has found that as v_B increases, mechanical properties greatly diminish [102]. Both matrix and fiber dominated properties are affected [155]. For typical aerospace parts, a v_B of 2% or less is desirable. This is because of the strong negative effects of v_B on compressive strength of composite structures. In some cases, as in the case of a filament wound rocket engine housing, v_B can be substantially higher, but that is only because the housing is primarily loaded in tension, not compression. Compressive strength is known in industry to be more dramatically reduced by voids, by the formation of kink bands due to micro-buckling [156-158].

The effects of v_B on mechanical properties has been a topic of continued interest [159]. Efforts to minimize v_B continue in various processes. Efforts are also aimed at reducing the cost of producing high-performance composites, often by utilizing optimized liquid composite molding (LCM) techniques. These processes have historically produced higher void content, but trends in process optimization and void content characterization are promising. Now, many high-grade aerospace parts are made using (LCM).

However, to obtain the best mechanical properties in a composite structure, one must still utilize expensive special processes and materials. The most prominent example of expensive composites processing includes prepreg materials and an autoclave. Autoclave processes and prepreg laminates are integral to producing the lowest v_c in composites. Vacuum bagging and resin flow monitoring are closing the gap in void content. There are many other processes of which void content is an area of research. As the v_B gap closes, it is becoming ever more important to identify the best process to produce parts of sufficiently low void content while keeping costs low.

Commercial software is available to help composites manufacturers estimate the cost of potential composite parts and processes [160,161]. However, annual licenses for effective software is often unavailable – especially for the production of mid-sized aerostructures. To add some clarity to this issue, a new cost model is developed. Data is obtained from the proceedings of an international cost estimating conference (ICEAA) [162] using a program called SEER®, and extended to determine the cost per part as a function of void content. The model predicts the cost per part for void content ranging between 0.3% and 7.5% for mid-sized composite aerostructures.

7.3 Method

Several factors must be taken into account to come up with a good estimate of the cost associated with void content. First, a typical model was evaluated. Then, the model was simplified and developed using empirical data to determine a new model that incorporates void content.

A typical model for cost estimation (C) would include such factors as: manufacturing process (P), tooling and equipment cost (T), labor cost (L), materials cost (M), and the number of parts produced (n):

$$C = C(P, T, L, M, n) \tag{7-1}$$

A model for cost per part is therefore defined by:

$$\frac{dC}{dn} = \dot{c} = \dot{c}(P, T, L, M, n) \tag{7-2}$$

Or simply:

$$C = n\dot{c} \tag{7-3}$$

Before a new model for $\dot{c}$ is established (with respect to void content), it is important to review other cost factors. The manufacturing method (P) is important because void content is inherently related to processing. For example, with autoclave-related processes, a much lower void content is possible because autoclaves can apply tremendous pressure (reaching up to 85 atm in many cases). Following the ideal gas law, we can assume that there is an inversely proportional relationship between pressure and gas bubble volume. The ideal gas law is not a perfect representation of void behavior under pressure, but it adequately describes the relationship between applied pressure and void size.

Tooling and equipment cost (T) factor into the cost of a part. As the number of parts increases, the cost per part from tooling and equipment lessens inversely to part number. This is critical when creating parts with large upfront costs, such as expensive tooling with low coefficient of thermal expansion, massive autoclaves (reaching well over $100K for a small autoclave), vacuum pumps, automated fiber placement machines, and so forth.

Labor (L) plays an important role in the cost of void content. With labor-intensive processes, especially with those in which automation is limited, part price is closely related to the number of hours worked. Automated fiber placement processes require many hours for the initial set up only. After the process is programmed and tuned, relatively very little hours are required to create an entire part. Typically, the energy and maintenance costs of running equipment are far less than the labor costs required to manually create parts.

Materials (M) play a large role in processing. Prepreg composites are expensive, typically have a shelf life of a few months, and produce significant amounts of non-reusable scrap. Reinforcement fibers (whether in prepreg or dry weave) are very expensive because their tensile and compressive stress limits drive light-weight, high-performance design. Resins, particularly specialty resins like high service temperature epoxies or phenolics, can drive up the price per part.

One of the biggest factors in determining part cost is the number of units produced (n). As production volume increases, the rate typically levels off near the cost of labor and materials. One exception is the VARTM process where the cost per part varies less as production volume changes. This is because cost is composed almost entirely of materials and labor. As well, only a one-sided mold, vacuum pump and typical composite materials are necessary to begin production.

These factors were researched, and a data set was found which incorporates all of these factors. Information regarding cost per process was found in an ICEAA (International Cost Estimating and Analysis Association) publication, a commercial software (SEER®) for evaluating total cost of a process. This information showed the cost per part of various processes at different production volumes. This information also included ratios of labor, equipment and tooling, and materials. However, this data did not incorporate the cost of an autoclave in certain processes. Knowledge of typical void content percentages in the aerospace were researched. For example, it is common knowledge that VARTM and RTM processes reach v_B around 2% for most aerospace applications, as the 2% line is an industry standard for high-performance parts. Estimates on void content were compared to each of the process costs to determine the cost per part with respect to void content. These estimates were developed by combining data available

from an ICEAA paper [162] and consulting with the aerospace industry representative from Albany International. In summary, the data already presented a model of the factors identified in the cost estimation function mentioned earlier.

After acquiring empirical data for cost per part, the data was compared to standard void content values. Thus a new definition of cost per part in terms of volume fraction was developed; $\dot{c} = \dot{c}(v_B)$. A power law was used to describe behavior.

In order to understand the processes compared in the data, descriptions are provided. Processes were as follows: Automated fiber placement (AFP), Resin Transfer Molding (RTM), Vacuum Assisted Resin Transfer Molding (VARTM), SF-TP (Stamp Formed Automated Tape Placement), and Wet Layup (WL). AFP data was developed for an autoclave. However, the data in the ICEAA publication did not incorporate the high up-front costs for an autoclave. Thus an additional $100,000 was divided by the number of parts produced and added to the cost. It was not clear whether the costs listed in the ICEAA publication incorporated energy usage and maintenance costs. As well, the costs listed were assumed to mean the average cost per part and not the differential cost per part.

Also note that the ICEAA publication data was also constrained to an example geometry, a concave layup of 600mm x 600mm x 100mm, 3 plies thick, 0.6 mm, without core or stiffeners. The example geometry allows for general design considerations, while still being applicable to high performance aerospace parts. The value of this research, therefore, is highest for mid-sized parts with (1) positive draft, (2) 3D-countour, (3) constant gage, and (4) high-performance applications. [162]

All parts presented in the ICEAA publication were processed for low void content, perhaps $v_B < 3\%$, thus in order to obtain higher void content values, estimations needed to be made. Particularly, the data from WL was estimated to have a void content of 7.5% by removing the autoclave portion of its processing. This estimation is a low approximation for WLv_B, but is justified by assuming that a part made with WL was not placed in an autoclave. Thus the part cost is significantly lower than a WL part made in an autoclave.

7.4 Results

Data was gathered and organized for the cost per part of various processes, void contents, and production counts. Acronyms in the Process column are describe in the Method. v_B represents void content, v_B Low and High represent lower and upper bounds, respectively. n shows the number of parts produced for the corresponding cost per part. Results are presented in Table 7-1 and Figure 7-1.

Table 7-1: Cost per part ($\dot{c}$) compared to process, v_B, and n

Process	v_B Low	v_B	v_B High	$n = 100$	$n = 500$	$n = 1000$	$n = 2000$
AFP	0.17%	0.30%	2.00%	$ 1,534	$ 520	$ 405	$ 345
RTM	2.00%	2.00%	5.00%	$ 953	$ 365	$ 295	$ 250
VARTM	1.90%	2.50%	5.00%	$ 499	$ 475	$ 460	$ 450
SF-TP	1.00%	3.00%	5.00%	$ 446	$ 195	$ 170	$ 150
WL	5.00%	7.50%	10.00%	$ 368	$ 345	$ 320	$ 305

Figure 7-1 shows Cost per part was plotted as a function of void content and organized into part count groups.

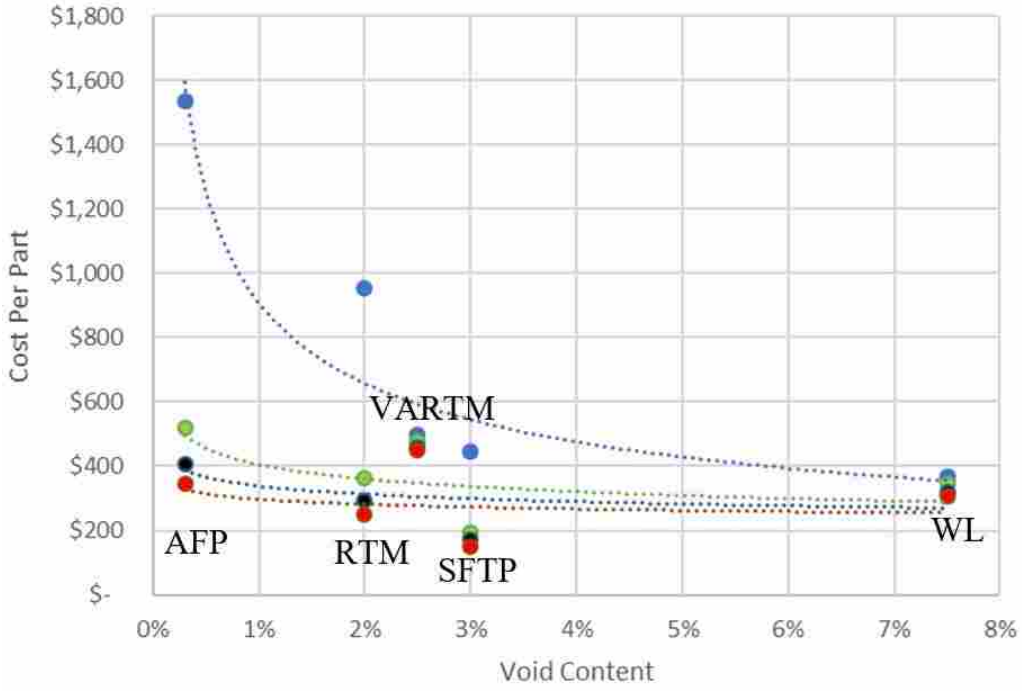

Figure 7-1: Cost per part for n=100 (blue), n=500 (green), n=1000 (black), n=2000 (red)

Overall, as void content increases, the cost per part lowers. As the number of parts produced increases, the cost per part lowers. Vertically aligned data points represent part costs of the same process. In order from left to right, vertical clusters are AFP, RTM, VARTM, SF-TP, and WL. Power law trendlines appear to be good fits for most data, except for the data with a void content of 2.5%. This represents the VARTM process. VARTM cost per part is nearly independent of the number or parts produced. Thus there is a cluster between $450 and $499 at $v_B = 2.5\%$.

In general, the cost per part, $\dot{c}$, can be represented by the function,

$$\dot{c} = a{v_c}^r \tag{7-4}$$

Where n is the number of parts produced, and a and r are fitting constants. In Table 7-2, values of a and r are shown for various part counts.

7-2: Fit curves and constants

n	a	r
100	106.03	-0.466
500	186.17	-0.169
1000	202.22	-0.112
2000	208.29	-0.077

Total cost can therefore be estimated by

$$C = \dot{c}n \tag{7-5}$$

Or, equivalently,

$$C = n \cdot a{v_B}^r \tag{7-6}$$

If production count, n, is not known, a cost per part estimate, $\dot{c}_{est}$, can be approximated by

$$\dot{c}_{est}(v_B) = 169.81{v_c}^{-0.206} \tag{7-7}$$

This model was established from a power law trendline with the four different n values and is therefore useful for $n \in (100,2000)$ and $v_c \in (0.3,7.5)$. Data error ranges are shown in Table 7-1.

7.5 Conclusion and Discussion

Models of cost per part are presented for a range representing mid-size aerostructures produced using a variety of void contents. By using the models, one can effectively estimate the cost of a change in void content on a particular part. For example, by reducing the void content from 3% to 2% does not dramatically change the cost of production per part for larger part

counts. However, changing from 1.5% to 0.5% v_B substantially increases cost per part. The cost per part function is more sensitive to changes in v_B at lower v_B.

VARTM processes show the least cost sensitivity to part count. This suggests that of the options listed, VARTM processes are most economically desirable for low void content (~2.5%) and low part count (n = 100). For higher part counts, RTM processes (v_B = ~2.0%) are more desirable. Trends in industry reflect this small sensitivity; liquid composite molding (LCM) processes (including VARTM and RTM) are becoming more common for advanced applications as (1) engineers use processing optimization to reduce void content, and (2) as demand for composite parts increases.

It is with this trend (the shift to LCM) in mind that motivates creasing simple models to help the industry to decide when to switch to opportune processing improvements, such as a switch to VARTM. A useful test of the model provided in this literature would be to choose an aerostructure design that fits in the models parameters. Then one could use the model to draw conclusions about which test to employ for the desired void content and cost per part. After the model was employed, one could compare results with data obtained through commercial software, such as SEER®, to identify limitations and opportunities in the model.

Some opportunities for improvement that are not dependent on software involved pinging industry members for data. For example, filament winding, a common process for composite parts, was not evaluated. By vetting this model with a number of experienced composites engineers, more data can be added and the model can be refined. It is not, however, the goal of this model to become as accurate as commercial software. The aim of this model is to help with initial process design decisions and to develop an intuition for part cost dependence on void content.

8 CONCLUSION

LCM is growing in importance alternative to traditional prepreg-autoclave methods for manufacture aerospace composites, especially as the demand for *more* composites of *lower* void content increases. The most significant roadblock to industry's implementation of LCM is the optimization of resin flow to ensure these high quality parts. This study aimed at contributing process optimization tools to facilitate the adaptation of LCM. This goal was accomplished.

8.1 Observations and Summaries

The dissertation consisted of research done to characterize the permeability of reinforcement fabrics under various processing conditions (3D flow, curvature, and shear) using a highly packed unidirectional weave fabric. Efforts were successful in investigating *in-situ* bubble flow as has not been previously seen in literature. The goal of extending understanding of LCM and pushing forward the state of the art via sub-studies was successful. The contributions and findings of the five chapters, or manuscripts, are listed below.

Chapter 3 set the groundwork for permeability analysis in LCM by reviewing and extending the current theory for assessing 3D permeability of reinforcement fabrics using an ellipsoidal point infusion experiment. The aim was to improve permeability measurement accuracy for LCM processing models. Various ellipsoidal flow solutions exist in literature, but most of these introduce error with the geometric assumption that the inlet shape could be treated

as an ellipse (simplifying the math to flow out to an elliptical flow front). However, this assumption was proven to be introduce a minimum error of 46%. For thin samples, the error was especially large. The research here was the first to compare solutions in the context of 75 experiments. Modifications to available solutions were suggested, which simplify convergence and reduce error.

Chapters 4 and 5 extended permeability analysis from ideal flat plate geometries to curved and sheared geometries, typical to real-world aerostructures. The motivation for these geometries came from a close working relationship with industry partners, who sought to understand flow behavior of highly packed aerospace grade carbon fiber.

Chapter 4 demonstrated a new method for the permeability measurement of fabric with local curvature, based on a vertically oriented curve and vacuum bagging. A correlation was shown between curvature (as evaluated over four radii) and effective permeability, which is likely related to higher compression around a corner for vacuum bag forming. Two mathematical approaches were considered, and it was shown that the harmonic-average permeability (though common for flow regions in series) was not effective for computing reasonable results.

Chapter 5 investigated the effects of shear beyond the shear-locking angle for the research fabric. Although the permeability of locally sheared fabric has been studied up to the shear-locking angle, nothing has looked beyond that; however, modern reinforcements with low shear-locking angle are commonly used in aerospace instead of legacy weaves. The study showed that the full permeability tensor increased for mid-range shear angles beyond the shear-locking angle due to fabric undulations. These undulations were caused by fabric compression while being sheared in-plane. Even though fiber volume fraction increased as shear increased, the permeability of the fabric actually also increased for medium-range shear angles (~16°).

Permeability increase at mid-range angles was seen for all directions of the permeability tensor. However, permeability is shown to decrease with higher shear (~37°) angles beyond the shear-locking angle as fiber volume fraction maximizes; i.e. the fabric became so compressed that the undulations were no longer enough to increase flow.

Chapter 6 researched improving the resolution and automation of *in-situ* infusion of carbon fiber. Motivation for the research was that mechanical properties of an LCM-manufactured aerospace part can be improved when process modeling incorporates minimization of void content. Such models require an understanding of bubble formation and migration during LCM. But has previously been challenging to monitor void flow in-situ with carbon fiber reinforcements because of fiber opacity. The research built upon a new fluorescent imaging method to monitor void flow in-situ, and did so successfully. Results show higher resolution (bubble contrast) than ever before compared to previous *in-situ* optical analyses. An automated script was developed to allow rapid analysis of thousands of images. This method was validated by comparing to automatically- to manually analyzed images. A linear relationship was shown between automatically- and manually-measured image void content. The improved image contrast and speed of analysis allowed generating void formation vs. velocity curves with substantially more data points than ever before seen in literature.

And finally, Chapter 7 investigated the cost motivation for LCM. In light of the composites industry's growing interest in LCM processes for aerospace applications, the cost of different processes was evaluated to help industry members know when to make the switch from prepreg-autoclave processes to LCM. A short cost summary of typical processes for manufacturing aerospace composite parts was provided. Cost data was based on publicly available SEER® results and organized to show the cost per aerospace part with respect to part

count and process. Data showed that LCM is a financially wise alternative to automated fiber placement (prepreg-autoclave) manufacturing when a void content of 2-2.5% was acceptable.

8.2 Conclusions

Using 75 experiments representing a wide range of materials and test conditions, the Mekic method for measuring 3D permeability are recommended [6], because it correctly assumes a circular inlet shape. For curvature under vacuum bagging, a reduction in permeability for fabrics draped over curvature was shown with decreasing radius; this can reasonably be attributed a change in volume fraction. For fabrics with in-plane shear at mid-range shear angles, total permeability can increase beyond the shear locking angle because of micro-undulations that form in the reinforcement.

The method presented for automatically analyzing visible void content in carbon fiber processing *in situ* was shown to be easily calibrated for good accuracy. The method was particularly accurate for measuring macro-voids along weft fibers. Void content vs. flow velocity was plotted, showing a minimum void content can be obtained for velocities around 0.0001 m/s for the fluid-reinforcement system. Fiber orientations were shown to affect void content vs. flow velocity, with flow in the fiber-direction being most sensitive to velocity. VARTM was recommended as the most economical process for making less than ~500 parts and RTM was shown as economical for making more than ~500 parts, so long as an acceptable 2-2.5% void content is permissible.

REFERENCES

[1] Khnel M, Kraus T, The global CFRP market 2016. In: International Composites Congress. November, 28 2016, 2016.

[2] Ashby M. Materials Selection in Mechanical Design: Fourth Edition. , 2010.

[3] McIlhagger A, Archer E, McIlhagger R. Manufacturing processes for composite materials and components for aerospace applications. In: Anonymous Polymer Composites in the Aerospace Industry. : Elsevier, 2014. p. 53-75.

[4] Darcy H. Les Fontaines Publiques De La Ville De Dijon: Exposition Et Application... : Victor Dalmont, 1856.

[5] Rudd CD, Long AC, Kendall KN, Mangin C. Liquid Moulding Technologies: Resin Transfer Moulding, Structural Reaction Injection Moulding and Related Processing Techniques. : Elsevier, 1997.

[6] Mekic S, Akhatov I, Ulven C. A radial infusion model for transverse permeability measurements of fiber reinforcement in composite materials. Polymer Composites 2009;30(7):907-917.

[7] Arbter R, Beraud JM, Binetruy C, Bizet L, Bréard J, Comas-Cardona S, Demaria C, Endruweit A, Ermanni P, Gommer F, Hasanovic S, Henrat P, Klunker F, Laine B, Lavanchy S, Lomov SV, Long A, Michaud V, Morren G, Ruiz E, Sol H, Trochu F, Verleye B, Wietgrefe M, Wu W, Ziegmann G. Experimental determination of the permeability of textiles: A benchmark exercise. Composites Part A: Applied Science and Manufacturing 2011;42(9):1157-1168.

[8] Vernet N, Ruiz E, Advani S, Alms JB, Aubert M, Barburski M, Barari B, Beraud JM, Berg DC, Correia N, Danzi M, Delavière T, Dickert M, Di Fratta C, Endruweit A, Ermanni P, Francucci G, Garcia JA, George A, Hahn C, Klunker F, Lomov SV, Long A, Louis B, Maldonado J, Meier R, Michaud V, Perrin H, Pillai K, Rodriguez E, Trochu F, Verheyden S, Wietgrefe M, Xiong W, Zaremba S, Ziegmann G. Experimental determination of the permeability of engineering textiles: Benchmark II. Composites Part A: Applied Science and Manufacturing 2014;61(0):172-184.

[9] Causse N, Benchimol S, Martineau L, Carponcin D, Lonjon A, Fogel M, Dandurand J, Dantras E, Lacabanne C. Polymerization study and rheological behavior of a RTM6 epoxy

resin system during preprocessing step. Journal of Thermal Analysis & Calorimetry 2015;119(1):329-336.

[10] George A. RTM6 Rheology and DSC. 2012.

[11] Kazilas MC. Acquisition and interpretation of dielectric data for thermoset cure monitoring. 2003.

[12] Tsamasphyros GJ. Some Analytical Solutions of the Kamal Equation for Isothermal Curing With Applications to Composite Patch Repair. Journal of engineering materials and technology 2009;131(1).

[13] Pichaud S, Duteurtre X, Fit A, Stephan F, Maazouz A, Pascault J. Chemorheological and dielectric study of epoxy-amine for processing control. Polym Int 1999;48(12):1205-1218.

[14] George A. Optimization of resin infusion processing for composite materials: simulation and characterization strategies. 2011.

[15] Modi D, Johnson M, Long A, Rudd C. Analysis of pressure profile and flow progression in the vacuum infusion process. Composites Sci Technol 2009;69(9):1458-1464.

[16] Sirtautas J, Pickett AK, George A. Materials characterisation and analysis for flow simulation of liquid resin infusion. Applied Composite Materials 2015;22(3):323-341.

[17] Robitaille F, Gauvin R. Compaction of textile reinforcements for composites manufacturing. I: Review of experimental results. Polymer Composites 1998;19(2):198-216.

[18] Grimsley, BW. Characterization of the Vacuum Assisted Resin Transfer Molding Process for Fabrication of Aerospace Composites. 2005.

[19] Hannibal PM. Compressibility Measurement and Modeling to Optimize Flow Simulation of Vacuum Infusion Processing for Composite Materials. 2015.

[20] George A, Hannibal P, Morgan M, Hoagland D, Stapleton SE. Compressibility measurement of composite reinforcements for flow simulation of vacuum infusion. Polymer Composites 2018.

[21] Simácek P, Advani SG. Desirable features in mold filling simulations for Liquid Composite Molding processes. Polymer Composites 2004;25(4):355-367.

[22] Steenkamer D, McKnight SH, Wilkins DJ, Karbhari VM. Experimental characterization of permeability and fibre wetting for liquid moulding. J Mater Sci 1995;30(12):3207-3215.

[23] Woerdeman DL, Phelan FR, Parnas RS. Interpretation of 3-D permeability measurements for RTM modeling. Polymer Composites 1995;16(6):470-480.

[24] Mogavero J, Advani SG. Experimental investigation of flow through multi-layered preforms. Polymer Composites 1997;18(5):649-655.

[25] Song YS, Heider D, Youn JR. Statistical characteristics of out-of-plane permeability for plain-woven structure. Polymer Composites 2009;30(10):1465-1472.

[26] Pillai KM. Modeling the unsaturated flow in liquid composite molding processes: a review and some thoughts. J Composite Mater 2004;38(23):2097-2118.

[27] Trevino L, Rupel K, Young WB, Liou MJ, Lee LJ. Analysis of resin injection molding in molds with preplaced fiber mats. I: Permeability and compressibility measurements. Polymer Composites 1991;12(1):20-29.

[28] Drapier S, Monatte J, Elbouazzaoui O, Henrat P. Characterization of transient through-thickness permeabilities of non crimp new concept (NC2) multiaxial fabrics. Composites Part A: Applied Science and Manufacturing 2005;36(7):877-892.

[29] Scholz S, Gillespie Jr. JW, Heider D. Measurement of transverse permeability using gaseous and liquid flow. Composites Part A: Applied Science and Manufacturing 2007;38(9):2034-2040.

[30] Comas-Cardona S, Binetruy C, Krawczak P. Unidirectional compression of fibre reinforcements. Part 2: A continuous permeability tensor measurement. Composites Sci Technol 2007;67(3):638-645.

[31] Klunker F, Danzi M, Ermanni P. Fiber deformation as a result of fluid injection: modeling and validation in the case of saturated permeability measurements in through thickness direction. J Composite Mater 2015;49(9):1091-1105.

[32] Becker D, Mitschang P. Influence of preforming technology on the out-of-plane impregnation behavior of textiles. Composites Part A: Applied Science and Manufacturing 2015;77:248-256.

[33] Swery EE, Allen T, Comas-Cardona S, Govignon Q, Hickey C, Timms J, Tournier L, Walbran A, Kelly P, Bickerton S. Efficient experimental characterisation of the permeability of fibrous textiles. J Composite Mater 2016;50(28):4023-4038.

[34] Wu C, James Wang T, James Lee L. Trans-plane fluid permeability measurement and its applications in liquid composite molding. Polymer Composites 1994;15(4):289-298.

[35] Dungan FD, Sastry AM. Saturated and unsaturated polymer flows: microphenomena and modeling. J Composite Mater 2002;36(13):1581-1603.

[36] Gokce A, Chohra M, Advani SG, Walsh SM. Permeability estimation algorithm to simultaneously characterize the distribution media and the fabric preform in vacuum assisted resin transfer molding process. Composites Sci Technol 2005;65(14):2129-2139.

[37] Okonkwo K, Simacek P, Advani SG, Parnas RS. Characterization of 3D fiber preform permeability tensor in radial flow using an inverse algorithm based on sensors and simulation. Composites Part A: Applied Science and Manufacturing 2011;42(10):1283-1292.

[38] Yun M, Sas H, Simacek P, Advani SG. Characterization of 3D fabric permeability with skew terms. Composites Part A: Applied Science and Manufacturing 2017;97:51-59.

[39] Ahn SH, Lee WI, Springer GS. Measurement of the three-dimensional permeability of fiber preforms using embedded fiber optic sensors. J Composite Mater 1995;29(6):714-733.

[40] Weitzenböck JR, Shenoi RA, Wilson PA. Measurement of three-dimensional permeability. Composites Part A: Applied Science and Manufacturing 1998;29(1-2):159-169.

[41] Ballata WO, Walsh SM, Advani S. Determination of the transverse permeability of a fiber preform. J Reinf Plast Compos 1999;18(16):1450-1464.

[42] Nedanov PB, Advani SG. A Method to Determine 3D Permeability of Fibrous Reinforcements. J Composite Mater 2002;36(2):241-254.

[43] George A, Brandley M, Dart R, Peterson C. Rigid Tooling for Optical 3D Wetting Permeability Measurements.

[44] Konstantopoulos S, Hueber C, Mühlbachler E, Schledjewski R. Identification of the effect of typical curvatures encountered in RTM parts on localized permeability of fibrous preforms. Advanced Manufacturing: Polymer & Composites Science 2016:1-10.

[45] Weitzenböck JR, Shenoi RA, Wilson PA. Radial flow permeability measurement. Part B: Application. Composites part A: applied science and manufacturing 1999;30(6):797-813.

[46] Stven T, Weyrauch F, Mitschang P, Neitzel M. Continuous monitoring of three-dimensional resin flow through a fibre preform. Composites Part A: Applied Science and Manufacturing 2003;34(6):475-480.

[47] Jiang JH, Wang ZX, Chen NL, Measurement of transverse permeability of fabric preforms using ultrasound monitoring technique in LCM processes. In: Advanced Materials Research. , 2011. p. 214-217.

[48] Brard J, Saouab A, Bouquet G. Dependence of the reinforcement anisotropy on a three dimensional resin flow observed by X-ray radioscopy. J Reinf Plast Compos 1999;18(9):814-826.

[49] Weitzenböck JR, Shenoi RA, Wilson PA. Radial flow permeability measurement. Part A: Theory. Composites Part A: Applied Science and Manufacturing 1999;30(6):781-796.

[50] Ahn KJ, Seferis JC, Berg JC. Simultaneous measurements of permeability and capillary pressure of thermosetting matrices in woven fabric reinforcements. Polymer composites 1991;12(3):146-152.

[51] Amico S, Lekakou C. An experimental study of the permeability and capillary pressure in resin-transfer moulding. Composites Sci Technol 2001;61(13):1945-1959.

[52] Adams KL, Russel WB, Rebenfeld L. Radial penetration of a viscous liquid into a planar anisotropic porous medium. Int J Multiphase Flow 1988;14(2):203-215.

[53] Mekic S, Akhatov IS, Ulven CA. Analysis of a radial infusion model for in-plane permeability measurements of fiber reinforcement in composite materials. Polymer Composites 2009;30(12):1788-1799.

[54] Lagarias JC, Reeds JA, Wright MH, Wright PE. Convergence properties of the Nelder--Mead simplex method in low dimensions. SIAM Journal on optimization 1998;9(1):112-147.

[55] Turner DZ, Hjelmstad KD. Determining the 3D permeability of fibrous media using the Newton method. Composites Part B: Engineering 2005;36(8):609-618.

[56] Liu Q, Parnas RS, Giffard HS. New set-up for in-plane permeability measurement. Composites Part A: Applied Science and Manufacturing 2007;38(3):954-962.

[57] Stadtfeld HC, Erninger M, Bickerton S, Advani SG. An experimental method to continuously measure permeability of fiber preforms as a function of fiber volume fraction. J Reinf Plast Compos 2002;21(10):879-899.

[58] Friedman HL, Johnson RA, Miller B, Salem DR, Parnas RS. Forced in-plane flow through complex deformable structures: Influence of an imposed curve. Polymer Composites 1997;18(5):663-671.

[59] Friedman HL, Johnson RA, Gusev V, Neimark AV, Buvel D, Salem DR, Parnas RS. Visualization and quantification of forced in-plane flow through deformed porous media. Polymer Composites 1999;20(5):613-627.

[60] Jain LK, Lutton BG, Mai Y, Paton R. Stresses and deformations induced during manufacturing. Part II: a study of the spring-in phenomenon. J Composite Mater 1997;31(7):696-719.

[61] Naji MI, Hoa SV. Curing of thick angle-bend thermoset composite part: curing cycle effect on thickness variation and fiber volume fraction. J Reinf Plast Compos 1999;18(8):702-723.

[62] Oakeshott JL. Warpage of carbon–epoxy composite channels. Plastics, rubber and composites 2003;32(3):104-113.

[63] Feih S, Shercliff HR. Quality assessment of curved composite components in peel joint structures. Composites Part A: Applied Science and Manufacturing 2005;36(3):397-408.

[64] Yoon M, Baidoo J, Gillespie JW, Heider D. Vacuum assisted resin transfer molding (VARTM) process incorporating gravitational effects: a closed-form solution. J Composite Mater 2005;39(24):2227-2242.

[65] Bickerton S, Sozer EM, Graham PJ, Advani SG. Fabric structure and mold curvature effects on preform permeability and mold filling in the RTM process. Part I. Experiments. Composites Part A: Applied Science and Manufacturing 2000;31(5):423-438.

[66] Bickerton S, Sozer EM, Šimácek P, Advani SG. Fabric structure and mold curvature effects on preform permeability and mold filling in the RTM process. Part II. Predictions and comparisons with experiments. Composites Part A: Applied Science and Manufacturing 2000;31(5):439-458.

[67] Sun J, Li Y, Li M, Gu Y, Zhang Z. Numerical study on effects of interaction between rubber mould and lay-up on consolidation of L-shaped laminates in autoclave process. Polym Polym Compos 2011;19(4/5):271.

[68] Batch GL, Cumiskey S, Macosko CW. Compaction of fiber reinforcements. Polymer composites 2002;23(3):307-318.

[69] Causse P, Ruiz E, Trochu F. Experimental study of flexible injection to manufacture parts of strong curvature. Polymer Composites 2011;32(6):882-895.

[70] Causse P, Ruiz E, Trochu F. Influence of preforming on the quality of curved composite parts manufactured by flexible injection. International journal of material forming 2013;6(3):341-362.

[71] Hubert P, Poursartip A. Aspects of the compaction of composite angle laminates: an experimental investigation. J Composite Mater 2001;35(1):2-26.

[72] Lawrence JM, Hsiao K, Don RC, Simacek P, Estrada G, Sozer EM, Stadtfeld HC, Advani SG. An approach to couple mold design and on-line control to manufacture complex composite parts by resin transfer molding. Composites Part A: Applied Science and Manufacturing 2002;33(7):981-990.

[73] Nakatani H, Adachi K, Osaka K. RESIN IMPREGNATION BEHAVIOR IN THICK CARBON FIBRE COMPOSITE WITH A CORNER DURING VARTM PROCESS. 2016.

[74] Sas HS. Addressing variability of fiber preform permeability in process design for liquid composite molding. 2015.

[75] Wendling A, Hivet G, Vidal-Sallé E, Boisse P. Consistent geometrical modelling of interlock fabrics. Finite Elements Anal Des 2014;90:93-105.

[76] Vectorply C-L 0900 Spec. Sheet v.7. 2015;2018(May 28).

[77] Walther J, Simacek P, Advani SG. The effect of fabric and fiber tow shear on dual scale flow and fiber bundle saturation during liquid molding of textile composites. International journal of material forming 2012;5(1):83-97.

[78] Simácek P, Advani SG. Permeability model for a woven fabric. Polymer Composites 1996;17(6):887-899.

[79] Advani SG, Bruschke MV, Parnas RS. Resin transfer molding flow phenomena in polymeric composites. Composite materials series 1994:465.

[80] Grujicic M, Chittajallu KM, Walsh S. Effect of shear, compaction and nesting on permeability of the orthogonal plain-weave fabric preforms. Mater Chem Phys 2004;86(2–3):358-369.

[81] Endruweit A, Ermanni P. The in-plane permeability of sheared textiles. Experimental observations and a predictive conversion model. Composites Part A: Applied Science and Manufacturing 2004;35(4):439-451.

[82] Wong CC, Long AC, Sherburn M, Robitaille F, Harrison P, Rudd CD. Comparisons of novel and efficient approaches for permeability prediction based on the fabric architecture. Composites Part A: Applied Science and Manufacturing 2006;37(6):847-857.

[83] Arnold M, Cojutti M, Mitschang P. Influence of the shearing of textiles on the in-plane permeability. ICCM19 2013.

[84] Heardman E, Lekakou C, Bader MG. In-plane permeability of sheared fabrics. Composites Part A: Applied Science and Manufacturing 2001;32(7):933-940.

[85] Ueda S, Gutowski T. Anisotropic permeability of deformed woven fabrics. Composites Part A 1993.

[86] Rudd C, Long AC, McGeehin P, Smith P. In-plane permeability determination for simulation of liquid composite molding of complex shapes. Polymer Composites 1996;17(1):52-59.

[87] Smith P, Rudd CD, Long AC. The effect of shear deformation on the processing and mechanical properties of aligned reinforcements. Composites Sci Technol 1997;57(3):327-344.

[88] Demaria C, Ruiz E, Trochu F. In-plane anisotropic permeability characterization of deformed woven fabrics by unidirectional injection. Part II: Prediction model and numerical simulations. Polymer Composites 2007;28(6):812-827.

[89] Demaria C, Ruiz E, Trochu F. In-plane anisotropic permeability characterization of deformed woven fabrics by unidirectional injection. Part I: Experimental results. Polymer Composites 2007;28(6):797-811.

[90] Louis M, Huber U. Investigation of shearing effects on the permeability of woven fabrics and implementation into LCM simulation. Composites Sci Technol 2003;63(14):2081-2088.

[91] Slade J, Sozer EM, Advani SG. Fluid impregnation of deformed preforms. J Reinf Plast Compos 2000;19(7):552-568.

[92] Verleye B, Croce R, Griebel M, Klitz M, Lomov SV, Morren G, Sol H, Verpoest I, Roose D. Permeability of textile reinforcements: Simulation, influence of shear and validation. Composites Sci Technol 2008;68(13):2804-2810.

[93] Rimmel O, Becker D, Mitschang P. Maximizing the out-of-plane-permeability of preforms manufactured by dry fiber placement. Advanced Manufacturing: Polymer & Composites Science 2016;2(3-4):93-102.

[94] Aranda S, Berg DC, Dickert M, Drechsel M, Ziegmann G. Influence of shear on the permeability tensor and compaction behaviour of a non-crimp fabric. Composites Part B: Engineering 2014;65:158-163.

[95] Liotier P-, Govignon Q, Swery E, Drapier S, Bickerton S. Characterisation of woven flax fibres reinforcements: Effect of the shear on the in-plane permeability. J Compos Mater 2015;49(27):3415-3430.

[96] George A, Brandley M, Dart R, Peterson C. Characterization and optimization of optical 3D wetting measurements of through-thickness permeability. FPCM Conference Proceedings 2014.

[97] Shilin Y, Fei Y, Dequan L, Yongjing L. Unsaturated flow characteristics in dual-scale fibre fabrics at one-dimensional constant flow rate. Sci Eng Compos Mater 2016;23(6):617-624.

[98] George A, Lystrup C, Fullwood D. Performance of alternative solutions for permeability calculation during ellipsoidal flow. 2018.

[99] Hoagland D, George A. Continuous permeability measurement during unidirectional vacuum infusion processing. J Reinf Plast Compos 2017;36(22):1618-1628.

[100] 2017 Top Markets Report Composites Sector Snapshot. U.S. Department of Commerce International Trade Commission 2017.

[101] Mazumdar S. State of the Composites Industry Report for 2017. Composites Manufacturing Magazine 2016.

[102] Liu L, Zhang B, Wang D, Wu Z. Effects of cure cycles on void content and mechanical properties of composite laminates. Composite Structures 2006;73(3):303-309.

[103] Liu L, Guo ZS, Zhang BM. Experimental investigation of porosity and its effects on interlaminar shear strength in composite laminates. Int SAMPE Sym 2006;51:1-7.

[104] Lundstrom TS, Gebart BR. Influence from process parameters on void formation in resin transfer molding. Polymer Composites 1994;15(1):25-33.

[105] Frishfelds V, Lundstrm TS, Jakovics A. Bubble motion through non-crimp fabrics during composites manufacturing. Composites Part A: Applied Science and Manufacturing 2008;39(2):243-251.

[106] Lundstrom TS. Measurement of void collapse during resin transfer moulding. Composites Part A: Applied Science and Manufacturing 1997;28(3):201-214.

[107] Lundstrm TS. Bubble transport through constricted capillary tubes with application to resin transfer molding. Polymer Composites 1996;17(6):770-779.

[108] Ruiz E, Achim V, Soukane S, Trochu F, Bréard J. Optimization of injection flow rate to minimize micro/macro-voids formation in resin transfer molded composites. Composites Sci Technol 2006;66(3–4):475-486.

[109] Michaud V, Nordlund M, Lundstrm S, Mnsson JE, Capillary phenomena in liquid composite moulding. In: International Conference on Composite Materials: 08/07/2007-13/07/2007. , 2007.

[110] Patel N, Lee LJ. Effects of fiber mat architecture on void formation and removal in liquid composite molding. Polymer Composites 1995;16(5):386-399.

[111] Park CH, Lebel A, Saouab A, Bréard J, Lee WI. Modeling and simulation of voids and saturation in liquid composite molding processes. Composites Part A: Applied Science and Manufacturing 2011;42(6):658-668.

[112] Trochu F, Ruiz E, Achim V, Soukane S. Advanced numerical simulation of liquid composite molding for process analysis and optimization. Composites Part A: Applied Science and Manufacturing 2006;37(6):890-902.

[113] Lundstrm TS, Frishfelds V, Jakovics A. Bubble formation and motion in non-crimp fabrics with perturbed bundle geometry. Composites Part A: Applied Science and Manufacturing 2010;41(1):83-92.

[114] Patel N, Lee LJ. Modeling of void formation and removal in liquid composite molding. Part I: Wettability analysis. Polymer Composites 1996;17(1):96-103.

[115] Patel N, Lee LJ. Modeling of void formation and removal in liquid composite molding. Part II: Model development and implementation. Polymer Composites 1996;17(1):104-114.

[116] Leclerc JS, Ruiz E. Porosity reduction using optimized flow velocity in Resin Transfer Molding. Composites Part A: Applied Science and Manufacturing 2008;39(12):1859-1868.

[117] Labat L, Grisel M, Bréard J, Bouquet G. Original use of electrical conductivity for void detection due to injection conditions of composite materials. Comptes Rendus de l'Académie des Sciences-Series IIB-Mechanics 2001;329(7):529-534.

[118] Saraswat M, Heider D, Song Y. Ultrasonic monitoring of the void formation during VARTM infusion. Research Reviews. Center for Composite Materials, Delaware 2006.

[119] Endruweit A, Long AC, Robitaille F, Rudd CD. Influence of stochastic fibre angle variations on the permeability of bi-directional textile fabrics. Composites Part A: Applied Science and Manufacturing 2006;37(1):122-132.

[120] Abdelwahed MAB, Wielhorski Y, Bizet L, Brard J. Bubble Shape and Transport During LCM Processes: Experimental Modeling in a T-Junction Tube. arXiv preprint arXiv:1207.4099 2012.

[121] Gangloff JJ, Hwang WR, Advani SG. Characterization of bubble mobility in channel flow with fibrous porous media walls. Int J Multiphase Flow 2014;60:76-86.

[122] Aaboud B, Saouab A, Nawab Y. Simulation of air bubble′s creation, compression, and transport phenomena in resin transfer moulding. J Compos Mater 2017;51(29):4115-4127.

[123] Lundstrom TS, Gebart BR, Lundemo CY. Void formation in RTM. J Reinf Plast Compos 1993;12(12):1339-1349.

[124] Sisodia SM, Garcea SC, George AR, Fullwood DT, Spearing SM, Gamstedt EK. High-resolution computed tomography in resin infused woven carbon fibre composites with voids. Composites Sci Technol 2016;131:12-21.

[125] Judd NC, Wright WW. Voids and their effects on the mechanical properties of composites- an appraisal. SAMPE J 1978;14:10-14.

[126] Ghiorse SR. Effect of void content on the mechanical properties of carbon/epoxy laminates. SAMPE quarterly 1993;24(2):54-59.

[127] Sisodia S, Gamstedt EK, Edgren F, Varna J. Effects of voids on quasi-static and tension fatigue behaviour of carbon-fibre composite laminates. J Composite Mater 2015;49(17):2137-2148.

[128] Haider M, Hubert P, Lessard L. An experimental investigation of class A surface finish of composites made by the resin transfer molding process. Composites Sci Technol 2007;67(15):3176-3186.

[129] Lambert J, Chambers AR, Sinclair I, Spearing SM. 3D damage characterisation and the role of voids in the fatigue of wind turbine blade materials. Composites Sci Technol 2012;72(2):337-343.

[130] Varna J, Joffe R, Berglund LA, Lundstrm TS. Effect of voids on failure mechanisms in RTM laminates. Composites Sci Technol 1995;53(2):241-249.

[131] George A, Brandley M, Dart R, Fullwood D, Void modeling in resin infusion. In: CAMX 2014 - Composites and Advanced Materials Expo: Combined Strength. Unsurpassed Innovation. , 2014.

[132] LeBel F, Fanaei AE, Ruiz E, Trochu F. Prediction of optimal flow front velocity to minimize void formation in dual scale fibrous reinforcements. Int J Mater Form 2014;7(1):93-116.

[133] Yenilmez B, Murat Sozer E. A grid of dielectric sensors to monitor mold filling and resin cure in resin transfer molding. Composites Part A: Applied Science and Manufacturing 2009;40(4):476-489.

[134] Hamidi YK, Aktas L, Altan MC. Effect of packing on void morphology in resin transfer molded E-glass/epoxy composites. Polymer composites 2005;26(5):614-627.

[135] Gourichon B, Binetruy C, Krawczak P. A new numerical procedure to predict dynamic void content in liquid composite molding. Composites Part A: Applied Science and Manufacturing 2006;37(11):1961-1969.

[136] Verrey J, Michaud V, Månson J. Dynamic capillary effects in liquid composite moulding with non-crimp fabrics. Composites Part A: Applied Science and Manufacturing 2006;37(1):92-102.

[137] Ravey C, Ruiz E, Trochu F, RTM optimal injection velocity determination by capillary rise measurements using Infrared thermography. In: Iccm19. , 2013. p. 4174-83.

[138] Villiere M, et al., Experimental study on the identification of saturation of a porous media through thermal analysis. In: Iccm19. , 2013. p. 2218-27.

[139] Vilà J, Sket F, Wilde F, Requena G, González C, LLorca J. An in situ investigation of microscopic infusion and void transport during vacuum-assisted infiltration by means of X-ray computed tomography. Composites Science and Technology 2015;119(Supplement C):12-19.

[140] Straumit I, Hahn C, Winterstein E, Plank B, Lomov SV, Wevers M. Computation of permeability of a non-crimp carbon textile reinforcement based on X-ray computed tomography images. Composites Part A: Applied Science and Manufacturing 2016;81:289-295.

[141] Thomas S, Bongiovanni C, Nutt SR. In situ estimation of through-thickness resin flow using ultrasound. Composites Science and Technology 2008;68(15):3093-3098.

[142] LeBel F, Fanaei AE, Ruiz E, Trochu F. Experimental characterization by fluorescence of capillary flows in dual-scale engineering fabrics. Text Res J 2013;83(15):1634-1659.

[143] Brandley MW. Void Modeling in Resin Infusion. 2015.

[144] Product Data Sheet: Hexflow RTM6. 2009;2015(1/7).

[145] Ravey C, Lebel F, Ruiz E, Trochu F, Void minimization and optimisation of injection velocity in RTM Processing. In: ICCM 19, International Conference on Composite Materials. , 2013.

[146] Zobell B, George A. In-situ bubble characterization during resin infusion for process simulation of voids.

[147] Zobell B, George A, Fullwood D. In Situ Characterization of Voids During Liquid Composite Molding. 2017.

[148] Kang JH, Kim SM, Woo YS, Lee WI. Analysis of resin flow during nano-imprinting lithographic process. Current Applied Physics 2008;8(6):679-686.

[149] George A, Drechsler K, Void characterization and membrane selection in the vacuum assisted process. In: 15th European Conference on Composite Materials. , 2012.

[150] Dungan FD, Senoguz MT, Sastry AM, Faillaci DA. On the use of Darcy permeability in sheared fabrics. J Reinf Plast Compos 1999;18(5):472-484.

[151] Patiño Arcila I, Power H, Nieto Londoño C, Flórez Escobar W. Boundary Element Method for the dynamic evolution of intra-tow voids in dual-scale fibrous reinforcements using a Stokes-Darcy formulation. Eng Anal Boundary Elem 2018;87:133-152.

[152] Kuentzer N, Simacek P, Advani SG, Walsh S. Permeability characterization of dual scale fibrous porous media. Composites Part A: Applied Science and Manufacturing 2006;37(11):2057-2068.

[153] Zhou F, Alms J, Advani SG. A closed form solution for flow in dual scale fibrous porous media under constant injection pressure conditions. Composites Sci Technol 2008;68(3–4):699-708.

[154] Ravey C, Ruiz E, Trochu F. Determination of the optimal impregnation velocity in resin transfer molding by capillary rise experiments and infrared thermography. Composites Sci Technol 2014;99:96-102.

[155] Xueshu L, Fei C. A review of void formation and its effects on the mechanical performance of carbon fiber reinforced plastic. Engineering Transactions 2016;64(1):33–51.

[156] Liebig WV, Viets C, Schulte K, Fiedler B. Influence of voids on the compressive failure behaviour of fibre-reinforced composites. Composites Sci Technol 2015;117:225-233.

[157] Han G, Guan Z, Li X, Ji R, Du S. The failure mechanism of carbon fiber-reinforced composites under longitudinal compression considering the interface. Science and Engineering of Composite Materials 2017;24(3):429-437.

[158] Nair SN, Dasari A, Yue CY, Narasimalu S. Failure Behavior of Unidirectional Composites under Compression Loading: Effect of Fiber Waviness. Materials 2017;10(8):909.

[159] Meredith J, Bilson E, Powe R, Collings E, Kirwan K. A performance versus cost analysis of prepreg carbon fibre epoxy energy absorption structures. Composite Structures 2015;124:206-213.

[160] Profit P, Blog R. SEER Composites Brings Cost Estimating to CATIA Product Cost Management, Product Lifecycle Management, Software Tools (for PCM, ERP, PLM, etc.), Uncategorized 1 Response».

[161] Pagan JE, Huynh D, Schafer SR, Pinon-Fischer OJ, Mavris DN, Revolutionary Affordable Architecture Generation & Evaluation-Application to a System of Attritable UAVs. In: 2018 AIAA Aerospace Sciences Meeting. , 2018. p. 1743.

[162] Rush C, Dequine D, Continuous fiber composite part cost vs production volume by manufacturing process and material. In: International Cost Estimating and Analysis Association. December 2014, 2014.